



VRIJE  
UNIVERSITEIT  
BRUSSEL

Vrije Universiteit Brussel  
Faculteit Wetenschappen en  
Bio-ingenieurswetenschappen  
Departement Natuurkunde

1

2

3

4

5

6

7

8

9

10

11

12

---

# Search for Dark Matter in the Monojet and Trackless Jets Final States with the CMS Detector at the LHC

---

Isabelle De Bruyn

Promotor

Prof. Dr. Steven Lowette

Proefschrift ingediend met het oog op het behalen van de  
academische graad van Doctor in de Wetenschappen

September 2017



## Acknowledgements



# Table of Contents

1

2	<b>Acknowledgements</b>	i
3	<b>1 Introduction</b>	1
4	<b>2 Dark Matter Scenarios Beyond the Standard Model</b>	3
5	2.1 The Standard Model of Particle Physics . . . . .	3
6	2.1.1 Elementary particles and their interactions . . . . .	3
7	2.1.2 The theoretical framework of the Standard Model . . . . .	4
8	2.1.3 Unanswered questions of the Standard Model . . . . .	6
9	2.2 Dark matter . . . . .	7
10	2.2.1 Observational evidence . . . . .	7
11	2.2.2 Dark matter models . . . . .	10
12	2.2.3 Detection of dark matter . . . . .	12
13	2.2.3.1 Direct detection experiments . . . . .	12
14	2.2.3.2 Indirect detection experiments . . . . .	13
15	2.2.3.3 Collider experiments . . . . .	15
16	2.3 Strongly Interacting Massive Particles . . . . .	15
17	2.3.1 The SIMP simplified model . . . . .	15
18	2.3.2 Experimental constraints . . . . .	17
19	<b>3 The LHC and the CMS Detector</b>	21
20	3.1 The Large Hadron Collider at CERN . . . . .	21
21	3.1.1 The LHC injector chain . . . . .	21
22	3.1.2 The Large Hadron Collider . . . . .	22
23	3.1.3 The experiments at the LHC . . . . .	23
24	3.2 The CMS detector . . . . .	24
25	3.2.1 The tracker . . . . .	25
26	3.2.1.1 The pixel tracker . . . . .	25
27	3.2.1.2 The strip tracker . . . . .	26
28	3.2.2 The electromagnetic calorimeter . . . . .	26
29	3.2.3 The hadronic calorimeter . . . . .	28
30	3.2.4 The muon system . . . . .	28
31	3.2.5 Trigger and data acquisition . . . . .	30
32	3.2.6 CMS performance in Run 2 . . . . .	31
33	3.2.6.1 Pre-amplifier saturation in the APV25 chip . . . . .	31
34	<b>4 Event Simulation and Reconstruction</b>	35
35	4.1 Event generation . . . . .	35
36	4.2 Detector simulation . . . . .	36
37	4.3 Event reconstruction . . . . .	37
38	4.3.1 Track and vertex reconstruction . . . . .	37
39	4.3.2 Electron and isolated photon reconstruction . . . . .	38
40	4.3.3 Electron and photon identification . . . . .	39
41	4.3.4 Muon reconstruction . . . . .	39
42	4.3.5 Particle flow . . . . .	40
43	4.3.6 Jet reconstruction . . . . .	40
44	4.3.7 Identification of b-jets . . . . .	42
45	4.3.8 Reconstruction of tau leptons . . . . .	42

1	4.3.9	Missing transverse momentum reconstruction . . . . .	42
2	4.4	Simulation of the SIMP signal . . . . .	43
3	<b>5</b>	<b>The Monojet Analysis</b>	<b>47</b>
4	5.1	Event selection . . . . .	47
5	5.2	Background estimation . . . . .	48
6	5.2.1	The $Z$ and $W$ background estimation . . . . .	48
7	5.2.2	The QCD background estimation . . . . .	52
8	5.3	Systematic uncertainties . . . . .	52
9	5.4	Results . . . . .	52
10	5.5	Improvement going from the 2015 to 2016 analysis . . . . .	52
11	5.6	Interpretation . . . . .	53
12	<b>6</b>	<b>Search for SIMPs using Trackless Jets</b>	<b>55</b>
13	6.1	Physics object reconstruction . . . . .	55
14	6.1.1	Jets . . . . .	55
15	6.1.2	Photons . . . . .	56
16	6.1.3	Primary vertex . . . . .	56
17	6.2	Trigger selection . . . . .	57
18	6.3	Event selection . . . . .	59
19	6.4	Background estimation . . . . .	60
20	6.4.1	Photon + jets . . . . .	61
21	6.4.2	QCD multijets . . . . .	61
22	6.5	Systematic uncertainties . . . . .	65
23	6.6	Results . . . . .	66
24	6.7	SIMP model interpretation . . . . .	67
25	<b>7</b>	<b>Conclusion &amp; Outlook</b>	<b>69</b>

# 1

## Introduction

1

2



# 2

1

2

3

## Dark Matter Scenarios Beyond the Standard Model

4 In modern particle physics, the fundamental structure of matter at subatomic scales is described by the  
5 Standard Model [1, 2], which has already predicted many experimental results and is today considered  
6 among the most thoroughly tested scientific theories. The Higgs boson, the last missing piece which  
7 was predicted more than 50 years ago, was recently discovered at the Large Hadron Collider (LHC) in  
8 2012 [3, 4], thus completing this elegant theory. Although it has survived many precision tests so far,  
9 the Standard Model only describes 5% of the matter and energy in the known universe and is unable to  
10 explain many unresolved questions and observations, such as the baryon asymmetry, dark matter and dark  
11 energy, the neutrino masses, the incorporation of gravity, and the hierarchy problem.

12 In this chapter, a brief description of the Standard Model is first given in Section 2.1, including its  
13 shortcomings. In Section 2.2, one of the missing pieces in the Standard Model, dark matter, is discussed.  
14 The observational evidence for dark matter, as well as possible models and detection mechanisms are  
15 detailed. Finally, in Section 2.3 one of the dark matter models considered in this thesis is described in  
16 detail.

### 2.1 The Standard Model of Particle Physics

18 The Standard Model of elementary particle physics has been developed during the second half of the  
19 20th century, and reached its current formulation in the 1970's with the combination of the electromagnetic  
20 and weak interactions into the electroweak interaction [5–7], incorporating the Brout-Englert-Higgs  
21 (BEH) mechanism [8–10], and the addition of asymptotic freedom [11, 12] into the theory of the strong  
22 interaction. It is a quantum field theory which describes the fundamental particles and their interactions,  
23 incorporating three of the four fundamental forces. While this consistent framework describes the elec-  
24 tronagnetic force and the weak and strong nuclear interactions, the fourth interaction, gravity, has not yet  
25 been included successfully.

#### 2.1.1 Elementary particles and their interactions

27 All ordinary matter we see around us is built up from atoms, which consist of negatively charged electrons  
28 circulating around the positively charged atomic nucleus, formed by protons and neutrons, which in turn  
29 consist of up and down quarks. The electrons and up and down quarks are fundamental particles called  
30 fermions. Although all ordinary matter can be built from this so-called first generation of fermions,  
31 there are twelve fermions with different flavours in total, six quarks and six leptons, grouped in three

generations with increasing mass, as shown in Figure 2.1. The electrically neutral neutrinos interact only via the weak nuclear interaction, which complicates their observation, but they can be detected in dedicated experiments.

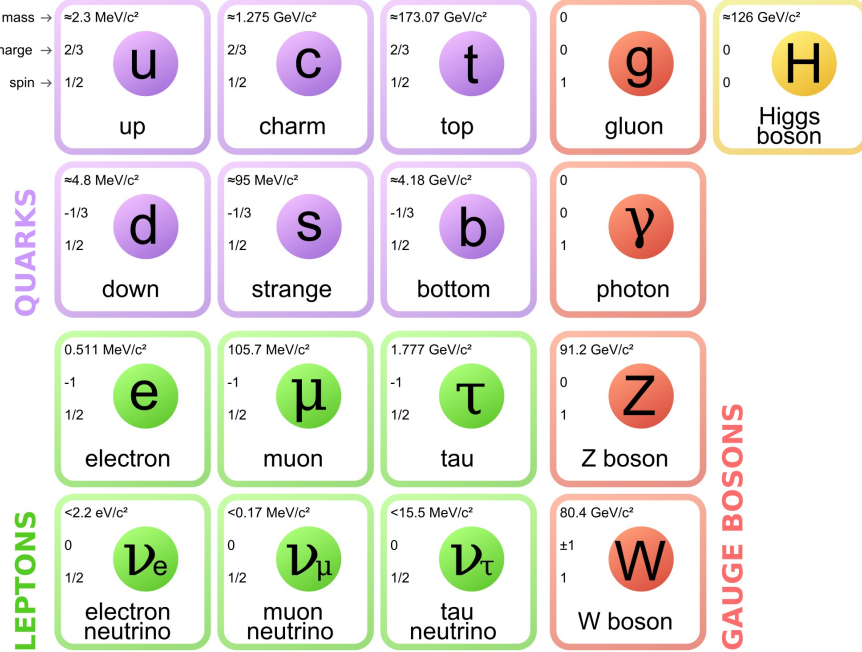


Figure 2.1: The particle content of the Standard Model, showing the fermions divided into 3 generations (columns) on the left and the bosons on the right. The electrical charges are expressed as multiples of the absolute value of the electron charge. Figure taken from [13].

A common characteristic of the fermions is their half-integer spin, in contrast to the integer spin of the force mediators, called bosons. Within the Standard Model, the mediation of the different fundamental interactions is represented by the exchange of these spin-1 gauge bosons, which are summarized in Figure 2.1. The massless photon mediates the most familiar force, the electromagnetic interaction, which is responsible for light, electromagnetic fields, and chemical reactions. The weak nuclear interaction is among other things used to describe the radioactive  $\beta$  decay, and is propagated by the neutral  $Z$  boson and two charged massive  $W$  bosons. Lastly, the strong nuclear interaction is carried by massless gluons, keeping the protons and neutrons in the atomic nuclei and holding the quark constituents together. A resulting property of the quarks is that they hadronise, i.e. they cannot exist isolated, but form bound states via the strong interaction. These bound states are referred to as hadrons, and can be made up from three quarks or a quark and an antiquark, respectively called baryons and mesons.

Finally, it is also important to note that for every fermion ( $f$ ) there exists an antifermion ( $\bar{f}$ ), which differs only in electric charge and handedness of spin. When matter and antimatter come into contact they annihilate, generating energy which can be transformed into other particles.

### 2.1.2 The theoretical framework of the Standard Model

The Standard Model goes further than merely giving an exhaustive list of elementary particles, it has a supporting theoretical framework formulated as a relativistic quantum field theory. In a quantum field theory, every particle is represented by discrete excitations of a field  $\psi(x)$ , where  $x$  is the space-time coordinate. The interactions and kinematics of this particle are fully determined by the action  $S$ , which is defined as the integral of the Lagrangian  $\mathcal{L}(\psi(x), \partial^\mu\psi(x))$  over the space-time coordinates:

$$S = \int \mathcal{L}(\psi(x), \partial^\mu\psi(x)) d^4x. \quad (2.1)$$

The Lagrangian is a function of the field  $\psi(x)$  and its first derivative  $\partial^\mu\psi(x)$ , where  $\mu$  represents the index of the space-time coordinate. The physical behaviour of the particles is obtained by following the principle of least action  $\delta S = 0$ , minimizing the action.

In this framework based on the gauge invariance of the Lagrangian under the fundamental symmetries, the interactions between the fermions and bosons follow automatically. This can be illustrated with the following example for invariance under a general local gauge transformation.

As mentioned before, a fermion has a half integer spin and can thus be represented as a complex relativistic spin-1/2 field, called a Dirac spinor:

$$\mathcal{L}_{Dirac} = i\bar{\psi}\gamma^\mu\partial_\mu\psi - m\bar{\psi}\psi, \quad (2.2)$$

where  $\gamma^\mu$  are the Dirac matrices, and the adjoint field  $\bar{\psi} = \psi^\dagger\gamma^0$  is the field associated to the antifermion. The imposed local gauge invariance then requires the fermion fields, and the overall Lagrangian, to be invariant under so-called local phase transformations

$$\psi \rightarrow \psi' = U(x)\psi = e^{i\vec{\alpha}(x) \cdot \frac{\vec{\tau}}{2}}\psi \quad (2.3)$$

where  $\vec{\alpha}(x)$  are the space-time dependent rotation parameters in the symmetry group represented by the Lie group generators  $\vec{\tau}$ . Since the derivative  $\partial_\mu$  in (2.2) spoils the invariance of the Lagrangian under a local phase transformation, it is replaced with a covariant derivative

$$D_\mu = \partial_\mu - ig\frac{\vec{\tau}}{2}\vec{A}_\mu, \quad (2.4)$$

restoring the invariance. This however introduces new vector gauge fields  $A_\mu$ , which interact with the fermion fields with a coupling strength  $g$ . As a result, the Dirac Lagrangian contains an additional term, which describes the interaction between the fermion fields mediated by the gauge fields  $A_\mu$ , and (2.2) becomes

$$\mathcal{L}_{Dirac} = i\bar{\psi}\gamma^\mu\partial_\mu\psi - m\bar{\psi}\psi + g\bar{\psi}\gamma^\mu\psi\vec{A}_\mu \cdot \frac{\vec{\tau}}{2} \quad (2.5)$$

The matrix  $U(x)$  which was introduced above, was defined as a general rotation matrix of the symmetry group  $SU(N)$ . In order to obtain the three fundamental interactions of the Standard Model, the described procedure can be simplified using the corresponding symmetry groups as mentioned below.

## Electroweak theory

The electroweak interaction describes the electromagnetic and weak interactions, which appear very different at low energies but can be merged into a single electroweak force above the electroweak energy scale. This theory is described by requiring gauge invariance under the  $SU(2)_L \otimes U(1)_Y$  symmetry group. This leads to 3 gauge fields  $W_\mu^\alpha$  introduced by the  $SU(2)_L$  group, and one gauge field  $B_\mu$  from the  $U(1)_Y$  group. Two coupling constants are introduced,  $g_1$  and  $g_2$ , for  $U(1)_Y$  and  $SU(2)_L$ , respectively. The corresponding observable gauge bosons are the photon, the  $Z^0$ , and the  $W^\pm$  bosons.

## Quantum Chromodynamics (QCD)

The strong interaction is described by the theory of Quantum Chromodynamics and is represented by the symmetry group  $SU(3)$ . It describes the interaction between particles that carry a colour charge, which can be red, green, blue, or one of the three corresponding anticolours. There are eight gauge boson fields associated to this group, which are massless and known as gluons. An important aspect which is unique for this interaction is asymptotic freedom, which states that the strong coupling constant, denoted by  $\alpha_s$ , goes to zero at high energies. Consequently, the strong force becomes stronger as the distance between the strongly interacting quarks and gluons increases. As a result, the quarks and gluons cannot exist independently and are not observed individually, but are instead confined in colour-neutral hadrons. This effect is called confinement.

At this point the resulting Lagrangian including the three fundamental forces does not contain any mass terms, and so it cannot explain the observed particle masses. Additional mass terms cannot simply

be added explicitly because they would break gauge invariance. Instead, a solution to this problem is found by introducing a complex scalar doublet  $\phi$  with a non-zero vacuum expectation value (vev)  $v$ . This breaks the electroweak symmetry and is known as the Brout-Englert-Higgs (BEH) mechanism, postulated in 1964 [8–10]. The Lagrangian of the Higgs field is

$$\begin{aligned}\mathcal{L}_H &= (D^\mu\phi)^\dagger(D_\mu\phi) - V(\phi) \\ &= (D^\mu\phi)^\dagger(D_\mu\phi) - \frac{1}{2}\mu^2\phi^\dagger\phi + \frac{1}{4}\lambda^2(\phi^\dagger\phi)^2,\end{aligned}\quad (2.6)$$

where  $\mu$  is a real constant representing a mass parameter and  $\lambda$  is a dimensionless parameter standing for the self-interaction strength. The potential  $V$  of the scalar doublet has an infinite set of minima or ground states, and by choosing a ground state and expanding the field around it, the electroweak symmetry is broken. As a result, three of the four original fields of the scalar doublet are absorbed by the massless vector fields of the weak interaction, giving mass to the  $W$  and  $Z$  bosons:

$$M_W = \frac{1}{2}vg_2 \quad M_Z = \frac{1}{2}v\sqrt{g_1^2 + g_2^2}. \quad (2.7)$$

From the remaining field, the  $H$  boson arises, acquiring a mass  $m_H = \sqrt{2\lambda v}$ .

The introduction of mass terms for the fermions also follows from the BEH mechanism, which allows to insert the following gauge-invariant term in the Lagrangian:

$$\mathcal{L}_{Yukawa} = -Y_{ij}\bar{\psi}_{L,i}\phi\psi_{R,j} + h.c. \quad (2.8)$$

with the  $Y_{ij}$  Yukawa matrices. The  $L$  and  $R$  here denote left-handed and right-handed fermions. This handedness or chirality is defined as  $\psi_L = \frac{1}{2}(1 - \gamma_5)\psi$  for left-handed and  $\psi_R = \frac{1}{2}(1 + \gamma_5)\psi$  for right-handed fermions. The fermion masses then arise from the Yukawa interactions describing the couplings of the fermions with the Higgs field. For massive particles, a reference frame which overtakes the spinning particle can always be found, in which case the particle will seem to move backwards, flipping its helicity<sup>1</sup>. This is however not the case for massless particles, which travel at the speed of light. As only left-handed neutrinos and right-handed antineutrinos have been observed so far, the neutrinos are massless in the Standard Model.

### 2.1.3 Unanswered questions of the Standard Model

Although the Standard Model is an extremely successful theory, there are still many questions that remain unanswered, indicating that the Standard Model cannot be a complete theory of nature. A brief description of some of the main unsolved problems follows here.

#### Grand Unified Theory

As the weak and electromagnetic interactions were successfully unified into the electroweak one, the idea of representing the three forces of the Standard Model by a single one is envisaged and studied. While this Grand Unified Theory (GUT) could be a first step towards the incorporation of gravity in the Standard Model, it cannot be achieved with the current Standard Model and requires new physics at a very high energy scale.

#### Baryon asymmetry

This problem refers to the imbalance of matter and antimatter in the universe. While the Big Bang should have produced an equal amount of baryonic and antibaryonic matter, this is not measured in our observable universe. It is assumed that most of the primordial matter and antimatter annihilated, but an imbalance allowed a fraction of the matter to survive. Within the Standard Model, some asymmetry in the production of matter and antimatter could be explained by the CP-violation<sup>2</sup> of the weak interaction. However, the amount of CP-violation needed to explain the baryon asymmetry is ten times higher than is observed from Standard Model measurements.

<sup>1</sup>The helicity is defined as the sign of the projection of the spin vector onto the momentum vector of a particle, left is negative and right is positive.

<sup>2</sup>According to Charge Parity (CP) symmetry, the laws of physics should remain identical when converting a particle into its antiparticle and mirroring the space coordinates. However, measurements of e.g. kaon-antikaon mixing show that this symmetry is violated.

1      **Hierarchy problem**

2      The most important hierarchy problem concerns the question why the weak force is so much  
 3      stronger than gravity. The measured vector boson masses suggest that the electroweak symme-  
 4      try breaking should occur at an energy scale of  $\mu^2 \sim (100 \text{ GeV})^2$ , while the energy regime  
 5      where gravity becomes comparable to the other forces, called the Planck scale, is of the order  
 6      of  $\Lambda_{\text{Planck}} \sim 10^{19} \text{ GeV}$ . This question is related to the mystery as to why the Higgs boson mass is  
 7      so much smaller than the Planck scale. The real physical Higgs boson mass is composed of its bare  
 8      mass and quantum loop corrections. These corrections depend strongly on a cut-off scale, which  
 9      would be the Planck scale if no additional physics on top of the Standard Model is present up to  
 10     this scale. In order for the theoretical prediction to match the experimentally determined mass of  
 11     125 GeV, the bare mass would need to be tuned to cancel the huge quadratic radiative corrections.  
 12     This would require a significant fine-tuning of more than 30 orders of magnitude, which is not  
 13     desirable for any theory.

14     **Neutrino masses**

15     The Standard Model predicts that the neutrinos are massless weakly interacting particles, but ob-  
 16     servations by the Sudbury Neutrino Observatory [14] and Super-Kamiokande [15] collaborations  
 17     showed the first clear evidence that the neutrinos oscillate from one flavour into another. This can  
 18     only be explained if the neutrinos differ in mass, implying that they are not massless. As men-  
 19     tioned above, the Standard Model does not provide masses for the neutrinos and it should therefore  
 20     be extended to explain this observation.

21     **Dark matter and energy**

22     This mystery arises from cosmological observations, which indicate that the known matter de-  
 23     scribed by the Standard Model makes up only 5% of the matter and energy in the universe. The  
 24     remaining matter, called dark matter, contributes another 27%, and will be discussed in more detail  
 25     in Section 2.2. In the Standard Model, neutrinos contribute to the dark matter, but their relic density  
 26     is by far not enough to account for all the dark matter. The last 68% has been labelled dark energy  
 27     and is believed to be responsible for the acceleration of the observed expansion of the universe, but  
 28     remains even more enigmatic as no explanation can be provided by the Standard Model.

29     **2.2 Dark matter**

30     One of the current open questions in particle physics that is not answered by the Standard Model is the ex-  
 31     istence of dark matter. Many astrophysical observations from gravitational effects (see for instance [16])  
 32     show there must be some additional matter in the universe, the so-called dark matter, next to the known  
 33     matter. Despite this, its precise nature remains as of yet unknown. Countless theoretical models are being  
 34     constructed in order to explain its origin, and on the experimental side dark matter is being looked for in  
 35     many different ways, but no observation has been made so far.

36     **2.2.1 Observational evidence**

37     The first hints of dark matter were observed by F. Zwicky [17] in 1933 by studying the velocity dispersion  
 38     of galaxies in the Coma cluster. The effect is not only observed for entire galaxies, but also for various  
 39     luminous objects, such as stars or gas clouds, inside a galaxy. The rotation curves of galaxies have been  
 40     well studied, and show clear evidence for the existence of dark matter. An example of a rotation curve is  
 41     shown in Figure 2.2, exhibiting a flat behaviour of the rotational velocity at large distances, going even  
 42     far beyond the edge of the visible disk. However, in Newtonian dynamics the circular velocity is expected  
 43     to be

$$v(r) = \sqrt{\frac{GM(r)}{r}}, \quad (2.9)$$

44     where  $M(r) = 4\pi \int \rho(r)r^2 dr$  with  $\rho(r)$  the mass density profile. Assuming  $M(r)$  to be constant, the  
 45     circular velocity is expected to fall like  $1/\sqrt{r}$  beyond the disk. Since the measurements show an approx-  
 46     imately constant velocity but a dropping visible mass density, this implies the existence of a halo with

<sup>1</sup>  $M(r) \propto r$  and  $\rho(r) \propto 1/r^2$ . A universal density profile seems to be suggested by the rotation curves of  
<sup>2</sup> both low and high surface luminosity galaxies, consisting of an exponential thin stellar disk and a spheri-  
<sup>3</sup> cal dark matter halo with a flat core of radius  $r_0$  and density  $\rho_0 = 4.5 \times 10^{-2} (r_0/\text{kpc})^{-2/3} M_\odot \text{pc}^{-3}$  [18]<sup>3</sup>.

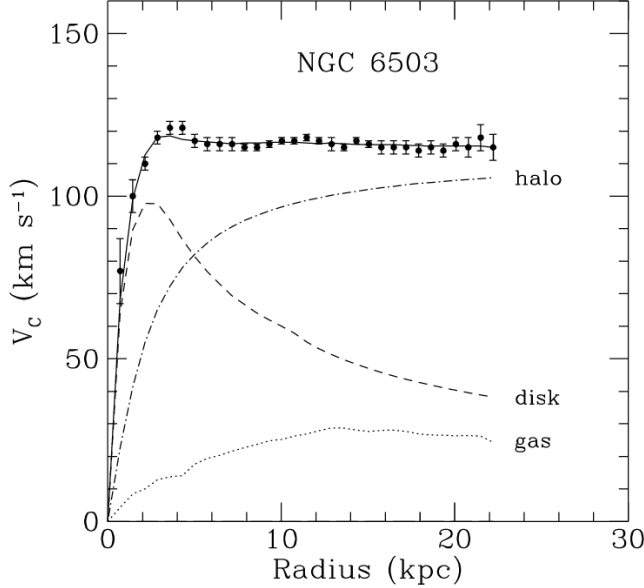


Figure 2.2: Rotation curve of NGC 6503. The dotted, dashed, and dash-dotted lines show the contributions of gas, disk, and dark matter, respectively. Figure taken from [19].

<sup>4</sup> Another evidence for dark matter comes from the effect of gravitational lensing, allowing to determine  
<sup>5</sup> the mass of an object regardless of the light it emits. When a distant star or quasar is aligned with a  
<sup>6</sup> massive compact object, the bending of its light due to the gravitational field of the massive object can  
<sup>7</sup> lead to multiple distorted, magnified, and brightened images, as illustrated in Figure 2.3. The distortion  
<sup>8</sup> of the image can then be used to determine the potential well and thus the mass of the heavy object.  
<sup>9</sup> Yet another way to determine the mass of a cluster of galaxies, next to gravitational lensing and the  
<sup>10</sup> distribution of radial velocities, is by studying the profile of X-ray emission, tracing the distribution of  
<sup>11</sup> the hot emitting gas in clusters. In general, these three methods are in reasonable agreement with each  
<sup>12</sup> other.

<sup>13</sup> Additionally, at a cosmological level, the analysis of the Cosmic Microwave Background (CMB)  
<sup>14</sup> allows to determine the total amount of dark matter in the universe. The existence of this isotropic  
<sup>15</sup> background radiation was already predicted in 1948, and unintentionally discovered by A. Penzias and  
<sup>16</sup> R. Wilson in 1965 [21]. This relic radiation comes from the propagation of photons in the early universe,  
<sup>17</sup> once they decoupled from matter. Before this, the photons were energetic enough to ionise hydrogen,  
<sup>18</sup> creating a plasma of electrons and protons which were unable to combine into hydrogen. As the universe  
<sup>19</sup> expanded and cooled down, the photons also cooled down enough to let the hydrogen atoms recombine,  
<sup>20</sup> and the universe became transparent. The photons can then travel freely without scattering off the protons  
<sup>21</sup> and electrons of the plasma, still carrying information from this surface of last scattering. The CMB is  
<sup>22</sup> now known to be isotropic at the level of  $10^{-5}$  and to follow the spectrum of a black body corresponding  
<sup>23</sup> to a temperature of 2.726 K. However, small anisotropies in the CMB have first been observed by the  
<sup>24</sup> COBE satellite [22] and more recently by WMAP [23] and Planck [24], as can be seen in Figure 2.4.  
<sup>25</sup> These anisotropies correspond to small thermal variations, and are usually expanded as

$$\frac{\delta T}{T}(\theta, \phi) = \sum_{l=2}^{+\infty} \sum_{m=-l}^{+l} a_{lm} Y_{lm}(\theta, \phi), \quad (2.10)$$

---

<sup>3</sup> $M_\odot$  denotes a solar mass,  $2 \times 10^{30}$  kg.

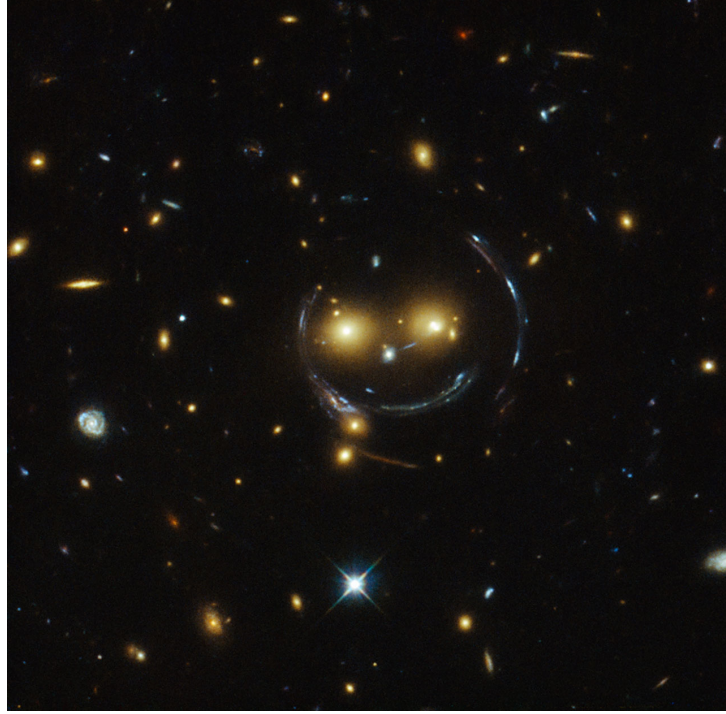


*Figure 2.3: An example of gravitational lensing showing the “Cheshire Cat” image of galaxy cluster SDSS J1038+4849, taken by the Hubble Space Telescope. Figure taken from [20].*

where  $Y_{lm}(\theta, \phi)$  are spherical harmonics. The variance of  $a_{lm}$  is given by

$$C_l = \langle |a_{lm}|^2 \rangle = \frac{1}{2l+1} \sum_{m=-l}^{+l} |a_{lm}|. \quad (2.11)$$

As the temperature fluctuations appear to be Gaussian, all the information contained in the CMB anisotropy maps can be condensed into the power spectrum given by the behaviour of  $C_l$  as a function of  $l$ . This is generally represented using  $D_l = l(l + 1)C_l/2\pi$ , as illustrated in Figure 2.5.

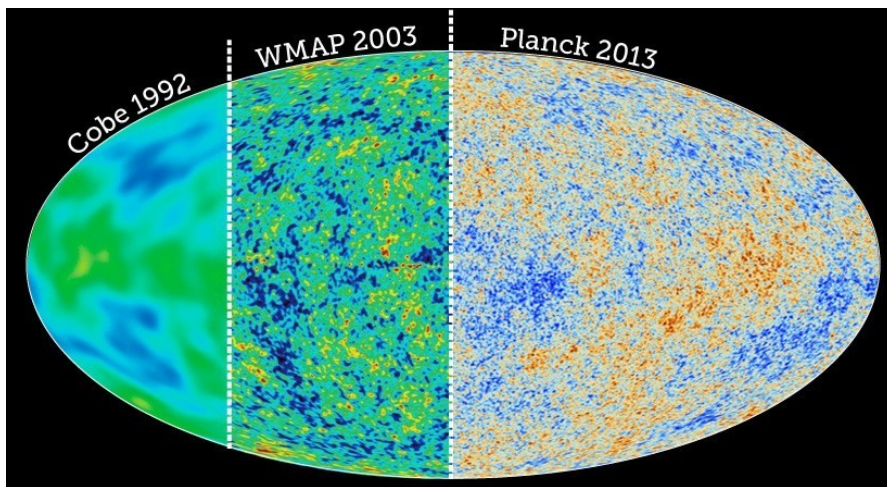


*Figure 2.4: The CMB temperature fluctuations obtained from the COBE, WMAP, and Planck data. Figure taken from [25].*

The CMB anisotropies are caused by acoustic oscillations arising from the conflict between the gravitational pull from baryons and dark matter and the repulsive force due to the radiation pressure from the photons. One popular model to describe and interpret these observations is the  $\Lambda$ CDM model. CDM

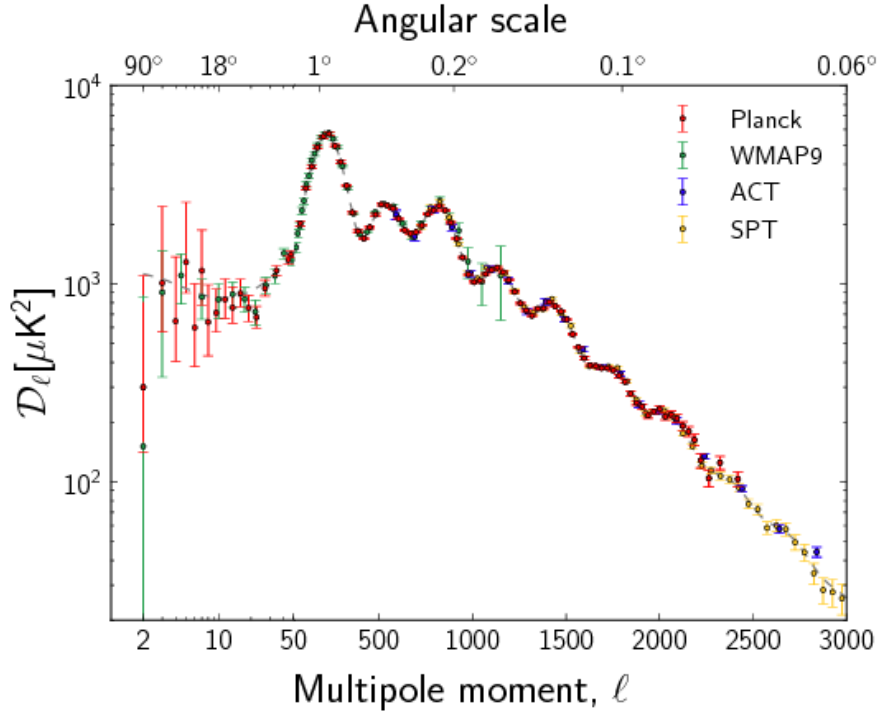


Figure 2.5: The observed power spectrum of the CMB anisotropies. The horizontal axis is logarithmic up to  $\ell = 50$  and linear beyond. Figure taken from [26].

1 stands for cold dark matter, indicating that in this model the dark matter particles are moving slowly compared  
2 to the speed of light, while the  $\Lambda$  represents the cosmological constant, which is associated with the  
3 vacuum energy or dark energy that is used to explain the accelerating expansion of space. The  $\Lambda$ CDM  
4 model is compatible with a number of observations beyond the CMB fluctuations, such as the large scale  
5 structure in the distribution of galaxies, the relative abundance of light nuclei, and the accelerating expansion  
6 of the universe which is observed from the red shift of well-known spectral absorption or emission  
7 lines in the light of distant galaxies. Using this model to fit the power spectrum, the multiple peaks in the  
8 spectrum can be interpreted. The angular scale of the first peak can be used to determine the curvature of  
9 the universe. The second peak determines the reduced baryon density and the third peak can be used to  
10 retrieve information about the dark matter density. From the analysis of the Planck data the abundance of  
11 baryons and matter in the universe is determined to be

$$\Omega_b h^2 = 0.02205 \pm 0.00028 \quad \Omega_M h^2 = 0.1423 \pm 0.0029 \quad (2.12)$$

12 This result shows that only about 15% of the matter in the universe is made up from the ordinary known  
13 matter, and the remaining 85% is called dark matter.

14 More evidence for dark matter was found from a great variety of data, both on subgalactic and inter-  
15 galactic scales. Without discussing them here in detail, a few examples are the velocity dispersions of spiral  
16 galaxy satellites, suggesting the existence of dark halos around spiral galaxies extending well beyond  
17 the visible disk [27], the velocity dispersion of dwarf spheroidal galaxies, implying larger mass-to-light  
18 ratios than those observed in our local neighbourhood [28], and the so-called Oort discrepancy in the disk  
19 of the Milky Way, inferring the existence of dark matter from the inconsistency between the amount of  
20 stars in the solar neighbourhood and the gravitational potential indicated by their distribution [29].

### 21 2.2.2 Dark matter models

22 Since very little is known so far concerning the nature of dark matter, a multitude of dark matter candidates  
23 are discussed in the literature. Without attempting to be complete, a list is given and a few of the more  
24 popular candidates are briefly covered here.

1           **Standard Model neutrinos**

2           As mentioned before, the Standard Model could explain the existence of dark matter with the  
 3           already observed neutrinos. However, it can be shown [30] that their total relic density is predicted  
 4           to be

$$\Omega_\nu h^2 = \sum_{i=1}^3 \frac{m_i}{93 \text{ eV}}, \quad (2.13)$$

5           taking the sum over the 3 neutrino flavours. Currently, the most stringent upper bound on neutrino  
 6           masses is

$$m_\nu < 2.05 \text{ eV} \quad \text{at 95% CL} \quad (2.14)$$

7           obtained in tritium  $\beta$ -decay experiments at Troitsk [31, 32] and Mainz [33]. Since the mass dif-  
 8           ference between the 3 neutrinos must be very small to explain solar and atmospheric neutrino  
 9           anomalies [34], this mass limit applies to the three mass eigenvalues, implying an upper bound on  
 10          the total neutrino relic density of

$$\Omega_\nu h^2 \lesssim 0.07. \quad (2.15)$$

11          This shows that Standard Model neutrinos are not abundant enough to be the dominant component  
 12          of dark matter.

13           **Sterile neutrinos**

14          Proposed in 1993 by Dodelson and Widrow [35], these hypothetical particles are similar to the  
 15          Standard Model neutrinos, but without Standard Model weak interactions, except for mixing. The  
 16          analysis of their cosmological abundance and the study of their decay products places stringent con-  
 17          straints on the sterile neutrinos. Light neutrinos with masses below a few keV would for example  
 18          be ruled out [36].

19           **Axions**

20          These particles were originally introduced to solve the problem of the apparent absence of CP-  
 21          violation by the strong interaction, and have often been discussed as dark matter candidates. They  
 22          are expected to interact extremely weakly with Standard Model particles. Furthermore, observa-  
 23          tions from laboratory searches, stellar cooling, and the dynamics of supernova 1987A constrain the  
 24          axion mass to be very small, of the order of or below 0.01 eV [37].

25           **SUSY candidates**

26          Several particles in supersymmetry (SUSY) models can serve as dark matter candidate, such as  
 27          gravitinos and neutralinos. Gravitinos are the superpartners of the graviton. In some SUSY models,  
 28          they can be the lightest supersymmetry particle and can be stable. While they are very strongly  
 29          motivated theoretically, they are very difficult to observe, as they only interact gravitationally. The  
 30          neutralinos are the superpartners of the photon,  $Z$  boson, and neutral Higgs bosons. The lightest  
 31          of the four is stable and is an excellent dark matter candidate. These dark matter candidates are  
 32          often called weakly interacting massive particles (WIMPs), since they are massive and interact  
 33          through the weak interaction. As many SUSY models predict a new particle with the correct  
 34          properties and self-annihilation cross section to obtain the correct abundance of dark matter today,  
 35          a stable supersymmetric partner has long been a very plausible dark matter candidate and a lot of  
 36          experimental effort has been made to detect it.

37           **WIMPs**

38          A prevalent assumption is that dark matter particles are a relic from the early universe, when all  
 39          particles were in thermal equilibrium. At those high energies the dark matter particles and antiparti-  
 40          cles could be formed by sufficiently energetic lighter particles, and they would annihilate back into  
 41          these lighter particles as well. However, as the universe expanded and cooled down, the thermal en-  
 42          ergy of the lighter particles became insufficient to form dark matter particle-antiparticle pairs. The  
 43          annihilation of the dark matter particles and antiparticles continued however, until the dark matter  
 44          density decreased considerably and the interaction between the dark matter particles stopped. The

number of dark matter particles would remain constant from that moment on. In comparison, particles with a large interaction cross section would continue to annihilate for a longer period of time and would be less abundant.

The interaction cross section of the annihilating dark matter particles can be inferred from the current estimates of the dark matter abundance in the universe, and can in this case not be larger than the cross section of the weak interaction. According to this model, WIMPs would be the perfect candidates for dark matter. In general, they are hypothetical new elementary particles that interact gravitationally and through any other force which is as weak or weaker than the Standard Model weak interaction, and they could have been produced thermally as described in this model. Since WIMPs have a relatively large mass, they would also constitute cold dark matter, which would fit the observed large scale structure of the universe. The coincidence of WIMPs fitting so well into this model and corresponding to the current observations is known as the “WIMP miracle”.

Many more dark matter candidates are discussed in literature, such as but not limited to heavy fourth generation neutrinos [38], Kaluza-Klein states in ADD [39] or RS [40] extra dimensions models, superheavy dark matter or Wimpzillas [41], self-interacting dark matter [42], charged massive particles (CHAMPs) [43], and Q-balls [44]. More detailed reviews are given in [30, 45, 46].

Add paragraph on simplified models and mention monojet models.

### 2.2.3 Detection of dark matter

The detection of dark matter can be categorised in three groups, based on the diagram shown in Figure 2.6. In the case of direct detection experiments, the studied process is the scattering of dark matter off ordinary matter. Experiments searching for dark matter with the indirect approach look for particles or radiation produced in the annihilation of dark matter particles. Finally, at collider experiments, attempts are made to produce and detect dark matter particles by colliding Standard Model particles at high energies.

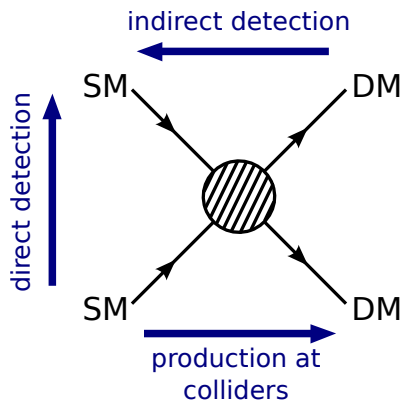


Figure 2.6: Diagram illustrating the three used methods to detect dark matter.

#### 2.2.3.1 Direct detection experiments

This category of experiments is based on the fact that if our galaxy is filled with a static halo of dark matter particles, then many of them should pass through the Earth as it rotates around Galactic Center, and they could be detected by looking for the interaction of such particles with matter. This is for example done by recording the recoil energy of nuclei when WIMPs scatter off them. In order to determine the expected rate of events per unit detector material mass, the WIMP-nucleon scattering cross section and the density and velocity distribution of the WIMPs in the solar neighbourhood are needed.

There are several types of scattering processes which can be classified by two relevant characteristics: elastic or inelastic scattering and spin-dependent or spin-independent scattering. In the case of elastic scattering, the WIMP simply scatters off a nucleus as a whole, causing it to recoil. The recoil energy

1 spectrum can then be measured by detecting the emitted scintillation light with very sensitive detectors  
 2 or by measuring very small temperature changes due to crystal vibrations. Taking a Maxwell-Boltzmann  
 3 velocity distribution with as characteristic velocity our rotation velocity of about 270 km/s, the recoil  
 4 spectrum is exponential with typical energies of  $\langle E \rangle \sim 50$  keV. This range of energies is easily detectable  
 5 by current experiments, which can detect recoils as low as 1-10 keV. Instead, when the WIMP scatters  
 6 inelastically, it interacts with the orbital electrons of the target, exciting the electrons or ionising the  
 7 target. Differently, the WIMP could also excite the target nuclei, which would then emit a photon about a  
 8 nanosecond after the observed recoil. This signature has, however, to compete with the background from  
 9 natural radioactivity.

10 The spin dependence or independence of the scattering depends on the coupling of the WIMPs to  
 11 the Standard Model particles. Spin-dependent interactions result from couplings to the spin content of a  
 12 nucleon, yielding cross sections that are proportional to  $J(J+1)$  instead of the number of nucleons. For  
 13 spin-independent interactions, the cross section instead increases considerably with the mass of the target  
 14 nuclei. The spin-independent scattering therefore dominates over the spin-dependent one in experiments  
 15 which use heavy atoms.

16 Numerous direct detection experiments are currently operational or in development. They use one or  
 17 more techniques to measure the nuclear recoil, by detecting the scintillation light, the change in tempera-  
 18 ture, or the ionisation. Some experiments also try to separate the WIMP signatures from the background  
 19 by looking for an annual modulation in the rate, which arises due to the Earth's movement around the  
 20 Sun. This effect causes the Earth to have a relative velocity with respect to the galaxy's reference frame,  
 21 given by

$$v_E = 220 \text{ km/s} (1.05 + 0.07 \cos(2\pi(t - t_m))), \quad (2.16)$$

22 where the time is in units of years and  $t_m$  is approximately the beginning of June. As a result, a small  
 23 variation of about 7% in the WIMP flux can be measured in the direct detection rate.

24 Currently, there is some tension between the results obtained by the different experiments, as some  
 25 observations can be interpreted as dark matter signals, while other experiments are ruling out those mod-  
 26 els. The DAMA experiment for example observes an annual modulation in the event rate, pointing to the  
 27 existence of WIMPs scattering elastically off the sodium and iodine nuclei in the detector [47]. Other  
 28 experiments, such as SuperCDMS [48], EDELWEISS-III [49], CRESST-II [50], XENON100 [51], have  
 29 seen no evidence for dark matter so far and placed limits on many dark matter models, creating a tension  
 30 with the observed signal at DAMA. For WIMP masses above a few GeV, the strongest limit of direct  
 31 detection experiments for spin-independent interactions is currently given by LUX [52]. For a spin-  
 32 dependent WIMP-proton cross section, the most stringent limit is set by the PICO experiment [53], while  
 33 the PandaX experiment places the strongest limit on the WIMP-neutron cross section [54]. An overview  
 34 of the existing limits and signal observations is given in Figure 2.7, showing the mentioned experiments,  
 35 and a more complete review of the existing direct detection results is given in [55].

### 36 2.2.3.2 Indirect detection experiments

37 The indirect detection of dark matter is performed by looking for radiation produced in dark matter  
 38 annihilations. A reasonable place to look at would then be in regions with large dark matter densities and  
 39 thus larger annihilation rates, which will result in a higher flux of the studied radiation. Some examples  
 40 are dense regions of the galactic halo such as the galactic centre, or objects like the Sun or the Earth,  
 41 which could also capture dark matter particles through scattering with nucleons in their core. In the latter  
 42 case, only neutrinos would be able to escape those dense objects. Other annihilation products include  
 43 gamma rays, positrons, and antiprotons.

44 In order to observe gamma rays directly, the detectors must be placed in space, as photons of the  
 45 relevant energy range (GeV to TeV) interact with matter via  $e^+e^-$  pair production and cannot traverse  
 46 more than a surface density of about  $38 \text{ g cm}^{-2}$ . The gamma rays will not reach the ground-based  
 47 telescopes as the Earth's atmosphere is  $1030 \text{ g cm}^{-2}$  thick. Nevertheless, efforts are being made to  
 48 observe gamma rays indirectly via ground-based experiments as well, by detecting the secondary particles  
 49 and the Cherenkov light produced by their passage through the Earth's atmosphere. In the energy range  
 50 between approximately 100 MeV and 100 GeV, gamma ray telescopes on satellites such as the Fermi

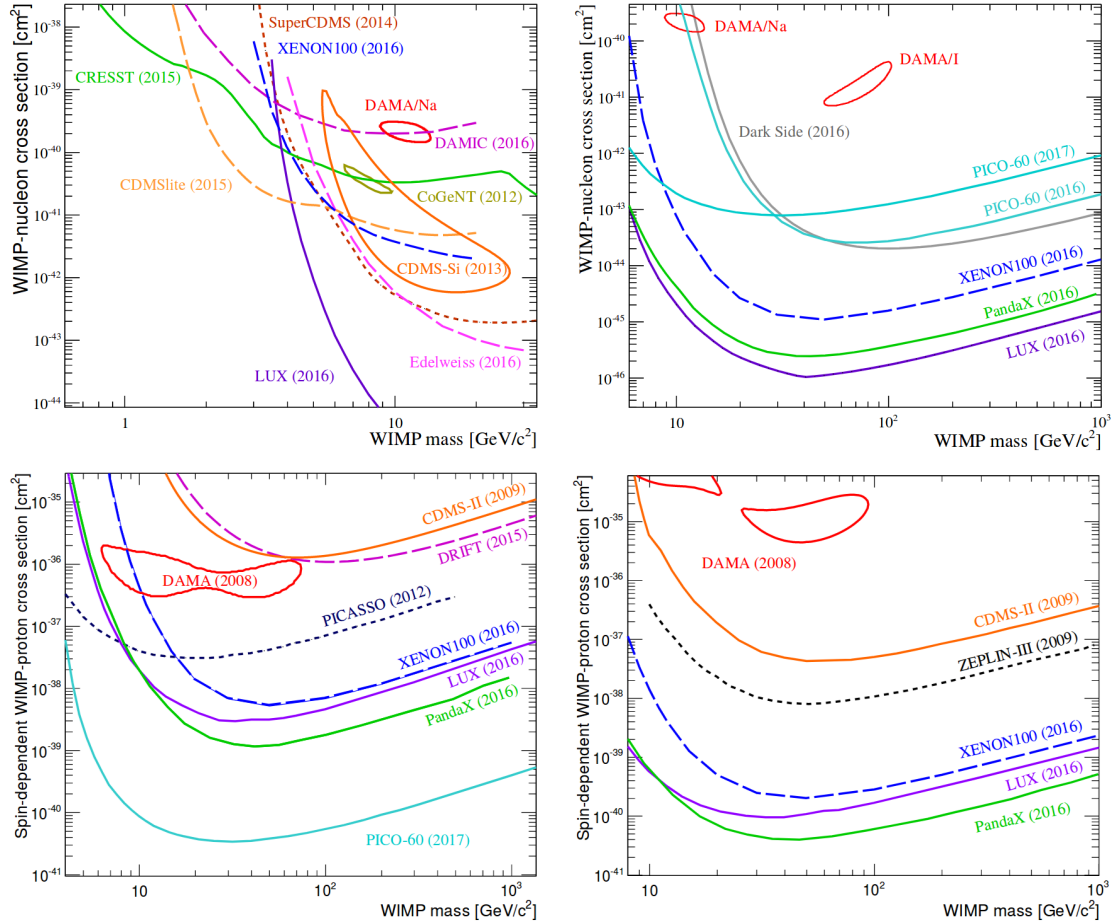


*Figure 2.7: Overview of the current limits for spin-independent WIMP-nucleon interactions at low (top left) and high (top right) WIMP masses, spin-dependent WIMP-proton interactions (bottom left), and spin-dependent WIMP-neutron interactions (bottom right). The observed signals from DAMA, CoGeNT, and CDMS-Si are shown as well. Figure taken from [55].*

1 Large Area Telescope [56] are being used. Above 100 GeV, the ground-based Imaging Air Cherenkov  
 2 Telescopes such as HESS [57], MAGIC [58], and VERITAS [59] become more adequate.

3 Neutrinos can also be produced in the annihilation of dark matter particles, but they are considerably  
 4 more difficult to detect than gamma rays due to their weak interaction with ordinary matter. They are  
 5 not easily absorbed, which makes it possible to observe them with underground, low-background ex-  
 6 periments. Very energetic neutrinos, in the GeV-TeV range, are most easily observed by detecting the  
 7 Cherenkov light from muons produced through charge current interactions of the neutrinos inside of or  
 8 close to the detector volume. Two very large neutrino detectors are ANTARES in the Mediterranean  
 9 Sea [60] and IceCube at the South Pole [61].

10 Additionally, evidence for dark matter annihilations can also be found by studying the spectra of  
 11 cosmic positrons and antiprotons. Contrary to neutrinos and gamma rays, these charged particles do not  
 12 point to their source, as their trajectory is modified by the presence of galactic magnetic fields. Currently,  
 13 the main detector for positrons and antiprotons is AMS [62], which is operating on the International Space  
 14 Station. Until 2016, PAMELA [63] was also active on board of the Resurs-DK1 satellite.

15 Finally, radio emissions from the galactic halo, and in particular from the galactic centre, can also  
 16 provide evidence for dark matter annihilation. Electrons and protons produced in dark matter annihi-  
 17 lations will emit synchrotron radiation at radio wavelengths as they move through galactic magnetic fields.  
 18 This type of searches is performed with radio telescopes and belongs to the realm of classical astronomy.

### 2.2.3.3 Collider experiments

Since dark matter particles are usually assumed to be neutral and to interact only weakly with ordinary matter, they are expected to pass through the detectors at colliders without leaving a signal, similar to neutrinos. These particles can however still be searched for at colliders as well, when they are produced in association with other visible particles which are detected as jets or charged leptons. The dark matter particles are then observed as missing energy, as they create an imbalance in the net momentum in the transverse plane perpendicular to the colliding beams, which should be zero. One of these flagship analyses is the monojet analysis, looking for dark matter produced together with one or more jets [64, 65]. Similarly, many more searches are performed at the CMS and ATLAS experiments at the LHC by looking for signatures containing missing energy. Recent summaries are given in [66] and [67].

Additionally, other signatures without missing energy can also be used to search for dark matter. If the dark matter particle is produced in a cascade of decays for example, different signatures can be obtained, such as displaced vertices [68], disappearing tracks [69], and displaced lepton-jets [70]. Furthermore, in dijet searches [71–73], resonances in the mass spectrum are being looked for, as this could point to the existence of a new dark matter mediator. If the dark matter particles couple to quarks via a dark matter mediator, this mediator can either decay to a pair of dark matter particles or a pair of Standard model quarks which can be observed as a pair of jets. Finally, for some particular types of dark matter candidates, such as strongly interacting massive particles (SIMPs) [74] or heavy stable neutral particles (HSCPs) [75, 76], more unusual signatures are expected. This is currently a developing area of dark matter research, and more and more searches looking for new signatures are appearing.

In Figures 2.8 and 2.9, recent limits from dark matter searches at the CMS experiment are compared to the direct detection results, for spin-dependent and spin-independent interactions, respectively.

## 2.3 Strongly Interacting Massive Particles

As no observation of dark matter has been made so far, despite many searches probing the more popular models described in the previous section, many scenarios now venture beyond minimal models or give up basic assumptions for the WIMP. In the following model, which is studied in this thesis, the interaction cross section of the dark matter with normal matter is so high that the particles are no longer WIMPs, but so-called strongly interacting massive particles (SIMPs). This model can also be motivated by the long lasting interest for self-interacting dark matter (SIDM)<sup>4</sup> particles with a large cross section [42], which could help to explain observations that present a challenge for the cold dark matter scenarios, such as the missing satellites or core-cusp problems [78–81]. While it is possible to create models with a strongly interacting hidden sector that is weakly coupled to the Standard Model particles, SIDM particles that interact rather strongly with the known matter particles can be considered as well.

### 2.3.1 The SIMP simplified model

In this simplified model, the dark matter particles  $\chi$  can be produced at the LHC in pairs, through a new strong interaction with a new mediator  $\phi$ , as illustrated in Figure 2.10. These SIMPs are neutral and stable, and are generated off-shell as the mediator is very light, of the order of the pion mass:  $m_\phi = 140$  MeV. We only consider the case of fermionic candidates, since the bosonic form is ruled out by constraints coming from neutron stars and black holes, as is described in Section 2.3.2. Both the cases with a scalar or a vector mediator can be studied, and the corresponding interaction Lagrangian is

$$\mathcal{L}_{\text{int}} = \begin{cases} -g_\chi \phi \bar{\chi} \chi - g_q \phi \bar{q} q & (\text{scalar mediator}) \\ -\tilde{g}_\chi \phi_\mu \bar{\chi} \gamma^\mu \chi - \tilde{g}_q \phi_\mu \bar{q} \gamma^\mu q & (\text{vector mediator}) \end{cases} \quad (2.17)$$

with  $g_\chi g_q, \tilde{g}_\chi \tilde{g}_q < 0$  to avoid the formation of bound states. For simplicity we assume that the SIMPs have a universal coupling to quarks, although a flavour dependent coupling could be preferred, as light SIMPs with a significant coupling to  $b$  or  $c$  quarks are probably constrained by  $B$  and  $D$  meson phenomenology.

<sup>4</sup>Incidentally, self-interacting and strongly interacting share the same abbreviation, such that SIDM can also stand for strongly interacting dark matter and SIMP for self-interacting massive particles in the literature.

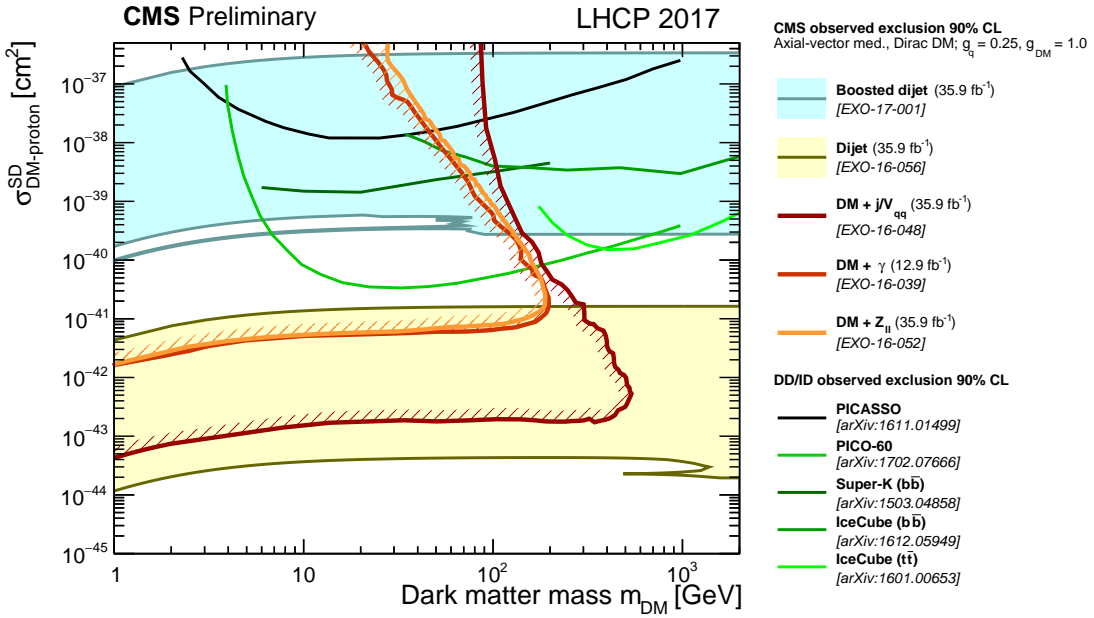


Figure 2.8: A comparison of CMS results to direct detection experiments in the  $m_{DM} - \sigma_{SD}$  plane. The limits are shown at 90% CL. The shown CMS contours are for an axial-vector mediator with Dirac dark matter and couplings  $g_q = 0.25$  and  $g_{DM} = 1.0$ . The spin-dependent exclusion contours are compared with limits from the PICASSO and PICO experiments, the IceCube limit for the  $t\bar{t}$  and  $b\bar{b}$  annihilation channels, and the Super-Kamiokande limit for the  $b\bar{b}$  annihilation channel. It should be noted that the CMS limits do not include a constraint on the relic density and also the absolute exclusion of the different CMS searches as well as their relative importance will strongly depend on the chosen coupling and model scenario. Therefore, the shown CMS exclusion regions in this plot are not applicable to other choices of coupling values or models. Figure taken from [77].

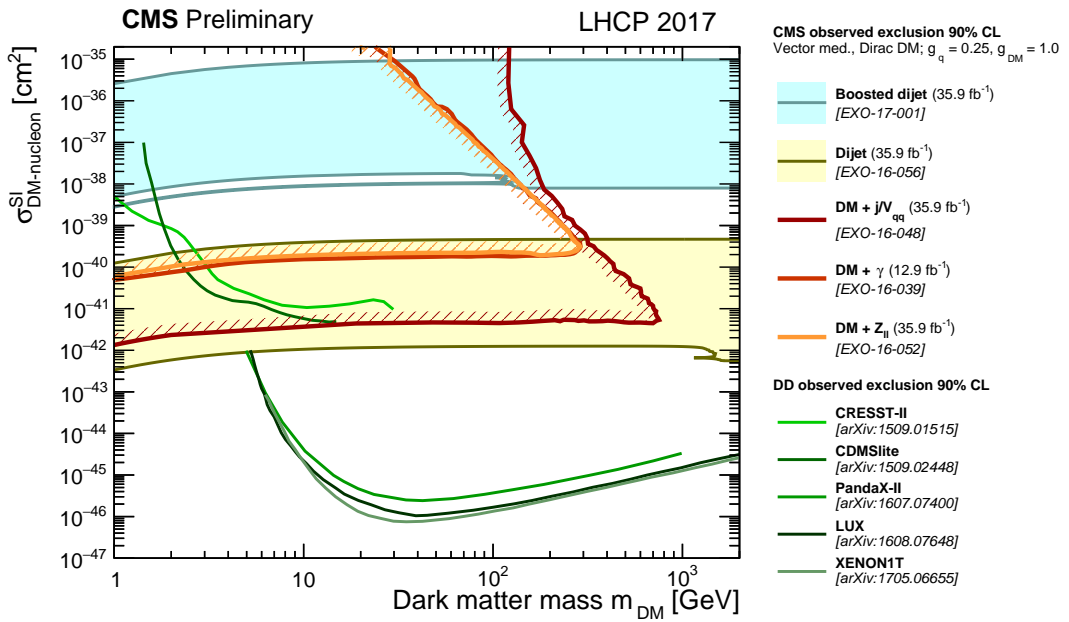


Figure 2.9: A comparison of CMS results to direct detection experiments in the  $m_{DM} - \sigma_{SI}$  plane. The limits are shown at 90% CL. The shown CMS contours are for a vector mediator with Dirac dark matter and couplings  $g_q = 0.25$  and  $g_{DM} = 1.0$ . The spin-independent exclusion contours are compared with the XENON17, LUX 2016, PandaX-II 2016, CDMSlite 2015 and CRESST-II 2015 limits, which constitutes the strongest documented constraints in the shown mass range. It should be noted that the CMS limits do not include a constraint on the relic density and also the absolute exclusion of the different CMS searches as well as their relative importance will strongly depend on the chosen coupling and model scenario. Therefore, the shown CMS exclusion regions in this plot are not applicable to other choices of coupling values or models. Figure taken from [77].

- <sup>1</sup> SIMPs lighter than about 5 GeV could for example appear in the decay of  $b$  or  $c$  quarks, and would be  
<sup>2</sup> constrained by limits on the invisible decay of B and D mesons.

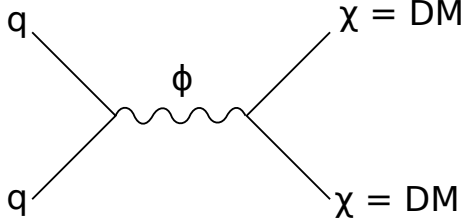


Figure 2.10: Feynman diagram showing the production of a SIMP pair, through a new low-mass mediator.

<sup>3</sup> Introducing a new strong interaction between quarks can however modify nuclear potentials. In order  
<sup>4</sup> to keep the impact small, the mediator is assumed to not modify nuclear potentials by more than  $\mathcal{O}(10\%)$ ,  
<sup>5</sup> such that  $g_{\chi N} \lesssim 0.3 g_{\pi NN} \sim 3$  for a mediator with the mass of a pion, where  $g_{\pi NN} \sim 13$  is the  
<sup>6</sup> effective pseudoscalar pion-nucleon coupling [82]. The quoted values are however not very precise, as  
<sup>7</sup> a large spread of values can be found in the literature for meson-nucleon effective couplings, sometimes  
<sup>8</sup> differing by a factor 2 or more (see e.g. [83] for comparison). This shows the difficulty of dealing with  
<sup>9</sup> strong interactions in the framework of effective field theories, which arise because contributions from  
<sup>10</sup> many mesons need to be taken into account, each of them with a different coupling. No constraints on  
<sup>11</sup> modified strong interactions at low energies seem to exist in literature so far, however searches at fixed-  
<sup>12</sup> target experiments do place constraints on the existence of strongly interacting stable neutral particles.

<sup>13</sup> In summary, the model has 4 free parameters: the two couplings, the mass of the mediator  $m_\phi$ , and  
<sup>14</sup> the mass of the SIMP  $m_\chi$ . At the LHC, only the product of the couplings appears, while astrophysical  
<sup>15</sup> observations constrain both the dark matter self-interaction and the interaction with the Standard Model.

### <sup>16</sup> 2.3.2 Experimental constraints

<sup>17</sup> Naively, one would expect such an unusual model with strong interactions not to be viable, as various  
<sup>18</sup> types of experiments and observations set constraints on SIMPs as dark matter candidates. However,  
<sup>19</sup> some of these limitations can be avoided by the assumptions in the model described above. The relevant  
<sup>20</sup> existing measurements are described below, showing there is still a part of phase space which remained  
<sup>21</sup> unexplored so far.

#### <sup>22</sup> Bound states

<sup>23</sup> Searches for heavy isotopes, in particular heavy water, constrain the formation of bound states  
<sup>24</sup> between SIMPs and nucleons, ruling out particles with a mass below 10 TeV for the scenario  
<sup>25</sup> with SIMPs as dominant contribution to dark matter. This constraint is evaded by assuming a  
<sup>26</sup> purely repulsive SIMP-nucleon interaction with opposite sign couplings, as is specified in the La-  
<sup>27</sup> grangian (2.17). In the vector mediator case, vector mediators would however couple to the dark  
<sup>28</sup> matter antiparticles with an opposite charge. This is avoided if no dark matter antiparticles are  
<sup>29</sup> around, i.e. if the abundance of dark matter is asymmetric. A reason for having asymmetric SIMPs  
<sup>30</sup> is that if they are the dominant source of dark matter, then the dark matter abundance is set by either  
<sup>31</sup> an asymmetry or through a non-thermal mechanism. In the case of a symmetric SIMP candidate,  
<sup>32</sup> the dark matter abundance is determined by thermal freeze-out, and it can only be a sub-dominant  
<sup>33</sup> component. Additional constraints also exist on the dark matter self-interacting strength from halo  
<sup>34</sup> shapes and merging galaxies such as the Bullet cluster [84, 85].

#### <sup>35</sup> Earth heating

<sup>36</sup> A second argument for an asymmetric abundance of SIMPs comes from experiments measuring the  
<sup>37</sup> heat emitted from the Earth's core. For the typical SIMPs cross sections, the dark matter particles  
<sup>38</sup> can be captured by the Earth and accumulate in its core over time. Annihilating SIMPs would then

provide a substantial source of heat and could modify the Earth's heat flow. This can be measured by detectors in deep underground shafts [86] and rules out the scenario with symmetric SIMPs.

### Neutron stars and black holes

In the asymmetric scenario, light scalar dark matter particles can however be collected in the cores of neutron stars and cause them to collapse into black holes. Bosonic dark matter candidates are therefore excluded, and we consider only fermionic candidates as mentioned previously.

### Direct detection searches

Many bounds on the SIMP parameter space also come from the direct detection searches. Underground experiments, such as CDMS and XENON, place strong constraints at smaller cross sections, about 5 orders of magnitude below the SIMP cross section, as can be seen from Figure 2.11. At the higher cross sections considered here, the SIMPs are stopped by the Earth's atmosphere, and they cannot reach the underground detectors. At higher altitudes however, space or airborne experiments such as RSS [87], a balloon-based experiment with a silicon semiconductor detector, and XQC [88], a sounding rocket experiment, exclude SIMPs in some regions of phase space. More details on these constraints can be found in [86], where they have been extensively reviewed.

### Nucleosynthesis and cosmic rays

There are also bounds from primordial nucleosynthesis and cosmic rays, reviewed in [89] and [90]. The protons in cosmic rays can scatter off dark matter particles and create neutral pions, which decay to photons and could be detected in gamma ray telescopes. Although limits have been placed on dark matter-nucleon interactions [90], these constraints depend on many assumptions and adopt a form of the dark matter density near the galactic core. Since the considered model describes a nonstandard form of dark matter with a relatively strong interaction with baryons, these densities may be considerably different.

### CMB and large scale structure

Observations of the CMB anisotropies and the large scale structure power spectrum, including from the Lyman- $\alpha$  data [91, 92] additionally also place strong constraints on interactions between dark matter and baryons.

### Fixed-target experiments

Finally, a relatively old fixed-target experiment led in 1976 at FNAL with a beam of neutral particles produced by 300 GeV protons hitting a beryllium target was used to look for massive, strongly interacting, neutral particles [93]. The mass of the particles was determined using their flight time and their kinetic energy which was measured in a calorimeter. Neutral particles with a mass larger than 2 GeV were searched for, in order to discriminate the candidates from the background of neutrons and lighter hadronic states, up to  $m_\chi \lesssim \sqrt{E/2} \approx 12$  GeV, limited by the beam energy of  $E = 300$  GeV. Single particle production was considered, but the results apply to pair production as well when they are translated into the case where 2 neutral particles are boosted and fly away in the same direction. The search showed no significant excess above the expected background and limits were placed on the invariant production cross section per nucleon versus the neutral particle interaction cross section. As an example, for an interaction cross section of 1 mb, a limit on the total production cross section of about  $2.5 \times 10^{-35}$  cm $^2 = 25$  pb is found, and this limit is reported by the Particle Data Group [94]. Comparing the considered SIMP model to this result by simulating the pair production at  $\sqrt{s} = 25$  GeV, one can conclude that SIMPs between 2 and about 6 GeV are already excluded by this experiment [95].

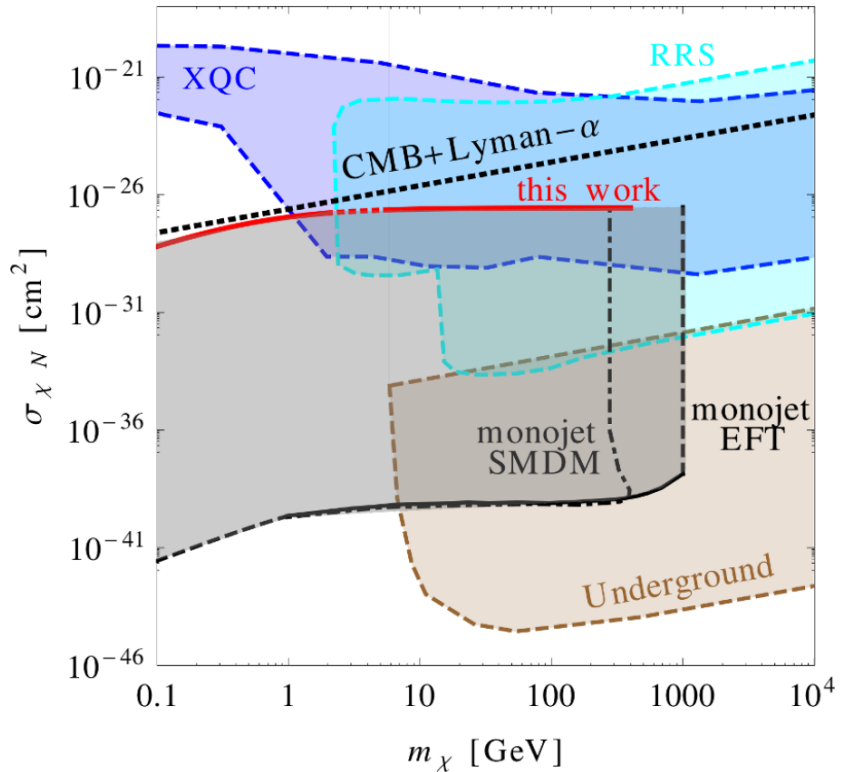


*Figure 2.11: Summary plot showing the SIMP model (red) in comparison with the most important applicable constraints, coming from the LHC monojet analyses (black), the atmospheric XQC and RRS experiments (blue), underground experiments (brown), and the CMB observations and Lyman- $\alpha$  data (black dashed line). Figure taken from [95].*



# 3

## The LHC and the CMS Detector

In order to investigate the currently unsolved mysteries of particle physics, such as the existence of dark matter, many experiments can be conducted, among other things at particle colliders. The largest particle accelerator in the world is the LHC, located at the European Organization for Nuclear Research (CERN) in Geneva, Switzerland. At this accelerator, protons are being accelerated at energies up to 6.5 TeV, giving rise to a record centre-of-mass energy of 13 TeV in the proton collisions. Using data from the collisions generated at the interaction points along the accelerator ring, the Standard Model can be tested in many ways and searches for particles beyond the Standard Model can be performed.

In Section 3.1 more details are given about the LHC and the 4 main experiments situated at the interaction points. In particular, the general-purpose Compact Muon Solenoid (CMS) detector is described in Section 3.2.

### 3.1 The Large Hadron Collider at CERN

The LHC was built in the already existing Large Electron Positron (LEP) collider tunnel, which was excavated in the 1980's and has a circumference of 27.6 km. Contrary to the LEP collider, the LHC accelerates particles of the same charge, namely protons or lead ions. Much higher luminosities can therefore be reached, since only particles are used and the generation of antiparticles is not needed. This was the limiting factor at the Tevatron, where protons and antiprotons were used. Additionally, at the probed energies the colliding particles are not the protons or ions, but their constituents, which carry a varying fraction of the total momentum. This makes the LHC an ideal instrument for exploration at higher energies, as the collisions naturally cover a wide energy range.

#### 3.1.1 The LHC injector chain

The protons (or lead ions) can not directly be injected in the LHC, but need to be accelerated gradually in several pre-accelerators, as illustrated in Figure 3.1. For the proton beams, the LHC injection chain starts at a bottle of hydrogen, where protons are stripped from the hydrogen atoms and accelerated up to 50 MeV by a linear accelerator (LINAC2). The protons are then transferred to a chain of circular accelerators, starting with the Proton Synchrotron Booster (PSB) which accelerates them to an energy of 1.4 GeV. Next, the protons go through the Proton Synchrotron (PS) and are delivered to the Super Proton Synchrotron (SPS) at an energy of 26 GeV. Finally, the protons are injected in the LHC in opposite direction with an energy of 450 GeV.

The lead ions are first accelerated in a different linear accelerator, LINAC3, before being injected in the Low Energy Ion Ring (LEIR) at an energy of 4.5 MeV per nucleon. Here the ions are accelerated

to an energy of 72 MeV per nucleon, and they then follow the same path as the protons through the PS, where they are accelerated to 5.9 GeV and stripped from the last of their electrons, and the SPS, where they are accelerated to 177 GeV. The record centre-of-mass energy for heavy ion collisions at the LHC so far has been 5.02 TeV and 8.16 TeV, for lead-lead (Pb-Pb) and proton-lead (p-Pb) collisions in 2015 and 2016, respectively.

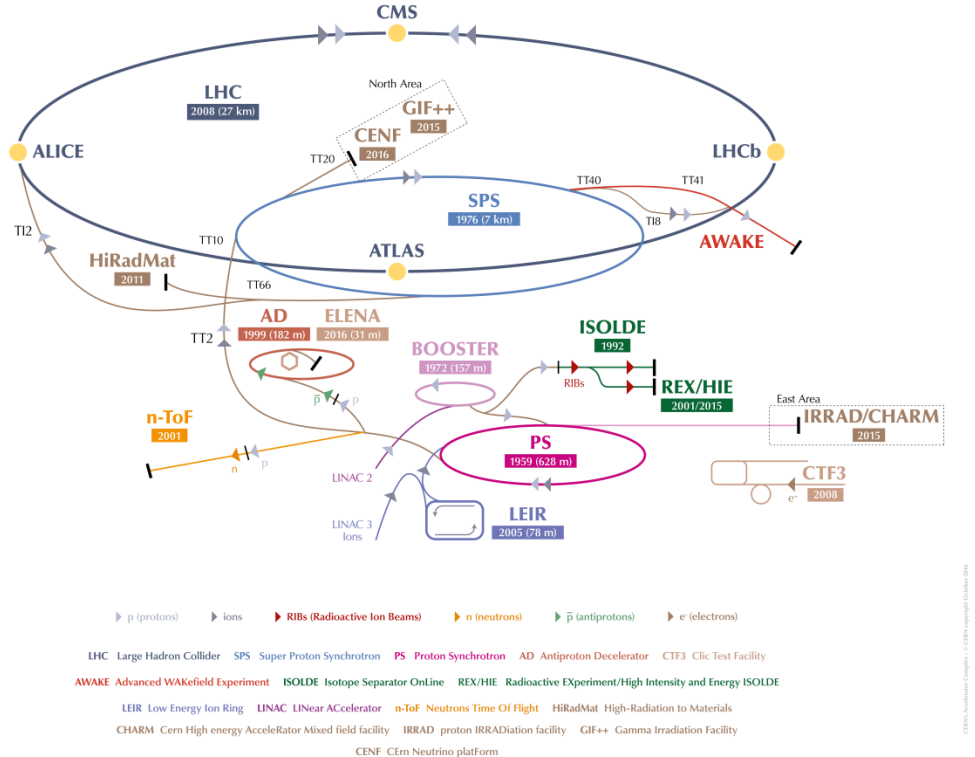


Figure 3.1: Schematic view of the various linear and circular accelerators of the CERN accelerator complex, including the LHC injection chain. Figure taken from [96].

### 3.1.2 The Large Hadron Collider

The most relevant specifications for a particle physics accelerator are the maximum energy and the luminosity that can be reached. High energy is necessary in order to be able to create new heavy particles, which are for example predicted in many theories beyond the Standard Model.

The protons are kept on the correct orbit by the 1232 LHC dipole magnets. These magnets are cooled down to 1.9 K with liquid Helium and supplied with a current of 12 kA to reach the design field of 8.33 T. This limits the maximum beam momentum of the accelerator to

$$p = B/\rho = 8.33 \text{ T}/2804 \text{ m} = 7 \text{ TeV}/c, \quad (3.1)$$

with  $\rho$  the bending radius of the tunnel. The protons are accelerated up to the desired energy by radio-frequency (RF) cavities, which produce an oscillating electric field.

A high event rate or luminosity  $\mathcal{L}$  is equally important, to obtain a sufficiently high number of collisions. For a process with cross section  $\sigma$ , this rate is

$$\frac{dN}{dt} = \mathcal{L}\sigma. \quad (3.2)$$

In order to achieve the high design luminosity of  $10^{34} \text{ cm}^{-2}\text{s}^{-1}$  in the LHC, the protons are concentrated in bunches which are focused by strong quadrupole magnets around the interaction regions. The RF

frequency is 400 MHz, which corresponds to a wavelength of 75 cm and confines the protons into buckets of 2.5 ns. The LHC circumference would then allow for 35640 buckets in total, which would result in bunch crossings spaced by only 37.5 cm. A more realistic spacing is 25 ns, corresponding to one bunch per 10 RF buckets. Additionally, 225 ns gaps are present between the bunch trains, corresponding to the rise time of the injection kicker magnets. One gap of 3  $\mu$ s is necessary as well to allow clean beam dumps. These requirements limit the number of bunches to a maximum of 2808.

After almost 25 years of design and construction, the LHC was completed in 2008 and the commissioning of the machine started. However, during a powering test on 19 September of the same year an electric arc developed inside a bus bar which led to a large release of helium and a pressure wave that caused extensive mechanical damage to the affected LHC sector. This incident delayed the first collisions, with one bunch per beam and at a beam energy of 900 GeV, until late 2009. During 2010 and 2011 a centre-of-mass energy of 7 TeV was used for the collisions, which was then increased to 8 TeV in 2012. The instantaneous luminosity was also increased, starting from  $2 \times 10^{32} \text{ cm}^{-2}\text{s}^{-1}$  in 2010 to more than  $6 \times 10^{33} \text{ cm}^{-2}\text{s}^{-1}$  in 2012. During the 3 years of data-taking in Run 1, data corresponding to an integrated luminosity of  $45.0 \text{ pb}^{-1}$ ,  $6.1 \text{ fb}^{-1}$ , and  $23.3 \text{ fb}^{-1}$ , respectively, were delivered. After Run 1, a long shutdown (LS1) of 2 years followed, which was used to correct the problems that were discovered in the aftermath of the incident at the startup in 2008, and to upgrade and consolidate the experiments located on the LHC ring.

In 2015, the LHC restarted operations with Run 2, at an even higher centre-of-mass energy of 13 TeV. During 2016 the design luminosity of  $10^{34} \text{ cm}^{-2}\text{s}^{-1}$  was exceeded and a total of  $41 \text{ fb}^{-1}$  of data were delivered. A comparison of the delivered integrated luminosity per year is shown in Figure 3.2.

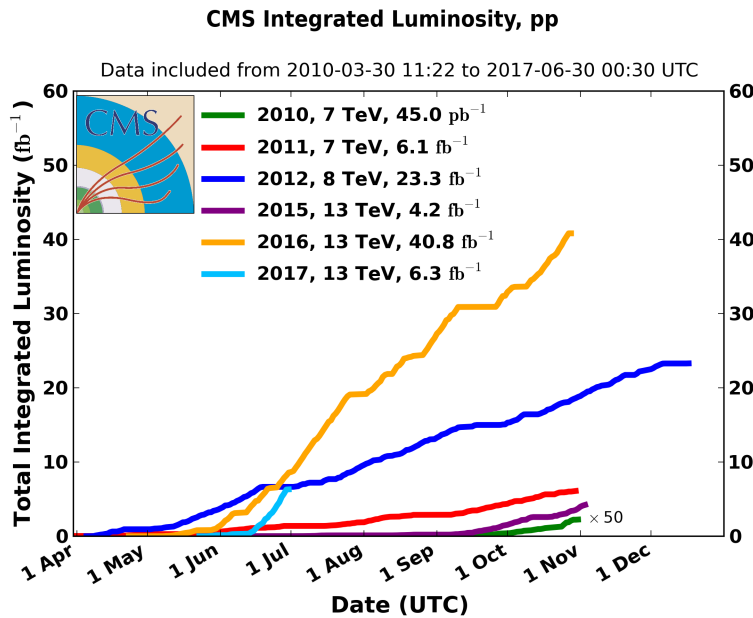


Figure 3.2: Overview of the integrated luminosity delivered to the CMS detector during Run 1 (2010 to 2012) and Run 2 (2015 to 2017).

### 3.1.3 The experiments at the LHC

There are four interaction points (IPs) where the proton or lead ion beams of the LHC can collide, and around each of these points large particle detectors were built in order to record the generated collisions. The ATLAS and CMS detectors, located at IP1 and IP5, are both high luminosity general-purpose detectors and consist of several layers surrounding the IP in an onion-like structure to avoid particles escaping detection. These detectors can cover a wide range of high energy physics, from precision measurements of the Standard Model to searches beyond the Standard Model. At IP2 the ALICE detector is specialized in heavy ion collisions with low instantaneous luminosities, around  $10^{27} \text{ cm}^{-2}\text{s}^{-1}$ . With

this detector information is gathered about the quark-gluon plasma, a state of matter that exists at extremely high temperatures and densities where quarks and gluons are no longer confined in hadrons. The fourth main detector, LHCb, is located at IP8 and requires instantaneous luminosities of the order of a few  $10^{32} \text{ cm}^{-2} \text{ s}^{-1}$ . Using this detector  $b$  quarks are being studied, focusing among other things on the matter-antimatter asymmetry in the universe.

## 3.2 The CMS detector

The searches described in this thesis were conducted using data collected with the CMS detector, a general-purpose detector located on the LHC ring. It consists of the typical components of a particle physics detector, namely a tracker, an electromagnetic calorimeter (ECAL), a hadronic calorimeter (HCAL), a solenoidal magnet, and muon detectors. One peculiar aspect is however that both calorimeters are situated inside the superconducting magnet. This design was chosen in order to improve the energy resolution by reducing the amount of material in front of the calorimeters. The overall detector has a length of 21.6 m, a diameter of 14.6 m and a total weight of 12500 t. A schematic overview is shown in Figure 3.3.

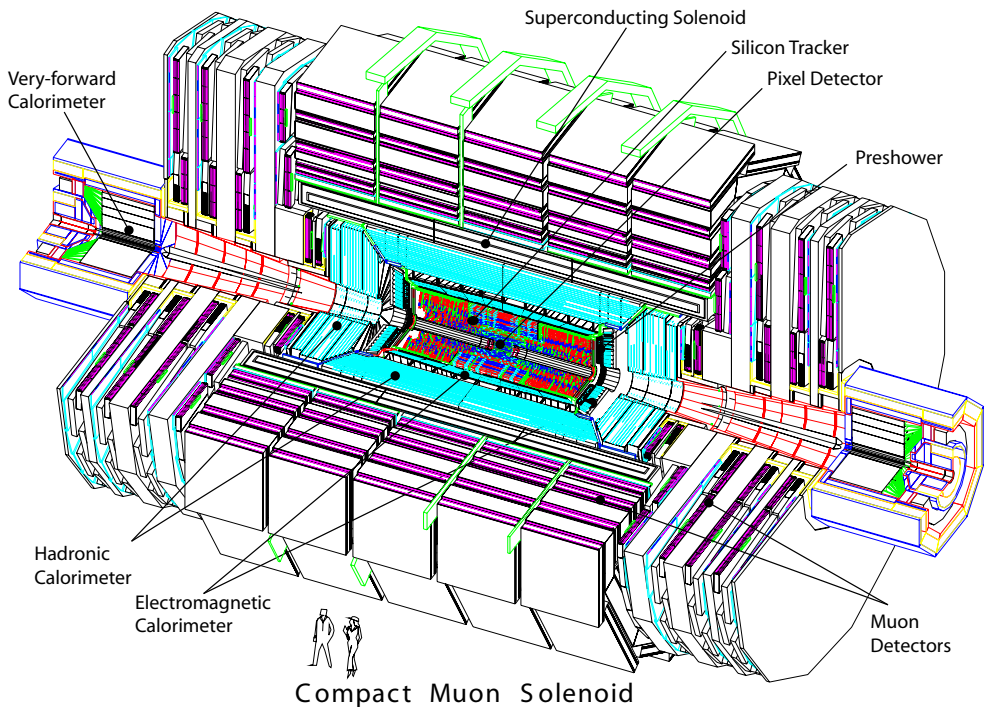


Figure 3.3: The CMS detector, consisting of the pixel and strip tracker, the electromagnetic calorimeter (ECAL) with preshower, the hadronic calorimeter (HCAL) with its forward component, and the muon systems. Figure taken from [97].

The CMS coordinate system places the origin at the nominal collision point. The  $x$  axis is perpendicular to the beam and points towards the centre of the LHC ring, the  $y$  axis is vertical and pointing upwards, and the  $z$  axis is defined anticlockwise along the beam direction. The azimuthal angle  $\phi$  is then defined in the  $xy$  plane, relative to the  $x$  axis and the polar angle  $\theta$  is measured with respect to the  $z$  axis. In general, the polar angle is converted into the pseudorapidity

$$\eta = -\ln \left( \tan \frac{\theta}{2} \right) \quad (3.3)$$

for convenience, since differences in pseudorapidity are invariant under Lorentz boosts along the  $z$  axis. A pseudorapidity of 0 corresponds to the direction perpendicular to the beam ( $\theta = \pi/2$ ), and an infinite pseudorapidity corresponds to the direction parallel to the beam ( $\theta = 0$ ).

1 Due to the conservation of momentum before and after the collision, the momenta of the particles in  
 2 the final state of a collision should be balanced in the transverse plane. Another variable that is therefore  
 3 often used in particle physics is the transverse momentum of a particle, defined as

$$p_T = p \cdot \sin \theta. \quad (3.4)$$

#### 4 **3.2.1 The tracker**

5 The innermost part of the CMS detector, closest to the IP, is the tracking system, which is designed to  
 6 provide a precise measurement of the trajectories of charged particles. This all-silicon detector is divided  
 7 into a pixel and a strip detector, with a layout as shown in Figure 3.4. The inner part, consisting of pixel  
 8 modules, provides very precise 3D hits, which are important for vertex reconstruction and track seeding.  
 9 This allows to have a precise measurement of secondary vertices and track impact parameters, necessary  
 10 for the efficient identification of e.g. heavy flavour particles. As the hit occupancy is lower in the outer  
 11 part of the detector, a larger cell size can be afforded, and silicon strips are used instead of pixels. This  
 12 strip detector provides a large lever arm and a link to the calorimeters and the muon system. The tracker  
 13 covers a pseudorapidity range  $|\eta| < 2.5$ .

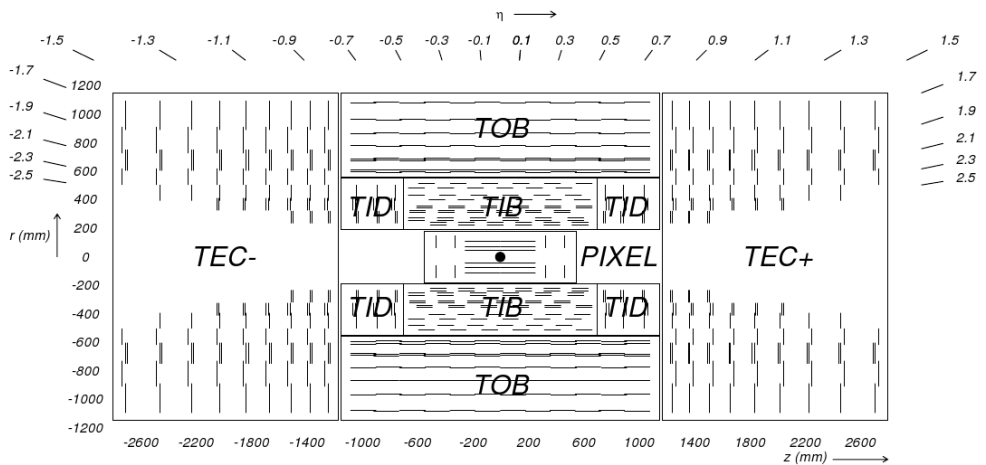


Figure 3.4: A transverse view of the pixel and strip tracker detectors. Figure taken from [97].

##### 14 **3.2.1.1 The pixel tracker**

15 The pixel tracker was replaced during the extended technical stop in 2016 and 2017 [98], as a part of the  
 16 CMS Phase 1 upgrades. As the data used for this thesis were recorded before that, only the so-called  
 17 Phase 0 detector is described here.

18 For the pixel modules n+ pixels on n-substrate are used, allowing the sensors to also work in under-  
 19 depletion after type inversion. The 1440 modules are arranged in several cylindrical layers and disks, as  
 20 illustrated in Figure 3.4. The barrel, consisting of 3 pixel layers surrounding the beam pipe at radii of 4.4,  
 21 7.3 and 10.2 cm, is complemented by the forward pixel detector, composed of 2 endcap disks on each  
 22 side extending from 6 to 15 cm in radius. The barrel and the forward parts contain respectively 48 million  
 23 and 18 million pixels with a size of  $100 \times 150 \mu\text{m}^2$ , covering a total area of  $1.06 \text{ m}^2$ .

24 In the barrel, the magnetic field of CMS is perpendicular to the drift of the electrons to the collecting  
 25 pixels, which results in a Lorentz drift. This drift leads to a spread of the charge over several pixels.  
 26 Since the read-out of the modules is analogue, an improved spatial resolution can therefore be achieved  
 27 with charge interpolation. In the forward pixel detector the drift of the electrons would be parallel to the  
 28 magnetic field so in order to profit from the Lorentz angle, the modules are tilted by  $20^\circ$  in a turbine-  
 29 like arrangement, as can be seen in Figure 3.5. A spatial resolution of  $10 \mu\text{m}$  ( $30 \mu\text{m}$ ) can be achieved  
 30 in the local directions  $x$  ( $y$ ) of the module, respectively. In the barrel  $x$  is the longitudinal direction  
 31 perpendicular to the beam and  $y$  is the longitudinal direction parallel to the beam.

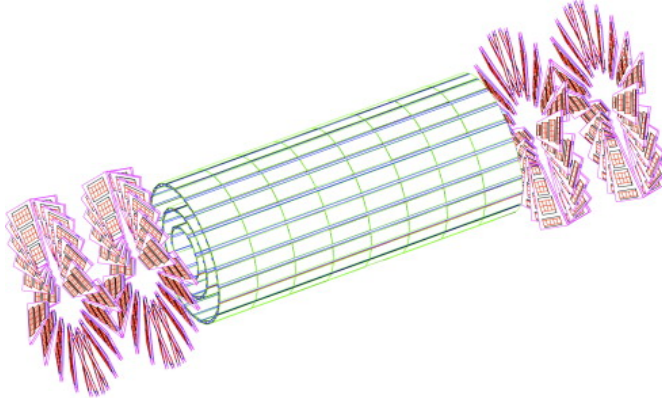


*Figure 3.5: A 3D view of the barrel and forward pixel detector. Figure taken from [99].*

1     The signals from the pixel sensors are read out by custom read-out chips (ROCs), which amplify  
2 and store the signals, and already apply zero-suppression on-detector. The data rate from the detector  
3 to the Front End Drivers (FEDs) is therefore not constant for every event. Additionally, if there are  
4 too many hits on a pixel module for a given event, they can not all be stored on the finite buffer of the  
5 ROC. Consequently, as the instantaneous luminosity increases the pixel modules start to show a “dynamic  
6 inefficiency” which is most pronounced in the first layer, closest to the beampipe. This was one of the  
7 main motivations for the Phase 1 upgrade of the pixel detector.

### 8     **3.2.1.2 The strip tracker**

9     The outer part of the tracker consists of 15 148 strip modules, which are distributed among multiple  
10 barrel layers and endcap disks and make up a total active area of  $198 \text{ m}^2$ . The inner part is composed of  
11 4 Tracker Inner Barrel (TIB) layers with 3 Tracker Inner Disks (TID) on each side. Surrounding these  
12 are 6 Tracker Outer Barrel (TOB) layers and the 2 Tracker EndCaps (TEC), which are composed of 9  
13 disks. This geometric arrangement is shown in Figure 3.4, with double lines to indicate back-to-back  
14 modules. These so-called double-sided modules are mounted with a stereo angle of 100 mrad to improve  
15 the 3D point resolution by providing a measurement of the  $z$  and  $r$  coordinate in the barrel and disks,  
16 respectively. The choice of strip pitches is driven by the two particle separation capability and two-hit  
17 resolution, and ranges from  $80 \mu\text{m}$  to  $205 \mu\text{m}$ . The length of the strips varies from 63 mm to 117 mm,  
18 minimizing the occupancy and noise levels.

19     In the TOB and the 3 outermost rings of the TEC two silicon sensors are daisy chained, while single  
20 sensors are used in the inner part. This is done to limit the number of read-out channels, since the area  
21 that had to be instrumented is larger in the outer region. The larger cell size can be afforded due to the  
22 lower occupancy in the outer part. However, the noise of the sensors also increases with strip length, so  
23 thicker silicon sensors,  $500 \mu\text{m}$  compared to  $320 \mu\text{m}$  in the inner part, are used in order to collect more  
24 signal per traversing particle.

25     The strip sensors are single sided p-on-n type silicon. The signals from the sensors are amplified,  
26 shaped, and stored by 4 or 6 custom APV25 chips per module. When the trigger has made a positive  
27 decision, the analogue signals from two APV25 chips are multiplexed and sent to the FED boards in the  
28 service cavern via optical fibres, where they are converted to digital signals. The FEDs then perform  
29 pedestal and common mode subtraction as well as cluster finding. Additionally, the data is sparsified  
30 in these off-detector electronics, before being sent to the CMS central data acquisition (DAQ). Due to  
31 charge sharing, this analogue read-out scheme also results in an improved spatial resolution of 15 to 40  
32  $\mu\text{m}$ , depending on the position of the modules and the strip pitch.

### 33     **3.2.2 The electromagnetic calorimeter**

34     Surrounding the tracker, the CMS electromagnetic calorimeter (ECAL) is designed to measure the en-  
35 ergy of photons and electrons. It is composed of 75 848 lead tungstate ( $\text{PbWO}_4$ ) crystals arranged in a

1 cylindrical barrel and 2 endcaps. The barrel crystals measure  $22 \times 22 \text{ mm}^2$  at the front face of crystal,  
 2 and  $26 \times 26 \text{ mm}^2$  at the rear face, which corresponds to approximately  $0.0174 \times 0.0174$  in  $\eta\phi$ . The  
 3 length of the crystal is 230 mm, corresponding to 25.8 radiation lengths. In the endcaps, the crystals have  
 4 a rear face cross section of  $30 \times 30 \text{ mm}^2$ , front face cross section of  $28.62 \times 28.62 \text{ mm}^2$ , and a length of  
 5 220 mm, corresponding to 24.7 radiation lengths.

6 The high density material was chosen due to its short radiation length and small Moli  re radius,  
 7 resulting in a small spread of the electromagnetic shower generated by an incoming photon or electron.  
 8 This allows for a fine granularity, a better shower separation, and a compact calorimeter. Additionally,  
 9 this scintillating material has a fast response, as about 80% of the light is emitted during the first 25 ns.  
 10 The scintillation light is collected by photodetectors, digitized, and read out.

11 The layout of the ECAL is shown in Figure 3.6, with the barrel (EB) extending up to  $|\eta| < 1.470$   
 12 and the endcaps (EE) on each side covering the range  $1.479 < |\eta| < 3.0$ . A preshower detector (ES)  
 13 is positioned in front of the endcap crystals, covering the pseudorapidity range between  $|\eta| = 1.653$   
 14 and  $|\eta| = 2.6$ . This detector consists of a layer of lead which initiates an electromagnetic shower from  
 15 incoming photons or electrons, and a layer of silicon sensors which measures the deposited energy. The  
 16 main goal of this 20 cm thick detector is to discriminate between photons and neutral pions.

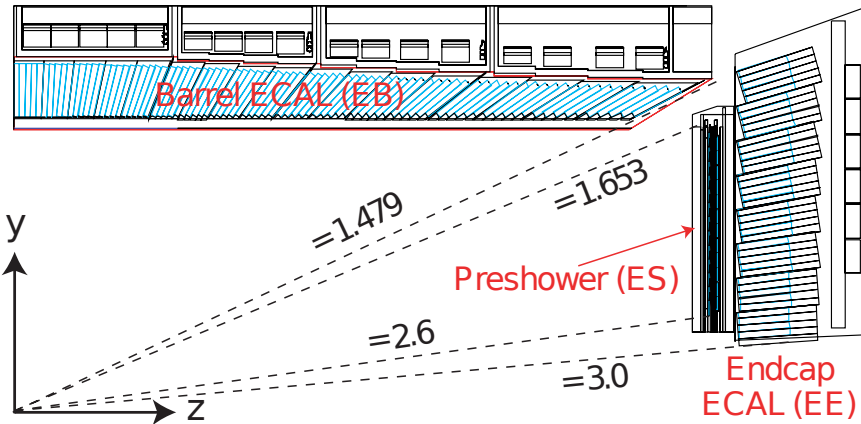


Figure 3.6: A transverse view parallel to the beamline showing one quarter of the ECAL, with its barrel (EB), endcap (EE), and preshower (ES) detectors. Figure taken from [99]

17 The energy resolution of calorimeters can be parametrized by the following stochastic ( $S$ ), noise ( $N$ ),  
 18 and constant ( $C$ ) terms:

$$\left(\frac{\sigma}{E}\right)^2 = \left(\frac{S}{\sqrt{E}}\right)^2 + \left(\frac{N}{E}\right)^2 + C^2 \quad (3.5)$$

19 The stochastic term represents contributions from the shower containment, the number of photoelectrons  
 20 and the fluctuations in the gain process. The noise term takes into account all noise components, such as  
 21 electronics and digitization noise. Finally, the constant term characterizes among others energy leakage  
 22 from the back of the calorimeter crystals and non-uniformities of the longitudinal light collection. The  
 23 latter term dominates the energy resolution for high-energy electron and photon showers. Figure 3.7  
 24 shows the energy dependence of this resolution for incident electrons as measured in a beam test, as well  
 25 as the determined stochastic, noise, and constant terms obtained by fitting equation 3.5 to the data.

26 A more recent measurement of the energy resolution was performed using electrons from Z boson  
 27 decays in collision data. In the central region, up to  $|\eta| < 0.8$ , it was measured to be better than 2%. Out-  
 28 side of this region, in the more forward direction, the energy resolution is 2-5% [100]. The reconstruction  
 29 of the electrons and photons will be discussed in Section 4.3.2.

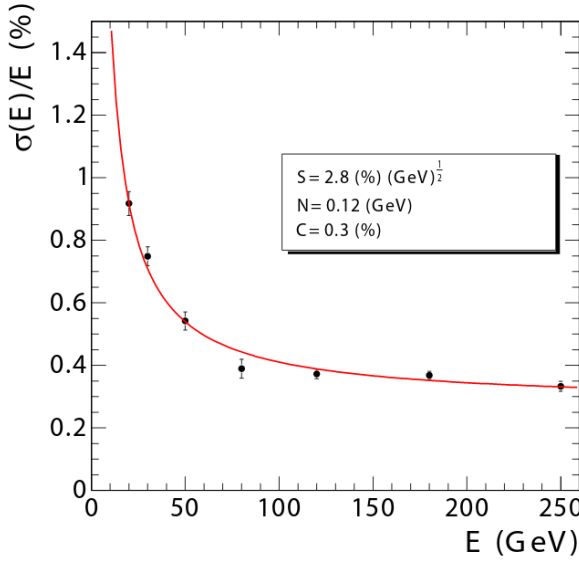


Figure 3.7: The ECAL energy resolution as a function of the electron energy, measured from a beam test. The stochastic ( $S$ ), noise ( $N$ ), and constant ( $C$ ) are given as well. Figure taken from [97].

### 3.2.3 The hadronic calorimeter

The hadronic calorimeter (HCAL) surrounds the ECAL with the aim to measure the energy of charged and neutral hadrons. The missing transverse energy can then be inferred from this measurement together with the measured energy in the ECAL, in order to identify neutrinos or exotic particles. The HCAL consists of brass absorber plates interleaved with plastic scintillator tiles.

Figure 3.8 shows a longitudinal quarter view of the different HCAL components. A cylindrical barrel (HB) covers the region up to  $|\eta| < 1.4$  and is complemented by endcaps (HE) on each side, extending the pseudorapidity range to  $|\eta| < 3.0$ . In the central region, the stopping power of the ECAL and HCAL barrel is not sufficient to contain the entire hadron showers. The HCAL was therefore extended outside the solenoid with an outer calorimeter (HO), which uses the magnet coil as absorber and consists of scintillators. Two layers are positioned at  $\eta = 0$ , where the absorber depth is minimal, and only 1 layer is used for the 2 rings on each side of the central ring. Finally, a forward calorimeter (HF) is positioned at 11.2 m from the IP covering  $3.0 < |\eta| < 5.2$ . Unlike the other HCAL components, this detector consists of iron and quartz fibres. Cherenkov-based, radiation-hard technology, since it is exposed to very large particle fluxes.

The optical signals from the scintillators in the HB and HE are converted to electrical signals by multichannel hybrid photodiodes, while silicon photomultipliers (SiPMs) are used in the HO. In the HF, the Cherenkov light emitted in the quartz fibres is detected by standard photomultiplier tubes (PMTs), since the magnetic field is much smaller in this region.

The expected transverse energy resolution for jets is shown in Figure 3.9 for various pseudorapidity regions: barrel jets ( $|\eta| < 1.4$ ), endcap jets ( $1.4 < |\eta| < 3.0$ ), and very forward jets ( $3.0 < |\eta| < 5.0$ ). Details about the reconstruction of jets from calorimeter and tracking information will be given in Section 4.3.6.

### 3.2.4 The muon system

The outermost detector, located entirely on the outside of the solenoid, is a dedicated muon detection system. The purpose of this subsystem is muon identification, momentum measurement, and triggering. As illustrated in Figure 3.10, the layers of muon chambers are embedded in the iron yoke constraining the magnetic field lines. The strong magnetic field completely saturates the return yoke with a field of about 2 T, in opposite direction with respect to the field inside the magnet.

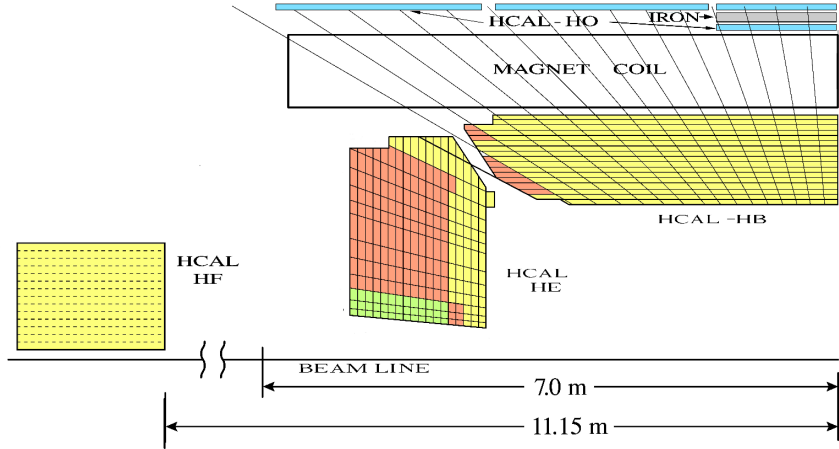


Figure 3.8: A quarter view of the hadronic calorimeter (HCAL), parallel to the beamline. The barrel (HB), endcap (HE), outer (HO), and forward (HF) detectors are indicated. Figure taken from [97].

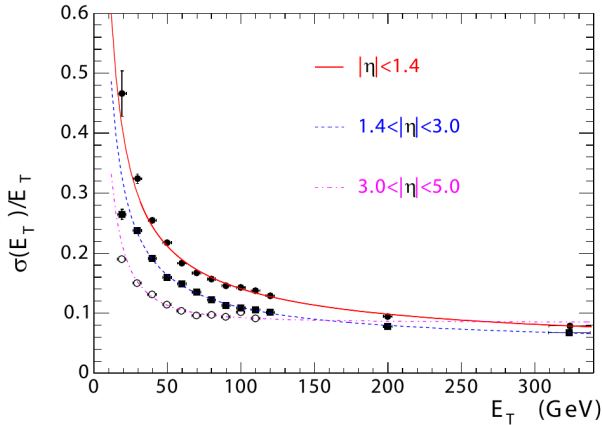


Figure 3.9: The jet transverse energy resolution as a function of the jet transverse energy, for barrel jets ( $|\eta| < 1.4$ ), endcap jets ( $1.4 < |\eta| < 3.0$ ), and very forward jets ( $3.0 < |\eta| < 5.0$ ). Figure taken from [97].

1 Three different types of gaseous detectors are used. In the barrel, 4 layers of Drift Tubes (DT) are  
2 installed, covering the pseudorapidity range up to  $|\eta| < 1.2$ . Due to the higher flux and the larger and non-  
3 uniform magnetic field at larger pseudorapidities, Cathode Strip Chambers (CSC) are used in the endcap  
4 region ( $0.9 < |\eta| < 2.4$ ). The DTs are designed for the low muon rates that are expected in the barrel  
5 and thus have a slower response time than the CSCs. Resistive Plate Chambers (RPCs) complement the  
6 DT and CSC systems in the pseudorapidity region up to  $|\eta| < 1.8$ . They provide a fast response, with a  
7 good time resolution but a worse spatial resolution than the DTs or CSCs. The RPCs are therefore very  
8 well suited to trigger on muons.

9 The offline reconstruction efficiency of simulated events containing one muon is typically between  
10 95% and 99%, except for the regions between 2 DT wheels ( $|\eta| = 0.25$  and  $|\eta| = 0.8$ ) and the transition  
11 region between the DTs and CSCs ( $|\eta| = 1.2$ ), where the efficiency drops to 92%. The reconstruction of  
12 muons using the information from the tracker and the muon detectors will be detailed in Section 4.3.4.  
13 For low pseudorapidities and small momenta, the offline momentum resolution of the standalone muon  
14 system is about 9%. At momenta around 1 TeV, the resolution varies from 15% to 40%, depending on  
15 the pseudorapidity. As demonstrated in Figure 3.11, performing a global momentum fit using the tracker  
16 as well improves the resolution by an order of magnitude at low muon momenta. At high momenta the  
17 resolution of the full system is about 5%.

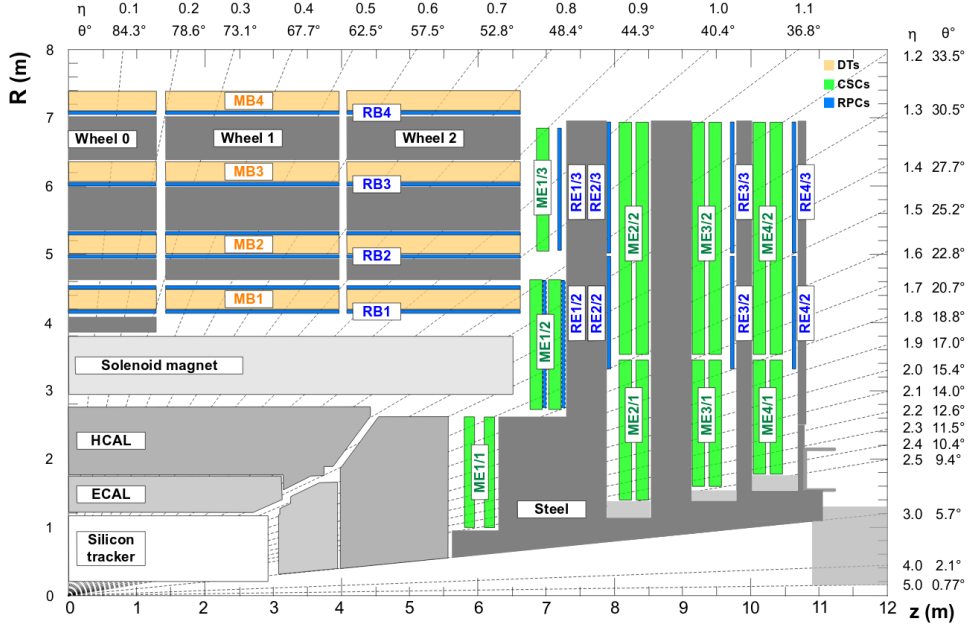


Figure 3.10: A transverse view of one quarter of CMS showing the position of the 3 types of muon detectors. The Drift Tubes (DT) are located in the barrel, the Cathode Strip Chambers (CSC) in the endcaps, and the Resistive Plate Chambers (RPC) in both regions up to  $|\eta| < 1.8$ . Figure taken from [101].

### 3.2.5 Trigger and data acquisition

Collisions are provided by the LHC at high interaction rates, with an interval of 25 ns between bunch crossings. This corresponds to a frequency of 40 MHz. Additionally, multiple collisions occur at the same time, depending on the luminosity. Since it is impossible to store and process the large amount of data produced in the collisions at this high rate, a severe rate reduction is needed. This rate reduction is performed by the trigger system, which decides whether to store or reject an event. Since this decision process is constrained in time, the computing time is optimized by rejecting uninteresting events as quickly as possible. The rate is reduced to 1 kHz in two steps by the Level-1 (L1) Trigger and the High-Level Trigger (HLT).

The L1 Trigger decision is based on information from the calorimeters and muon systems, following the structure illustrated in Figure 3.12. At the lowest level, the Local Triggers are based on energy deposits in calorimeter towers and track segments or hit patterns in the muon system. Regional triggers, indicated as Calo Trigger Layer 1 and Muon Track-Finder Layer in the figure, then combine this information and use pattern logic to determine trigger objects such as jet or muon candidates in separated spatial regions. The candidates are ranked based on their energy or momentum and quality, reflecting the level of confidence assigned to the L1 parameter measurements. Finally, the Calo Trigger Layer 2 and the Global Muon Trigger (GMT) determine the highest-rank calorimeter and muon objects across the whole detector and transfer them to the Global Trigger, which makes the final decision to accept or reject an event. Following this procedure, the L1 Trigger thresholds are tuned to reduce the event rate to 100 kHz. The L1 Trigger is composed of custom electronics located partially on the detectors, and partially in the underground service cavern. The L1 decision needs to be made and distributed to the detector front-end electronics within 3.8  $\mu$ s [102].

The readout of the data proceeds as illustrated in Figure 3.13. When an event is accepted by the L1 Trigger, the data from about 740 FEDs is read out by the Readout Units (RUs). For so-called *legacy* systems, i.e. systems which are using VME-based hardware from the initial installation, the FEDs are read out by custom Front-End-Readout-Link (FRL) cards, while for systems that changed their readout architecture from the VME standard to the newer  $\mu$ TCA standard during or after LS1 they are read out via the newer Front-End-Readout-Optical-Link (FEROL) cards. The event fragments are then sent over

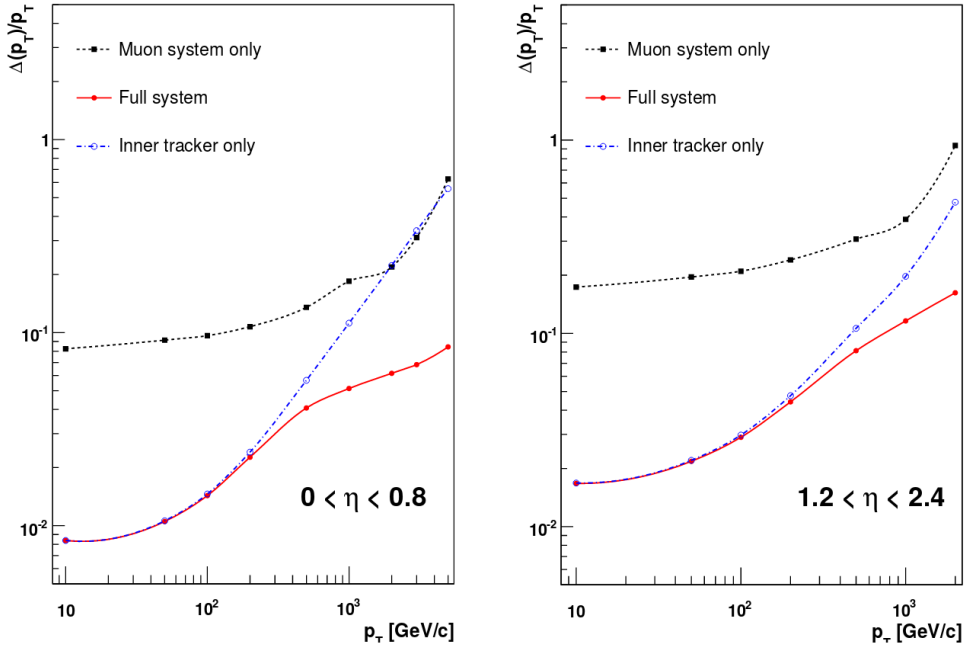


Figure 3.11: The muon transverse momentum resolution as a function of transverse momentum for low (left) and (high) pseudorapidities. The resolution is shown for the muon system and the tracker separately, and for the full system. Figure taken from [97].

1 the event-builder switch to the Builder Units (BUs), which assemble the events. Next, the events are  
2 distributed to the Filter Units (FUs) by a large switch network.

3 The HLT software system is implemented in this filter farm, which uses more than 15000 CPU cores  
4 for the final event selection. In this second step, the HLT reduces the event rate further to 1 kHz. The  
5 complete read-out data, including information from the pixel and strip tracker, are available for this step.  
6 New objects can therefore be reconstructed such as e.g. tau leptons and b-jets, as is done in the offline  
7 software, but speed-optimized.

### 8 3.2.6 CMS performance in Run 2

9 The number of collisions recorded at the experiments will differ from the amount delivered by the LHC.  
10 Data loss can be caused by e.g. problems with a particular subdetector, the trigger rate, the data acqui-  
11 sition, or the infrastructure. During Run 2, CMS achieved a data taking efficiency of 89% and 92% in  
12 2015 and 2016, respectively. The comparison between the delivered and recorded cumulative integrated  
13 luminosity in 2016 is shown in Figure 3.14. Subsequently, the recorded data is certified by the offline  
14 Data Quality Monitoring (DQM), to ensure that the data are suited for physics analysis.

#### 15 3.2.6.1 Pre-amplifier saturation in the APV25 chip

16 During Run 2, the instantaneous luminosity delivered by the LHC increased continuously, and even ex-  
17 ceeded the design luminosity of  $10^{34} \text{ cm}^{-2}\text{s}^{-1}$  in 2016. As the luminosity increased, a dynamic in-  
18 efficiency appeared in the strip tracker, which was most noticeable in the first layer of the TOB. The  
19 symptoms were a change in the signal-to-noise ratio and loss of hits. As can be seen from Figure 3.15,  
20 the most probable value (MPV) of the signal-to-noise ratio is shifted towards lower values and the low  
21 tail increased as well. The loss of hits is clearly visible in Figure 3.16, showing the change in number  
22 of hits per track for increasing instantaneous luminosities. The run periods indicated in the plot refer  
23 to a subset of the data taken over the course of the year. Run period boundaries are typically defined  
24 by changes in the LHC running conditions, changes to the detector configuration or calibration, or other  
25 parameters. The number of hits decreases for later run periods such as D and F, as the instantaneous

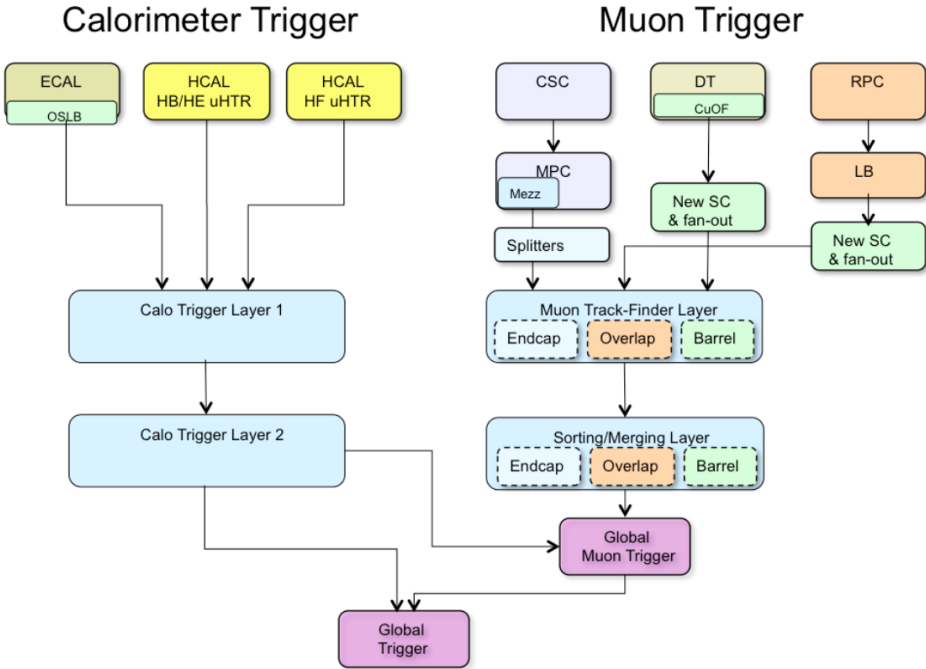


Figure 3.12: Schematic overview of the L1 Trigger. Figure taken from [102]

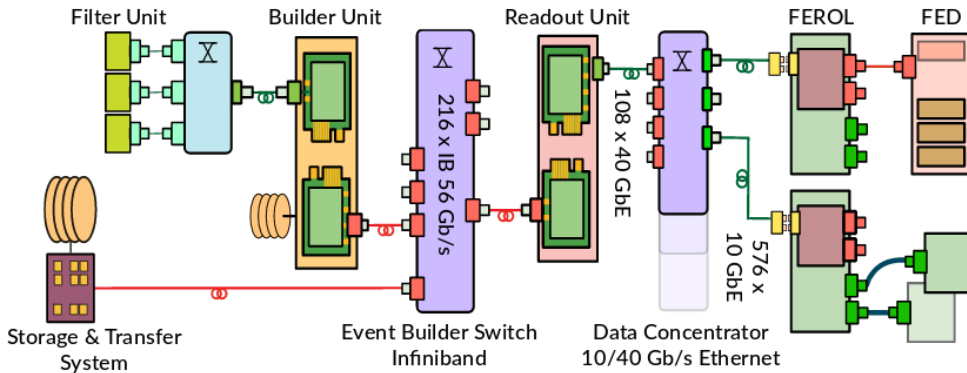


Figure 3.13: Schematic of the data acquisition (DAQ) system. Figure taken from [103]

<sup>1</sup> luminosity increases. This loss of hits results in less and shorter tracks.

<sup>2</sup> The origin of this inefficiency was eventually tracked down to saturation effects in the pre-amplifier of  
<sup>3</sup> the APV25 chip. The pre-amplifier decay time changes significantly with temperature. As the operating  
<sup>4</sup> temperature of the strip tracker was lowered from +4°C to -15°C coolant temperature during LS1, the  
<sup>5</sup> decay time was no longer sufficient to cope with the high luminosities. The dynamic inefficiency was  
<sup>6</sup> cured in August 2016 by changing the pre-amplifier drain speed. This lead among others to the recovery  
<sup>7</sup> of the muon efficiency, which showed a large drop for the highest luminosities before the change and an  
<sup>8</sup> essentially flat behaviour afterwards, as demonstrated in Figure 3.17.

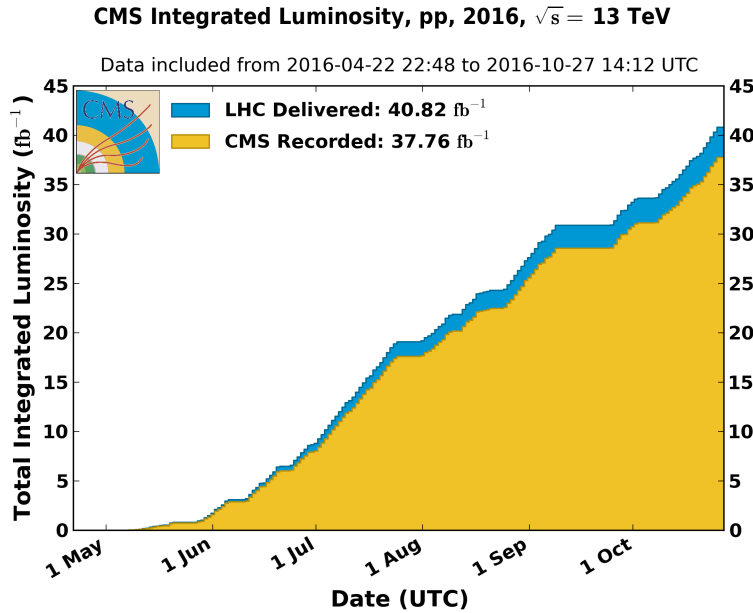


Figure 3.14: The cumulative distribution of the instantaneous luminosity delivered by the LHC (blue) and recorded by CMS (yellow) in 2016.

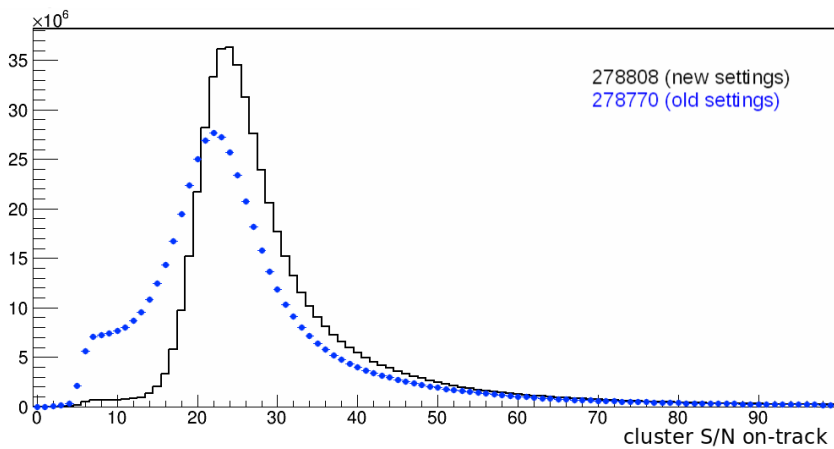


Figure 3.15: The signal-to-noise ratio for clusters on reconstructed tracks in the first layer of the TOB for a run before (blue) and after (black) the change of pre-amplifier drain speed.

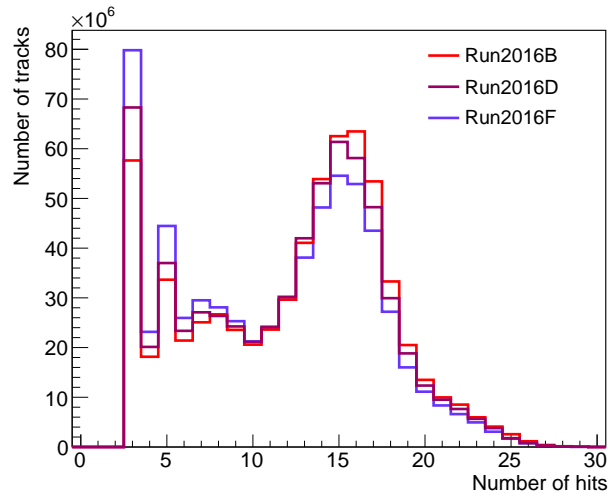


Figure 3.16: The number of hits per track for run periods B, D, and F, showing the effect of the increasing instantaneous luminosity.

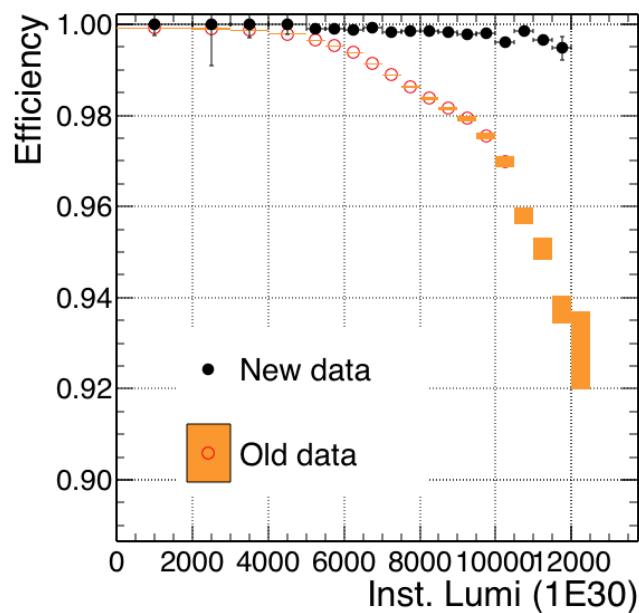


Figure 3.17: The muon efficiency as a function of the instantaneous luminosity for before (orange) and after (black) the change of pre-amplifier drain speed which cured the dynamic inefficiency.

# 4

1  
2

## Event Simulation and Reconstruction

3 In order to use the recorded data, the obtained signals coming from various parts of the detector must be  
4 reconstructed to be able to identify the particles in the event. Additionally, to compare the experimental  
5 results with theory, events are generated and the resulting signals in the detector are simulated, as detailed  
6 in Sections 4.1 and 4.2, respectively. The event reconstruction is detailed in Section 4.3. Finally, some  
7 details about the simulation of SIMPs are given in Section 4.4.

### 4.1 Event generation

8 The event structure at the LHC is complicated by the composite nature of protons, as well as the attainable  
9 high momentum transfers. A number of aspects must therefore be taken into account when generating  
10 events, such as parton distribution functions (PDFs), hard scattering, the parton shower, hadronization,  
11 and additional activity in the event.

12 Two partons, meaning the quark or gluon constituents of the colliding protons, will interact with a cer-  
13 tain probability at a given momentum transfer. This is parametrized by the PDFs  $f(x, Q^2)$ , were  $x$  is the  
14 proton's momentum fraction and  $Q^2$  is the momentum transfer scale. Experimentally determined PDFs  
15 are available from various groups, including e.g. CTEQ [104], MRST/MSTW [105], and NNPDF [106].  
16 An example of such PDFs obtained by the NNPDF group is shown in Figure 4.1. The PDFs are then  
17 convoluted with the matrix element of the hard scattering, which is the process of interest where the two  
18 colliding partons create high-energetic final state particles. This is done using an event generator, such  
19 as MADGRAPH5\_aMC@NLO [107] and PowHEG [108]. With MADGRAPH5\_aMC@NLO the ma-  
20 trix element can be calculated at tree-level or leading order (LO), and since the addition of aMC@NLO  
21 at next-to-leading order (NLO) as well. This generator was used to generate most of the background  
22 processes for the Monojet analysis detailed in Chapter 5 and for the SIMP signal used in Chapter 6.  
23 PowHEG is able to generate events using NLO computations, but only for a relatively limited number of  
24 physics processes. In this thesis, background processes from single-top production were generated with  
25 this program. Since NLO calculations are more time-consuming, one can instead use the less precise  
26 method of scaling a LO cross section to the NLO level by using a so-called k-factor, defined as the ratio  
27 of the NLO and LO cross sections. However, these k-factors often need to be determined as a function  
28 of the relevant kinematic variables as they depend on the kinematic phase space and the probed energy  
29 scale.

30 Since the colliding partons have a color charge, the hard scattering will be accompanied by a cas-  
31 cade of radiation from QCD processes. This radiation can originate from the incoming partons, which  
32 is referred to as initial state radiation (ISR), or the outgoing partons in the final state, the so-called fi-  
33 nal state radiation (FSR). The perturbative evolution of the cascade can be modelled using the DGLAP

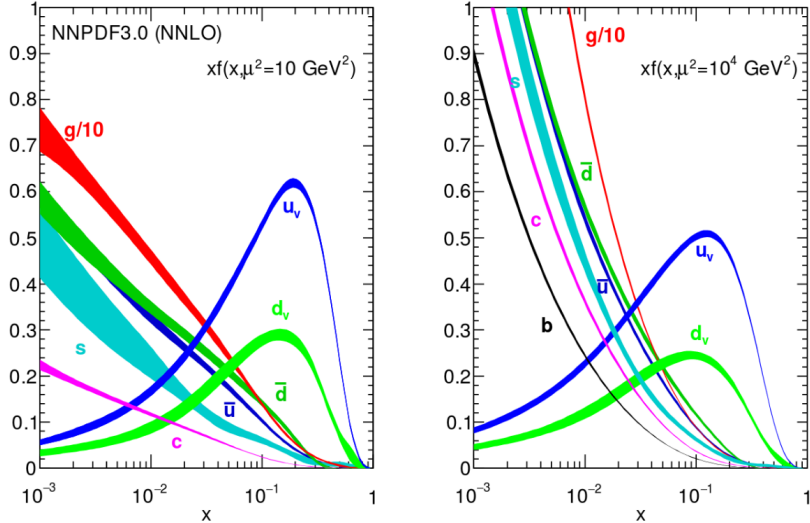


Figure 4.1: The parton distribution functions times the momentum fraction  $x$  at energy scales  $10 \text{ GeV}^2$  (left) and  $10\,000 \text{ GeV}^2$  (right), obtained in NNLO NNPDF3.0 global analysis. Figures taken from [106].

(Dokshitzer-Gribov-Lipatov-Altarelli-Parisi) equations [109–111]. These equations describe the time evolution of the probability of a ‘mother’ parton to split into ‘daughter’ partons at an energy scale  $Q^2$ . The momentum of the mother is then divided among the daughter partons, which can in turn split into other partons at a lower  $Q^2$  scale. The cascade continues down to an energy scale  $\Lambda_{QCD}$  where the strong coupling constant becomes unity.

The next step after the showering is the hadronization of the coloured particles produced in the parton shower, transforming them into color-neutral hadrons. Since this happens at low energy scales where the perturbative approach of QCD is not valid, phenomenological models have to be used. For most of the processes considered in this thesis, the showering and hadronization is done with PYTHIA 8 [112], using a standard set of parameters which were tuned to reproduce the experimental data.

In addition to ISR and FSR, also beam remnants and multiple parton interactions give rise to additional activity in the event, referred to as the underlying event. After the partons participating in the hard scattering are extracted, the remainder of the protons have a non-zero colour charge. The creation of additional hadrons during the hadronization is therefore possible. Multiple parton interactions represent additional interactions which can take place between other incoming partons. Finally, additional collisions between other protons in the same bunch crossing or from a previous bunch crossing, respectively referred to as in-time and out-of-time pileup, add extra activity in the event.

## 4.2 Detector simulation

After being generated, the collision events are passed on to the CMS detector simulation, which is based on the GEANT 4 [113] simulation toolkit. This toolkit provides a description of the interaction between particles and the detector material, including effects such as bremsstrahlung of charged particles, photon conversions, energy loss of charged particles by ionization, and the showering of electrons, photons and hadrons in the calorimeters due to interaction with the material. The CMS simulation package contains the geometry of the detector with all the sensitive layers designed to detect the traversing particles, as well as the dead material regions consisting of e.g. support structures, cables and cooling pipes. A precise map of the magnetic field is also included in order to simulate the curvature of the charged particles correctly.

Next, the impact of the detector, coming from the electronic response produced by the hits in the active detector material, the digitization, the data transmission, and any reconstruction performed in the electronics such as zero-suppression or cluster reconstruction, is simulated. In this way, an event content similar to the output of the real detector is obtained. At this point the effect of pileup is also included by adding detector hits of generated proton-proton interactions on top of the hits resulting from the main

interaction. Most of the simulated event samples used in this thesis are processed using this detector simulation. However, the interaction of new particles that can arise from specific theory models is not always readily described in GEANT. This is the case for the signal samples used in the analysis described in Chapter 6, so an additional step was needed in order to simulate strongly interacting massive particles (SIMPs) in the CMS detector, described in Section 4.4.

## 4.3 Event reconstruction

Once the detector response has been simulated, the obtained events can be reconstructed. The same method is applied for these simulated events and for data coming from the detector. First, the reconstruction of tracks is performed, with a specific track reconstruction for electrons and muons. Furthermore, the calorimeter deposits, generated by electrons, photons, and hadrons, are grouped into clusters. Additionally, the reconstruction is further improved by using the so-called particle flow (PF) algorithm. This algorithm greatly improves the performance for jet and hadronic  $\tau$  decay reconstruction, missing transverse energy momentum determination, as well as electron and muon identification. Finally, the obtained particle flow (PF) candidates are clustered into jets, and the missing transverse energy can be derived.

### 4.3.1 Track and vertex reconstruction

The tracks of charged particles going through the CMS tracker are reconstructed with an iterative tracking approach. This is used to cope with the high occupancy and consequently high combinatorics. Additionally, the first iterations search for tracks with less possible combinations, such as tracks with many pixel hits or a high momentum. After every iteration, the hits associated with the found track are removed to reduce the combinatorics. Each iteration consists of four steps:

1. **Seed generation.** In this first step hits are combined into seeds for the subsequent track finding. In the initial iterations pixel triplets are used, then pixel pairs, in order to take gaps or non-working modules into account. Next, mixed pixel/strip triplets are taken, and finally strip-only seeds are used. These additional iterations improve the acceptance in  $p_T$  and in displacement with respect to the primary vertex.
2. **Track finding.** The seeds are used as starting point for a Kalman filter algorithm. This method extrapolates the seed trajectory outward to the next layer, taking into account potential energy loss and multiple scattering. If compatible hits are found in the next layer, the parameters of the trajectory are updated. This process continues until the outermost layer of the tracking system. Using this method, a given seed can generate multiple tracks, or different tracks can share hits. A trajectory cleaner therefore determines the fraction of hits the tracks have in common and discards the track with the lowest number of hits when there are too many shared hits. If both tracks have the same number of hits, the track with the largest  $\chi^2$  value is removed.
3. **Track fitting.** The track parameters are then refitted using a Kalman filter and smoother, taking all hits determined in the track finding step into account.
4. **Track selection.** Finally, the tracks are selected based on quality requirements, such as the number of layers that have hits, the  $\chi^2/\text{dof}$ , and the distance to a primary vertex. This greatly reduces the fraction of reconstructed tracks that are fake.

The performance of the track reconstruction is excellent, and a high track-finding efficiency is obtained [114] while keeping the rate of fake tracks negligible. The highest tracking efficiency is obtained for muons, which traverse the full detector volume and have an improved momentum resolution due to tracking information from the muon detectors giving a long lever arm. For isolated muons with  $p_T$  between 1 and 100 GeV the tracking efficiency is higher than 99% for the entire  $\eta$  coverage of the tracker, as can be seen from the left plot in Figure 4.2. The  $p_T$  resolution is about 2-3% for a muon with  $p_T = 100$  GeV up to  $|\eta| < 1.6$ , but worsens for higher pseudorapidities. Different types of particles interact

1 differently with the detector material. Charged hadrons, for example, are also subject to elastic and in-  
 2 elastic nuclear interactions and have a tracking efficiency of 80-95% depending on pseudorapidity and  
 3 transverse momentum, as shown in the right plot of Figure 4.2.

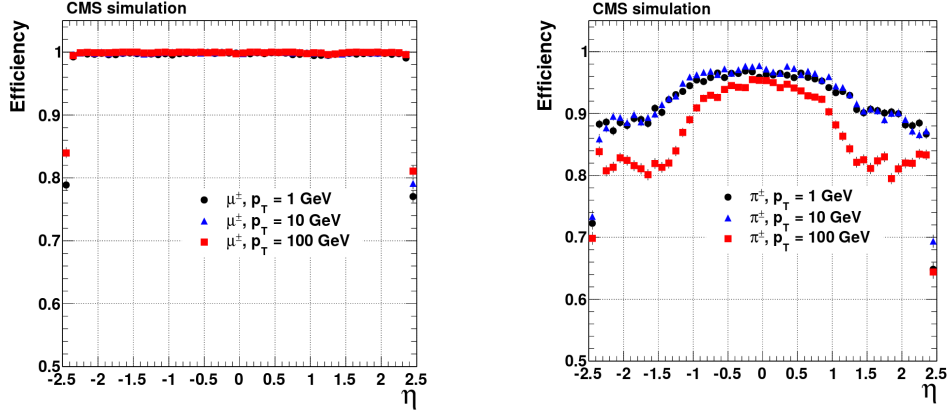


*Figure 4.2: The muon efficiency (left) and pion efficiency (right) as a function of pseudorapidity, for multiple transverse momenta. Figures taken from [114]*

4 Finally, the primary vertex is reconstructed from the tracks. Since the collisions happen between  
 5 bunches of protons, multiple protons will be colliding at the same time. The extra collisions, next to the  
 6 potentially interesting collision, are referred to as pile-up interactions. The particles generated in these  
 7 collisions are all detected simultaneously and form a challenge to disentangle them from the particles  
 8 coming from the to be studied interaction.

9 The reconstruction is done in 2 steps: first the tracks that appear to originate from the same interaction  
 10 vertex are clustered, then a fitting procedure computes the vertex parameters and assigns a weight to each  
 11 associated track, reflecting the probability that it corresponds to the considered vertex. Figure 4.3 shows  
 12 the reconstruction efficiency and the resolution of the primary vertex. The more tracks, the better the  
 13 vertex is constrained and thus the better the resolution.

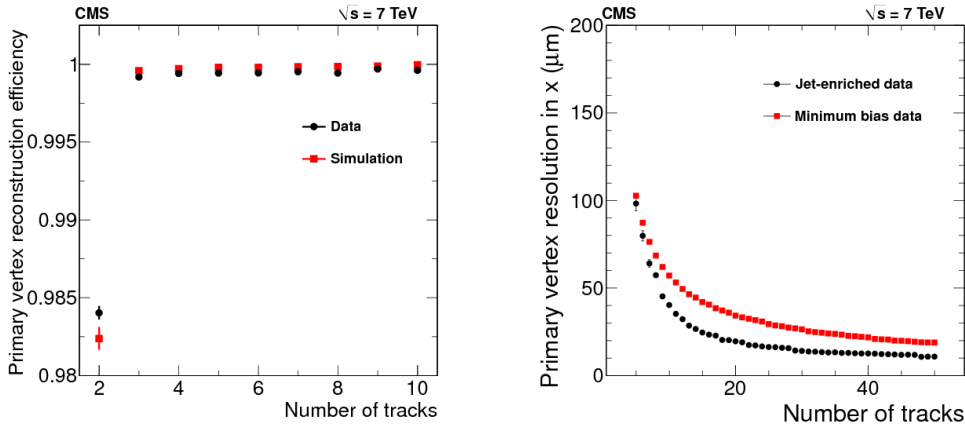


*Figure 4.3: The primary vertex reconstruction efficiency (left) and resolution (right) as a function of the number of tracks associated to it. Figures taken from [114]*

### 14 4.3.2 Electron and isolated photon reconstruction

15 Electrons are reconstructed using information from both the tracker and the calorimeters. Due to the large  
 16 amount of material present in the tracker, electrons will emit bremsstrahlung photons, and photons will  
 17 often convert into  $e^+e^-$  pairs, which can again radiate bremsstrahlung photons.

For electrons, a Gaussian-sum filter (GSF) [115] candidate is taken as starting point. This GSF candidate is obtained using 2 different methods to reconstruct the electron track from the hits in the tracker, which should gather all radiated energy from the electron. First, the ECAL-based approach is used, grouping ECAL clusters into superclusters. These superclusters collect the energy of the electron and the bremsstrahlung photons in a small  $\eta$  window and a large  $\phi$  window, taking the bending of the electron track in the magnetic field into account. The supercluster energy and position is then used to estimate the position of the corresponding hits in the tracker layers. Subsequently, the tracker-based approach is used to find electrons missed by the ECAL-based method. In this case, the tracks from the iterative tracking with transverse momentum larger than 2 GeV are used. Additional requirements are placed on the number of hits and the  $\chi^2$  of the fit, and the specific electron tracking is performed, using a GSF fit, which is more adapted to electrons than the Kalman filter used in the iterative tracking, as it describes the energy loss in each tracker layer. The electron seeds obtained with both methods are merged and used as input for the full electron tracking. The obtained electron tracks are then linked to ECAL clusters by the PF algorithm, as described in Section 4.3.5. In the case of isolated photons, a candidate is seeded from an ECAL supercluster with transverse energy larger than 10 GeV which is not linked to a GSF track.

The total energy of the accumulated ECAL clusters is corrected for the energy that was lost in the process of reconstruction, using analytical functions of the energy and pseudorapidity. The applied corrections can be as large as 25%, at low transverse momentum and at  $|\eta| = 1.5$ , where the material density in the tracker is largest. The energy of the electron is then obtained from a combination of the corrected energy and the momentum of the GSF track, while the direction of the electron is taken from the GSF track. For photons, the corrected energy and the direction of the supercluster are used.

Additionally, the electron and photon candidates must satisfy identification criteria to be retained. In the case of electrons a boosted decision tree is used, combining fourteen variables including the amount of energy radiated and the ratio between the energies gathered in HCAL and ECAL, while for photons the candidates must be isolated from other tracks and calorimeter clusters, and the energy distribution in the ECAL and the ratio between the HCAL and ECAL energies must be compatible with the expectation from a photon shower.

### 4.3.3 Electron and photon identification

### 4.3.4 Muon reconstruction

Muon tracking is performed using 2 complementary approaches. The first method starts from standalone muons, which are reconstructed from hits in the muon detectors only using pattern recognition. The standalone muons are then matched to tracks in the tracker, and the hits are combined to form a global muon track. This global muon fit improves the momentum resolution compared to the tracker-only fit at muon momenta larger than 200 GeV.

For momenta below 10 GeV, muons often fail the global muon conditions which require the muon to penetrate through more than one muon detector plane, due to the large multiple scattering in the return yoke. In this case, tracker-only muon reconstruction is more efficient since it only requires one muon segment. Each track in the tracker with a transverse momentum larger than 0.5 GeV and a total momentum larger than 2.5 GeV is therefore extrapolated to the muon system and if at least one matching track segment is found, it is retained as muon candidate.

Within the geometrical acceptance of the muon system about 99% of the muons are reconstructed, either as global muon or as tracker muon and frequently as both. Global and tracker muons that share the same track inside the tracker are merged into a single candidate. Muons that are only reconstructed as standalone muons have a worse momentum resolution compared to the global and tracker muons. These standalone muons are however only considered in the further reconstruction when the fit is of high quality and is associated with a large number of hits in the muon system.

Charged hadrons can be misreconstructed as muons if e.g. a part of the hadron shower reaches the muon system. In order to improve the muon identification, the PF muon identification algorithm described in Section 4.3.5 also matches energy deposits in the ECAL and HCAL with the muon track.

### 1 4.3.5 Particle flow

2 The particle flow (PF) algorithm [116] reconstructs so-called particle flow candidates by combining information from all different CMS subdetectors, linking different elements, such as tracks in the tracker, 3 calorimeter clusters, and muon tracks. A global picture of the event is thus formed, where each particle 4 is uniquely identified. The obtained collection of particle candidates is subsequently used to reconstruct jets and tau leptons, and to determine the missing transverse energy.

5 In a first step, the PF algorithm identifies charged particle tracks, as defined in Section 4.3.1 for all 6 tracks, and in Sections 4.3.2 and 4.3.4 for electron and muon tracks in particular. At the same time, the 7 calorimeter clusters are reconstructed with a clustering algorithm designed specifically for the PF event 8 reconstruction. In this algorithm, cluster seeds are first identified as local energy maxima with respect 9 to the four or eight closest cells, if the energy deposited in the cell is above a given seed threshold. The 10 clusters are then formed by accumulating neighbouring cells with an energy above a given cell threshold, 11 suppressing noise.

12 The PF elements in the different subdetectors are then connected by a link algorithm which avoids any 13 double counting. The link algorithm produces blocks of associated elements, quantifying the quality of 14 the link by defining a geometrical distance between the elements. When an element is linked to multiple 15 other elements, only the link with the shortest distance is kept. More precisely, a link between a track 16 in the tracker and a calorimeter cluster is made by extrapolating it from the last hit in the tracker to 17 the calorimeters. The distance between the position of the extrapolated track and the cluster in the  $(\eta,$  18  $\phi)$  plane is then used to define the link distance. At the interaction points between the track and the 19 tracker layers, tangents to the GSF tracks are extrapolated to the ECAL in order to collect the energy 20 of photons radiated by electron bremsstrahlung. A dedicated conversion finder was also developed to 21 identify bremsstrahlung and prompt photon conversions into  $e^+e^-$  pairs. Links between calorimeter 22 clusters are established outside of the tracker acceptance, or between the preshower and ECAL clusters in 23 the preshower acceptance. In this case the link distance is also defined as the distance between the position 24 of the clusters. Charged particle tracks can also be linked by a common secondary vertex. Finally, the PF 25 muon identification algorithm associates the muon tracks to the muon energy deposits in the ECAL and 26 HCAL, to improve the muon identification performance.

27 In a next step, the PF blocks obtained by linking the multiple PF elements, are classified as muons, 28 electrons, or isolated photons. The corresponding elements are then excluded from further consideration. 29 Once electrons, muons, and isolated photons have been identified, the remaining elements are identified 30 as charged hadrons, neutral hadrons, or photons produced in jets. Within the tracker acceptance, the 31 ECAL clusters not linked to any track are classified as photons, while the clusters in the HCAL without 32 a matched track are labelled as neutral hadrons. Outside of the tracker acceptance, charged and neutral 33 hadrons can not be distinguished. ECAL clusters linked to an HCAL cluster are then assumed to arise 34 from the same hadron shower, and the estimated energy for these particles is the sum of the energy 35 deposited in the ECAL and the HCAL. The ECAL clusters that are not linked to an HCAL cluster are 36 classified as photons.

### 39 4.3.6 Jet reconstruction

40 Jets are reconstructed with the anti- $k_T$  algorithm [117], which clusters either the generated particles from 41 event simulation, or the particles reconstructed by the PF algorithm (PF jets), or the energy deposits in 42 the calorimeters (Calo jets). This procedure takes into account the transverse momentum  $p_T$ , also called 43  $k_T$ , of the particles and the distance between particles, defined as

$$\Delta R_{ij} = \sqrt{(\eta_i - \eta_j)^2 + (\phi_i - \phi_j)^2}. \quad (4.1)$$

44 The strategy consists of the following steps:

45 1. For every pair of particles  $i$  and  $j$ , a distance  $d_{ij}$  defined as

$$d_{ij} = \min \left( \frac{1}{p_{Ti}^2}, \frac{1}{p_{Tj}^2} \right) \frac{\Delta R_{ij}^2}{R^2} \quad (4.2)$$

1       is calculated.

2       2. For every particle  $i$ , a distance  $d_{iB}$  to the beam pipe is calculated with

$$d_{iB} = 1/p_{Ti}^2. \quad (4.3)$$

3       3. The minimum of  $d_{ij}$  and  $d_{iB}$  is then determined.

4       4. If it is  $d_{ij}$ , particles  $i$  and  $j$  are recombined into a new particle by adding the four-momenta of the  
5       particles. If it is  $d_{iB}$ , particle  $i$  is declared to be a jet and it is removed from the list of particles.

6       5. This is repeated until no particles remain.

7       In this clustering algorithm, the parameter  $R$  determines what is called a jet. If a particle  $i$  has  
8       no other particles within a distance  $R$ ,  $d_{iB}$  will be smaller than  $d_{ij}$  and the particle will become a jet.  
9       A consequence of this is that an arbitrarily soft particle can become a jet, and therefore a minimum  
10      transverse momentum for a jet to be of interest is defined.

11      The anti- $k_T$  algorithm favours clustering around hard particles, and the jets then grow outward from  
12      this seed. This gives rise to circular jets, with a cone size that is proportional to  $R$ . Since it still involves  
13      a combination of energy and angle in the distance measure, this is a collinear-safe growth, meaning that  
14      the jet will not change when one of the particles of the jet is split collinearly. This algorithm is also  
15      infrared-safe, i.e. the same set of jets is obtained when soft particles are emitted.

16      A reliable determination of the jet energy is not straightforward, since many effects can distort the  
17      energy estimation, such as the calorimeter response, the limited particle reconstruction efficiency, the un-  
18      derlying event, the pileup, and the charged particles bending out of the jet cone due to the strong magnetic  
19      field. The pileup is mitigated by applying charged hadron subtraction (CHS), which consists of removing  
20      charged hadrons associated with vertices other than the primary vertex from the list of PF candidates.  
21      Additionally, the jet energy is corrected using a factorized approach, as illustrated in Figure 4.4, with the  
22      following steps:

23      • **Pileup correction (L1).** The first level of jet energy corrections is applied event-by-event and jet-  
24      by-jet, and is determined from simulation. It is dependent on the pseudorapidity and transverse  
25      momentum of the jet, the average  $p_T$  density in the event, and the effective jet area. This effective  
26      area is determined by injecting a large number of very soft particles in the event before the jet clus-  
27      tering. The spread of the soft particles in each jet then defines the jet area. When these corrections  
28      are applied on data, residual corrections are also applied to take into account the difference between  
29      the simulated events and the data.

30      • **Relative  $\eta$  and absolute  $p_T$  corrections (L2L3).** These corrections are also obtained from simula-  
31      tions and correct for the non-uniform response of the calorimeters in  $\eta$  and  $p_T$ . They are determined  
32      by comparing the reconstructed  $p_T$  to the one obtained from the jets built from the generated par-  
33      ticles. These corrections have the largest impact on the jet energy.

34      • **Residual  $\eta$  and  $p_T$  corrections (L2L3Residual).** Since the L2L3 correction is derived from simu-  
35      lation, additional residual corrections are needed in order to correct for the remaining small differ-  
36      ences between the jet response in data and simulation. These corrections are typically of the order  
37      of a few percent.

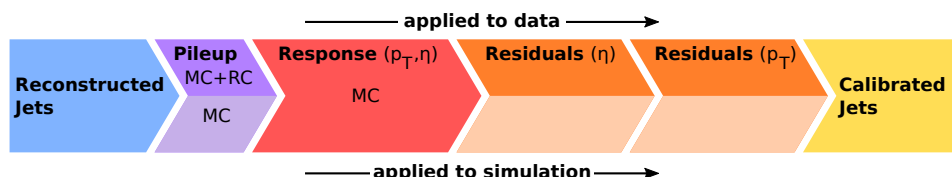


Figure 4.4: Graphical overview of the factorized approach used at CMS to apply jet energy corrections.

1     Optionally, a set of identification criteria are applied on the PF jets. A jet is required to consist of  
 2     at least two particles. For jets in the region  $|\eta| < 2.7$ , the fraction of energy coming from ether neutral  
 3     hadrons or photons should not exceed 99%. Additionally, for jets restricted to the tracker acceptance  
 4     ( $|\eta| < 2.4$ ), there should at least be some energy deposited in the HCAL, the jet should contain 1 or more  
 5     charged constituent, and the fraction of energy corresponding to electrons or photons should not exceed  
 6     99%.

### 7     **4.3.7 Identification of b-jets**

8     For the identification of jets originating from  $b$  quarks, the long lifetime of the  $b$  hadrons arising from the  
 9     hadronization of  $b$  quarks is exploited. The  $b$  hadrons will therefore decay at a position that is displaced  
 10    with respect to the primary interaction vertex. The b-jets can then be identified by looking for the presence  
 11    of displaced tracks from which a secondary vertex may be reconstructed. Additionally, the  $b$  hadrons  
 12    have a probability of 20% to decay into muons or electrons. Consequently, the presence of these charged  
 13    leptons can be used as well for b-jet identification techniques.

14    Within the CMS collaboration, two different algorithms are being used during Run 2, namely the  
 15    Jet Probability and the Combined Secondary Vertex taggers [118]. In this thesis, the latter is used to  
 16    identify b-jets, combining the information from displaced tracks and secondary vertices in a multivariate  
 17    technique. Jets are then identified or “tagged” as b-jets by applying a cut on the discriminator output.  
 18    Three standard operating points are defined, denoted as “loose”, “medium”, and “tight”, corresponding  
 19    to a misidentification probability of 10%, 1%, and 0.1% for light jets with  $p_T > 30$  GeV, respectively.

### 20    **4.3.8 Reconstruction of tau leptons**

21    Tau leptons can decay into either a charged lepton and two neutrinos, or a few hadrons and one neutrino.  
 22    The hadronic decays of the tau lepton can be separated from quark or gluon jets by analysing the  
 23    decay products. With the PF algorithm, it is possible to resolve the particles originating from the tau  
 24    decay and to determine its isolation. Hadronic tau decays are reconstructed using the hadrons-plus-strips  
 25    (HPS) algorithm [119] by using those particles as input. The jet constituent particles are combined into  
 26    candidates compatible with one of the main hadronic tau decay modes,  $\tau^- \rightarrow h^- \nu_\tau$ ,  $\tau^- \rightarrow h^- \pi^0 \nu_\tau$ ,  
 27     $\tau^- \rightarrow h^- \pi^0 \pi^0 \nu_\tau$ , and  $\tau^- \rightarrow h^- h^+ h^- \nu_\tau$ . This PF reconstruction of the tau decay products has signifi-  
 28    cantly improved the reconstruction and identification of the tau leptons compared to the previous method  
 29    which only took the energy deposits in the calorimeters into account.

### 30    **4.3.9 Missing transverse momentum reconstruction**

31    While most particles produced in the collisions can be reconstructed from the hits and energy deposits  
 32    in the detector, some collision products might not leave energy deposits in tracker, calorimeters or muon  
 33    system. This makes an accurate reconstruction of this type of particles impossible, and an alternative  
 34    method is used, based on indirect observations. As the detector is hermetically closed such that all  
 35    other particles in the event can be detected, the missing transverse momentum can be determined. This  
 36    momentum then corresponds to all undetected particles in the event, and can be calculated from the  
 37    vectorial sum of the transverse momenta of all the observed final state particles:

$$\vec{E}_T^{miss} = - \sum \vec{p}_T, \quad (4.4)$$

38    where the sum runs over all reconstructed PF particles. The variable that is generally used in particle  
 39    physics analyses is the norm of the missing transverse momentum:

$$E_T^{miss} = |\vec{E}_T^{miss}|. \quad (4.5)$$

40    A notable example of particles leaving no hits or energy deposits behind are neutrinos, as they are  
 41    neutral and weakly interacting and will therefore traverse the entire detector unhindered. Other hypothet-  
 42    ical neutral weakly interacting particles, which are being searched for in many physics analyses, would  
 43    escape the detector without producing hits as well.

## 4.4 Simulation of the SIMP signal

For the generation of the SIMP signal, the model Lagrangian given in equation ?? is implemented in FEYNRULES 2.0 [120]. Next, the matrix element is calculated at LO and events are generated using MADGRAPH 5. The subsequent parton shower and hadronization is done with PYTHIA 8, using tune CUEP8M1. Next, the events are simulated in the CMS detector using GEANT. However, the SIMPs are not included in the simulation, as their interaction with matter is not implemented in GEANT. The SIMPs were instead incorporated by adding an additional step to the standard reconstruction described in Section 4.3. In this additional step the SIMPs are directly converted to neutral PF candidates and merged with the rest of the PF candidates. The standard pileup corrections, jet clustering, and charged hadron subtraction are then applied in order to obtain the resulting jets, denoted here as P2PF jets.

In order to validate this method, a second sample was produced using neutrons instead of SIMPs, because of their resemblance to the SIMPs as single neutral particles generating a hadronic shower. The same additional step is applied, but in this case the neutrons will also be correctly reconstructed by the standard reconstruction. The reconstructed PF candidates that are matched to the generated neutrons were therefore removed before injecting the converted generated neutrons to the collection of PF candidates. This sample is then used to evaluate the difference with a standard neutron sample where the full GEANT simulation is done.

The two leading generator-level jets (GEN) can then be compared to the uncorrected P2PF jets from the custom sample and the PF jets from the standard sample. The transverse momentum of these jets is compared in Figure 4.5. This shows that the jet energy resolution (JER) is not described properly, since the additional step directly converts generated particles to PF candidates without taking into account any other effects. In order to produce a more realistic simulation, the new PF candidates are therefore smeared with JER distributions derived using the uncorrected PF jets matching the neutrons in the standard neutron sample in bins of  $\eta$  and  $p_T$ . An example of this resolution is shown in Figure 4.6 for central neutrons with low and high transverse momentum.

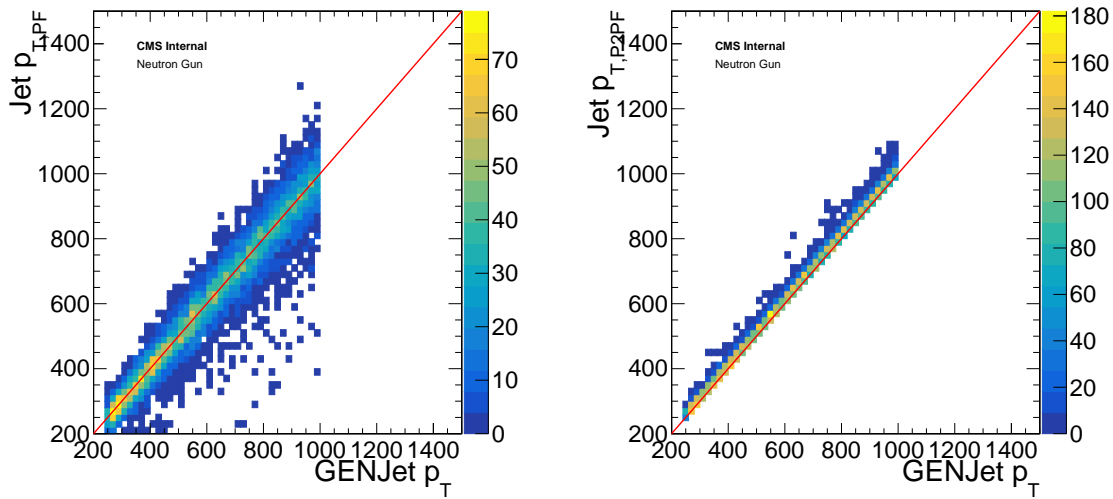


Figure 4.5: Comparison of the transverse momentum of the generator-level jets to the PF jets (left) and P2PF jets (right) without jet energy resolution smearing, using a neutron sample.

After applying this smearing, the P2PF jets are processed with the standard sequence of charged hadron subtraction, jet clustering, L1FastJet, and L2/L3 corrections. The comparison of the corrected P2PF jets and the standard corrected PF jets is shown in Figure 4.7 for the neutron sample, validating that the jet transverse momentum is now correctly smeared. The JER distributions are also compared in Figure 4.8 and fitted with a Crystal Ball function, showing compatible parameters. This demonstrates that the procedure, where the JER distributions derived from a neutron sample are used to smear the PF candidates from generator-level SIMPs, can sufficiently accurately simulate SIMPs in a realistic detector, assuming SIMPs are neutron-like.

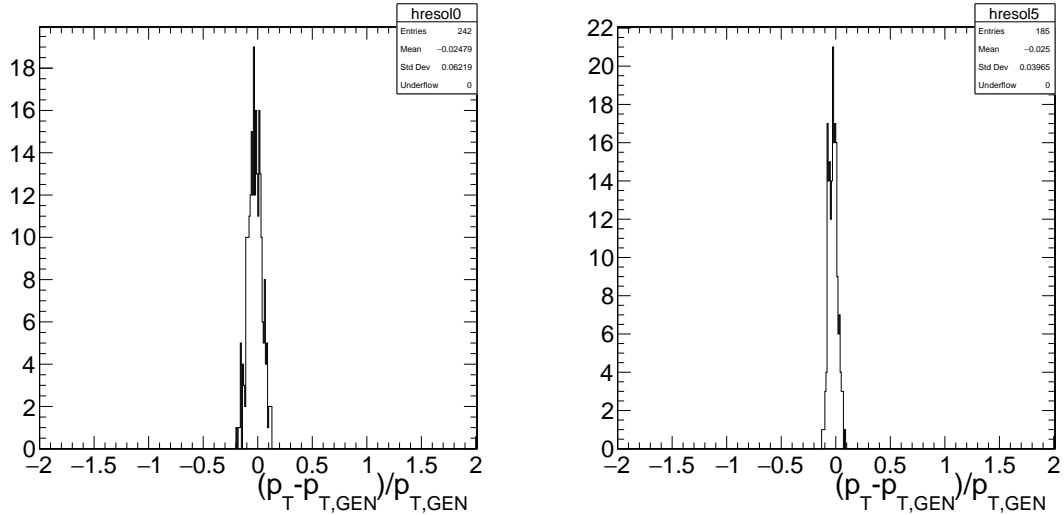


Figure 4.6: The jet energy resolution of neutrons with  $0 < |\eta| < 0.5$  and  $200 \text{ GeV} < p_T < 300 \text{ GeV}$  (left) or  $700 \text{ GeV} < p_T < 800 \text{ GeV}$  (right).

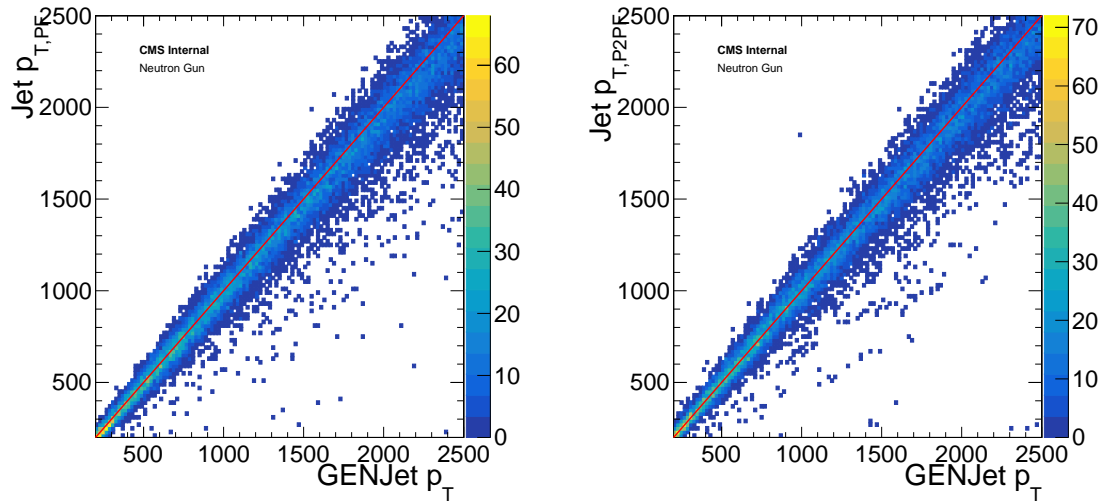


Figure 4.7: Comparison of the transverse momentum of the generator-level jets to the PF jets (left) and P2PF jets (right) in the region  $0 < |\eta| < 0.5$  with jet energy resolution smearing, using a neutron sample.

- <sup>1</sup> add table production cross section
- <sup>2</sup> explain P2PF AND neutron samples
- <sup>3</sup> het is nuttig te vermelden dat eerst de PFCand truc was gedaan, maar dat dat een signaal efficientie geeft die maximaal (en dus optimisitshc) is wegens gebrek aan tracker interacties

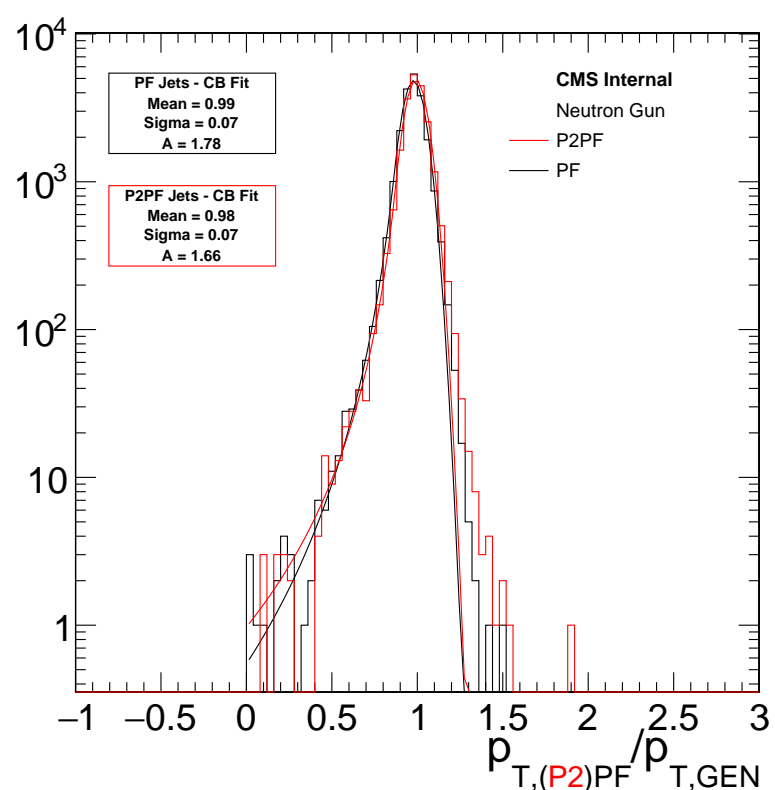


Figure 4.8: The jet energy resolution of the corrected P2PF jets (red) and PF jets (black), fitted with a Crystal Ball function.



# 5

1

2

## The Monojet Analysis

3 As has been described in Chapter 2, there are many searches for dark matter both at particle accelerators  
4 and elsewhere. At the LHC, one very promising channel is the monojet search, where the detection of  
5 dark matter is done by looking for missing energy in association with one or more jets. The dark matter  
6 particles are expected to pass through the detector without leaving any signal since they are neutral and  
7 only interact very weakly. They can however be detected indirectly as missing energy when they recoil  
8 off one or more jets coming from initial state radiation.

9 First, the event selection and the estimation of the background are described, respectively in Sections  
10 5.1 and 5.2. The included systematic uncertainties are described in Section 5.3. In Section 5.4,  
11 the obtained results are shown. The improvements achieved by going from the analysis strategy used in  
12 2015 to the 2016 version are detailed in Section 5.5. Finally, the results are interpreted in terms of the  
13 considered dark matter models in Section 5.6.

### 14 5.1 Event selection

15 In order to select events that have the Monojet signature illustrated in Figure 5.1, the trigger requires either  
16  $E_T^{miss} > 90$  GeV, where  $E_T^{miss}$  is the magnitude of the negative vectorial sum of the  $p_T$  of all particles at  
17 trigger level, or  $H_T^{miss} > 90$  GeV, where  $H_T^{miss}$  is calculated as the magnitude of the negative vectorial  
18 sum of the momenta of all jets with  $p_T > 20$  GeV. Muons are not taken into account to compute  $E_T^{miss}$   
19 and  $H_T^{miss}$ , so that the same trigger can be used to select the events for the muon control regions used for  
20 the background prediction. The trigger efficiency is above 98% for events passing the analysis selection  
21 described below.

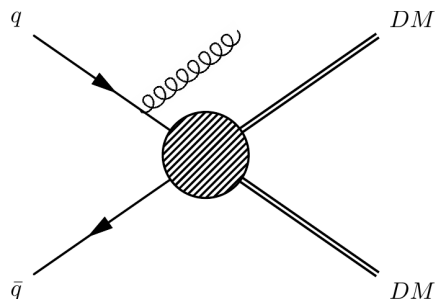


Figure 5.1: Illustration of dark matter production in the monojet final state.

22 Once the events have been fully reconstructed and the jets in the event have been corrected as de-

scribed in Section 4.3.6, an event selection is applied by requiring the missing transverse energy  $E_T^{miss}$  defined in Section 4.3.9 to be larger than 200 GeV in order to be consistent with the trigger turn-on. Additionally, the leading jet is required to have  $p_T > 100$  GeV,  $|\eta| < 2.5$ , and to pass the loose jet identification and pileup jet identification described in Section 4.3.6, as well as the jet cleaning. The jet cleaning is done by requiring a jet charged hadron energy fraction CHF  $> 0.1$  and a jet neutral hadron energy fraction NHF  $< 0.8$ . The same requirements are applied for the remaining jets to be taken into account, except for the  $p_T$  threshold which is at 30 GeV in this case. A cut on the difference in azimuthal angle between the  $E_T^{miss}$  and the first four leading jets of  $\Delta\phi(jet, E_T^{miss}) > 0.5$  is also applied to suppress the QCD background from mismeasurements of jet momentum or detector noise. The events are further cleaned by applying quality filters to remove events with badly reconstructed missing transverse energy. Finally, events containing a lepton, a photon, or a b-jet are vetoed as well.

The leptons are vetoed to suppress the electroweak backgrounds, such as  $W(l\nu) + \text{jets}$  and semileptonic diboson decays. Electrons (muons) are considered for the veto if they pass the loose selection and have  $p_T > 10$  GeV and  $|\eta| < 2.5(2.4)$ . In the case of tau leptons, they are required to have  $p_T > 15$  GeV and  $|\eta| < 2.3$ . They should also pass the tau identification criteria, which require a jet with an identified subset of particles with a mass consistent with the decay products of a hadronic tau and which are isolated with a pileup corrected isolation cut requiring less than 5 GeV of energy deposits within a radial cone of  $\Delta R < 0.3$ . Photons are required to have  $p_T > 15$  GeV,  $|\eta| < 2.5$ , and to pass the **loose identification** criteria. The photon veto is added to suppress the  $Z(\nu\nu) + \text{photon} + \text{jets}$  and  $W(l\nu) + \text{photon} + \text{jets}$  background processes, and to ensure there is no overlap with a similar dark matter search which investigates the final state consisting of missing energy and a photon. This rejects less than 1% of the signal. Finally, the b-jet veto reduces the top background by a factor 3 and only reduces the signal by 5 to 10%, depending on the type and mass of the mediator. The b-jets are tagged with the Combined Secondary Vertex algorithm described in Section 4.3.7, using the loose working point.

## 5.2 Background estimation

The dominant background comes from  $Z + \text{jet}$  events where the  $Z$  boson decays to two neutrinos. This produces the same signature of jets with missing energy as the signal, and results in an irreducible background. The second largest background consists of  $W + \text{jets}$  events with a leptonically decaying  $W$  boson. This background is already suppressed by the lepton veto, but a fraction of these events remain when the lepton is either not identified or outside of the detector acceptance. The remaining background events come from top quark decays, which are suppressed by the b-jet veto, semileptonic diboson ( $WW$ ,  $WZ$ , and  $ZZ$ ) decays, and QCD multijet events. The two main background contributions are estimated from five control regions in data consisting of dimuon, dielectron, single muon, single electron, and photon + jets events. The  $E_T^{miss}$  in these control regions is redefined in order to imitate the  $E_T^{miss}$  shape in the signal region. This hadronic recoil  $U$  is obtained by removing the leptons or the photon from the  $E_T^{miss}$  computation. The contributions from top quark decays and semileptonic diboson decays are estimated using simulated samples, while the QCD multijet background is estimated using a data-driven approach.

### 5.2.1 The $Z$ and $W$ background estimation

The yield of  $Z(\nu\nu)$  and  $W(l\nu) + \text{jets}$  events in the signal region is estimated from five control regions by using the ratio between data and MC in the control region, per bin of the recoil distribution. For the prediction using  $Z \rightarrow \mu\mu$  events in the dimuon control region for example, the predicted yield of  $Z \rightarrow \nu\nu$

events is given by

$$N_{Z(\nu\nu)} = \frac{N_{Z(\mu\mu)}^{data}}{N_{Z(\mu\mu)}^{MC}} N_{Z(\nu\nu)}^{MC} \quad (5.1)$$

$$= \frac{N_{\mu\mu}^{data} - N_{Bkgd}}{N_{Z(\mu\mu)}^{MC}} N_{Z(\nu\nu)}^{MC} \quad (5.2)$$

$$= \frac{N_{\mu\mu}^{data} - N_{Bkgd}}{N_{Z(\mu\mu)}^{MC}} R_{Z(\mu\mu) \rightarrow Z(\nu\nu)} N_{Z(\mu\mu)}^{MC} \quad (5.3)$$

- 1 The transfer factors, denoted by  $R$ , are derived from simulation and take into account the impact of lepton  
 2 acceptance and efficiency, as well as the additional  $E_T^{miss}$  requirement for the single electron control  
 3 region. They also include the difference in branching ratio and the relation between the differential cross  
 4 sections of the photon,  $W$ , and  $Z$  boson production as a function of the boson  $p_T$ . The transfer factors  
 5 are computed as a function of the recoil, and are shown for the five different control regions in Figure 5.2.  
 6 Furthermore, the  $Z/W$  ratio shown in the bottom right plot of Figure 5.2 provides an additional constraint  
 7 since the single lepton control regions are also used to estimate the  $Z(\nu\nu) +$  jets background.

8 The simulated samples used for the background estimation are generated at leading order (LO) using  
 9 the MADGRAPH generator, and corrected to next-to-leading order (NLO). These corrections introduce an  
 10 additional systematic uncertainty, but are crucial in order correctly represent the data, since the simulation  
 11 is approximately 40% higher than the data when using only LO calculations. The NLO QCD k-factors  
 12 are derived from samples generated at NLO with MADGRAPH5\_aMC@NLO, while the electroweak k-  
 13 factors are obtained from theoretical calculations [121–124]. The differential cross section as a function  
 14 of the boson  $p_T$  is shown in Figure 5.3 for photon,  $W$ , and  $Z$  production, and the obtained k-factors  
 15 are displayed in the ratio plots. More details on the different control regions are given in the following  
 16 description.

### 17 Dimuon control region

18 The traditional control region for the  $Z$  boson background is the dimuon control region. This region  
 19 is dominated by  $Z \rightarrow \mu\mu$  events, which are very similar to the  $Z(\nu\nu) +$  jets background events, the  
 20 only difference being the decay mode. The production mode and kinematics in the control region  
 21 are very similar, as well as the acceptance. However, the branching ratio of the  $Z$  boson into two  
 22 muons is 6 times smaller than the branching ratio to two neutrinos. As a result, the dimuon control  
 23 region contains about 10 times less  $Z$  boson events than the signal region. In order to improve this  
 24 statistical limitation, other control regions have been added as well.

25 In the dimuon control region the events are selected using the monojet triggers and applying the  
 26 same requirements as described in Section 5.1 for the signal region, using the recoil instead of  
 27 the missing transverse energy, except for the muon veto. Additionally, exactly two muons with  
 28 opposite charge and with  $p_T > 10$  GeV should be identified using the loose identification [described in Section ? \(or listed in Table ?\)](#). At least one muon is required to have  $p_T > 20$  GeV and to pass  
 29 the tight selection requirements [described in Section ? \(or listed in Table ?\)](#), and the leading muon  
 30 should also have a transverse momentum large than 20 GeV. Finally, the dimuon mass should be  
 31 between 60 and 120 GeV, corresponding to the  $Z$  boson mass.

### 33 Single muon control region

34 In order to model the second largest background, coming from  $W(l\nu) +$  jets events, a single muon  
 35 control region is typically used. This control region is in addition also used to constrain the  $Z(\nu\nu)$   
 36 + jets background. The events in the single muon control region are required to pass the monojet  
 37 triggers and event selection replacing the  $E_T^{miss}$  by the recoil obtained by removing the muon,  
 38 except for the muon veto. One muon should then pass the [tight selection](#) requirements and have  
 39  $p_T > 20$  GeV.

### 40 Dielectron and single electron control region

41 The dielectron and single electron control regions are completely analogous to the dimuon and

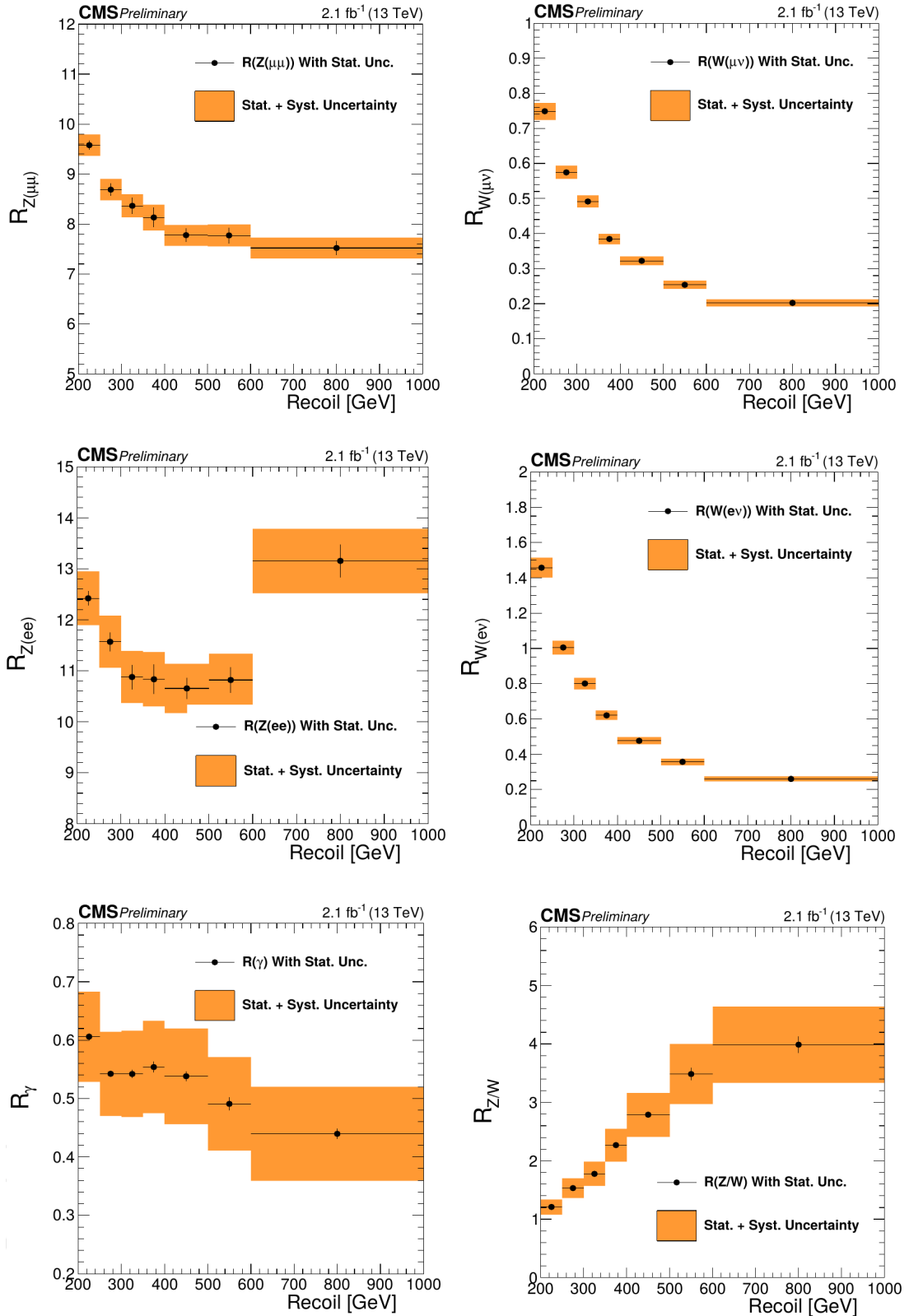


Figure 5.2: Transfer factors for the dimuon (top left), single muon (top right), dielectron (middle left), single electron (middle right), and photon + jets (bottom left) control regions. The ratio of the  $Z$  and  $W$  transfer factors is shown in the bottom right plot.

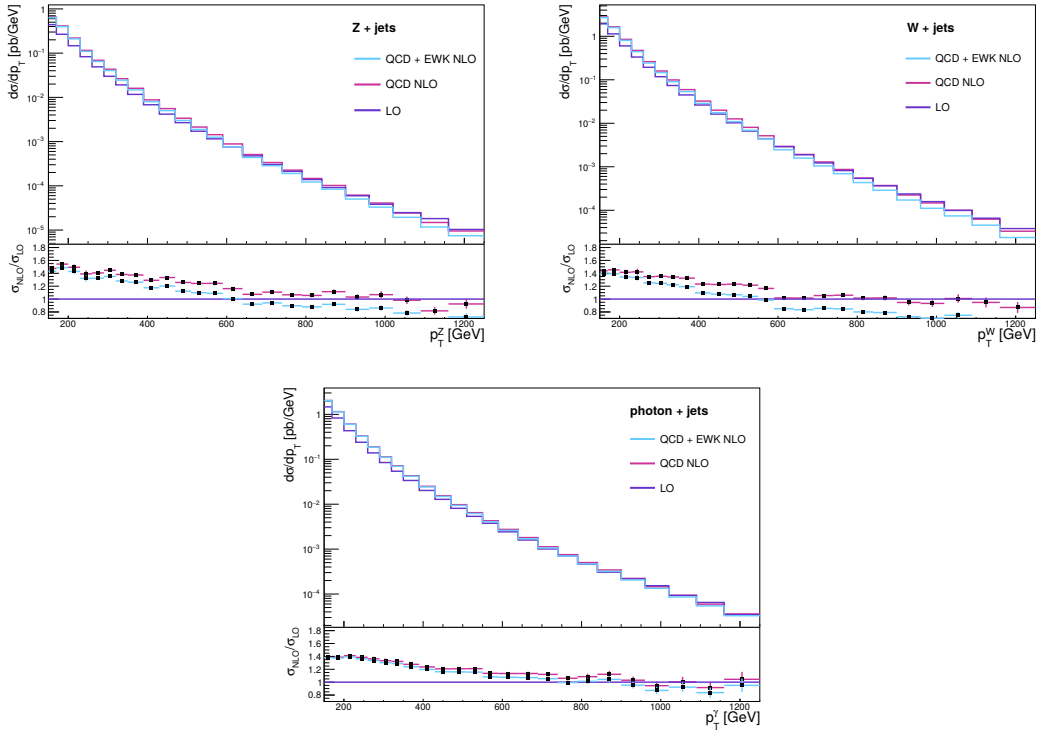


Figure 5.3: The differential cross section as a function of the boson  $p_T$  for photon,  $W$ , and  $Z$  production, with the resulting  $k$ -factors in the ratio plots.

single muon control regions, respectively. These events are required to pass the single electron triggers. Similarly to the dimuon control region, the events in the dielectron control region are required to pass the monojet selection, except for the electron veto. Instead, exactly two electrons with  $p_T > 10$  GeV are required to pass the loose identification described in Section ? (or listed in Table ?) In addition, at least one electron should pass the tight selection requirements and have  $p_T > 20$  GeV. Finally, the dielectron mass should be between 60 and 120 GeV, in order to be consistent with a  $W$  boson decay. transfer factor last bin due to isolation in trigger. The dielectron control region is used to constrain the  $Z \rightarrow \nu\nu$  background while the single electron control region is used to constrain the  $W(l\nu) + \text{jets}$  background. In the single electron control region, the events are required to have one electron passing the tight selection requirements and having  $p_T > 20$  GeV, analogously to the single muon control region. In this region, a large amount of QCD background is present. In order to reject most of those events, an additional cut on the  $E_T^{\text{miss}}$ , which includes the single electron, is added at 50 GeV. This reduces the QCD background by an order of magnitude.

#### Photon + jets control region

Due to its large yield, photon + jets control region provides the dominant constraint on the high- $p_T$  part of the  $Z(\nu\nu) + \text{jets}$  background. The selection of these events is done using the single photon triggers and applying the monojet selection, except for the photon veto. One photon is then required to pass the tight identification described in Section ? (or listed in Table ?) and to have  $p_T > 175$  GeV and  $|\eta| < 1.4442$ . Events with more than one photon passing the loose identification requirements described in Section ? (or listed in Table ?) are rejected.

### 5.2.2 The QCD background estimation

## 5.3 Systematic uncertainties

- For the main backgrounds, multiple systematic uncertainties on the transfer factors are taken into account. Experimental uncertainties are added for the muon efficiency, the electron efficiency, the lepton veto, the photon efficiency, and the photon purity in the photon + jets sample.

Uncertainties are also added from theory, to take into account variations of the factorization and renormalization scales, PDF uncertainties, and the NLO electroweak corrections. The former 3 uncertainties are shown in Figure 5.4 for the  $Z + \text{jets}$ ,  $W + \text{jets}$ , and photon + jets samples. The uncertainties are then propagated to the transfer factors, and are displayed in Figure 5.5. To evaluate the PDF uncertainty, the samples are reweighted with event-by-event scale factors representing the shift in the kinematic distributions from variations in the PDF. The transfer factors are then produced for each variation, and the RMS of the variation is taken as PDF uncertainty. Similarly, the renormalization and factorization scales are varied up and down by a factor 2, and the uncertainties are derived from the resulting transfer factors. For the electroweak corrections, the full correction is taken as an uncertainty.

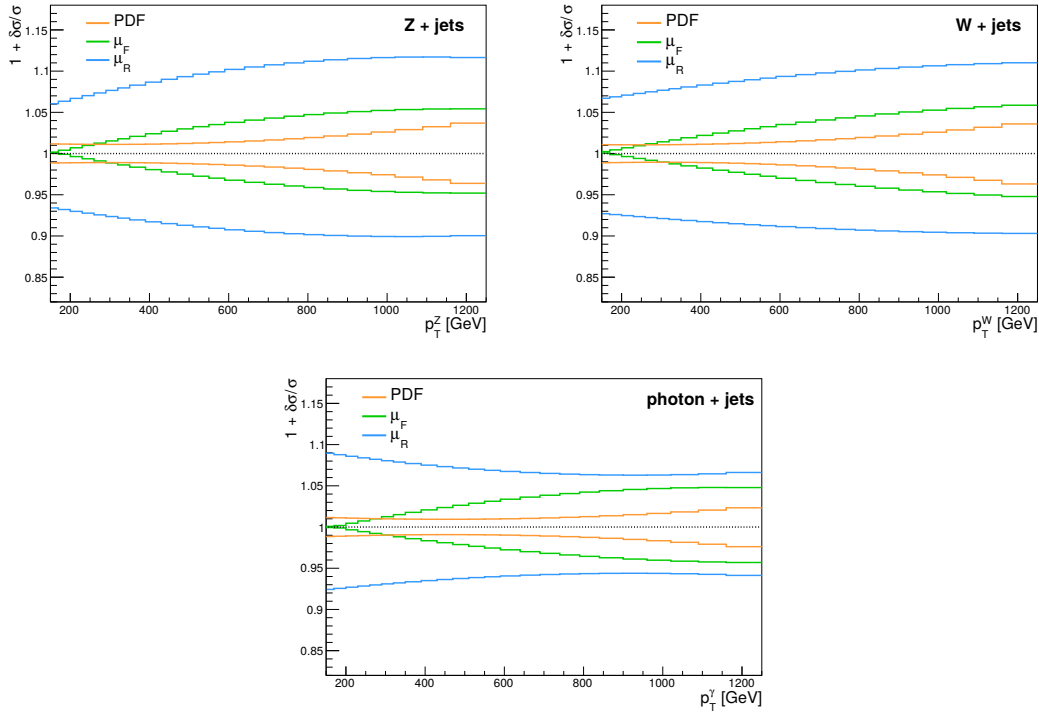


Figure 5.4: The PDF, renormalization, and factorization scale uncertainties for the  $Z + \text{jets}$  (top left),  $W + \text{jets}$  (top right), and photon + jets (bottom) samples. The uncertainties from the renormalization and factorization scales are obtained by separately varying them up and down by a factor 2.

## 5.4 Results

- The results are extracted by performing a binned fit to the missing energy spectrum, fitting simultaneously over the five control regions and the signal region.

## 5.5 Improvement going from the 2015 to 2016 analysis

- One of the improvements that were added to the monojet analysis is the use of MC samples generated at leading order for the estimation of the main backgrounds. This was possible by generating samples

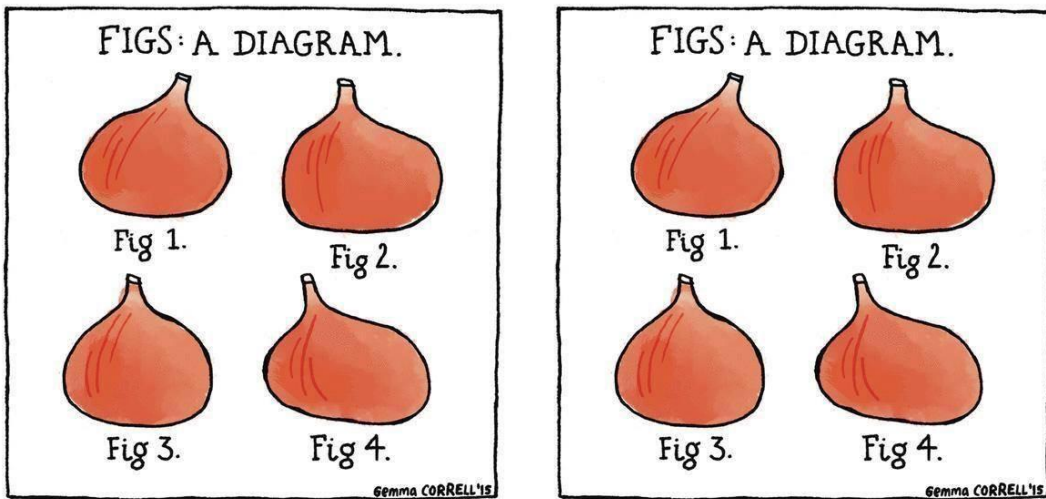


*Figure 5.5: .*

- <sup>1</sup> that are binned in photon,  $Z$ , or  $W$  boson  $p_T$ . As a result, no k-factors need to be applied to samples
- <sup>2</sup> generated at LO and no additional systematic uncertainties need to be introduced for this.

### <sup>3</sup> 5.6 Interpretation



# 6

1

2

## Search for SIMPs using Trackless Jets

3 The monojet dark matter search detailed in Chapter 5 can be complemented at high interaction cross  
4 sections by a different search which does not look for dark matter in the form of missing transverse  
5 momentum. Indeed, if the dark matter particles have an interaction cross section of the order of the  
6 **hadronic** interaction, they will interact in the detector, mainly in the calorimeters. The analysis described  
7 in this chapter is based on this scenario, and the considered simplified model is specified in [Section 2.3](#).  
8 In this model, the dark matter particles are produced in pairs through a new strongly interacting mediator,  
9 and give rise to a pair of trackless jets as signature. Since the produced strongly interacting massive  
10 particles (SIMPs) are neutral, the resulting jets can be distinguished from QCD jets using the jet charged  
11 hadron energy fraction (CHF).

12 Firstly, the applied jet and photon reconstruction and identification are described, as well as the spe-  
13 cific treatment applied for the primary vertex selection. The triggers that were designed specifically for  
14 this search, exploiting the CHF, are outlined in [Section 6.2](#). However, these triggers were found to be  
15 problematic and eventually **a standard trigger** was used instead. Next, the event selection is detailed in  
16 [Section 6.3](#) for both the signal and control regions. The strategy for the background estimation and the  
17 systematic uncertainties are discussed in [Sections 6.4](#) and [6.5](#), respectively. Finally, in [Sections 6.6](#) and  
18 [6.7](#), the results are shown and interpreted in terms of the SIMP simplified model described in [Section 2.3](#).

### 19 **6.1 Physics object reconstruction**

20 In this analysis, jets with a very small charged hadron energy fraction (CHF) are being searched for.  
21 Since these are rather peculiar jets, a good primary vertex selection and photon identification prove to  
22 play an important role **as well** in suppressing the main physics and reconstruction backgrounds in the  
23 **search region.** 

#### 24 **6.1.1 Jets**

25 For the jet reconstruction, the standard method described in [Section 4.3.6](#) is used. Although the jets in the  
26 signal samples are expected to be neutral, it is beneficial to use PF jets because they directly provide an  
27 unambiguous association of tracks to jets. The standard jet energy corrections are applied as well, while  
28 the standard jet identification criteria are not used, since several of the quality criteria would actually  
29 remove the neutral **signal jets**.

### 6.1.2 Photons

Since photons are reconstructed as neutral jets, photon + jets events are an important background for the control as well as the signal region. The photons therefore need to be identified and rejected, which is done using the standard photon loose identification described in Section 4.3.3. Further photon rejection is achieved by analysis-specific selections on conversions and on the jet neutral electromagnetic energy fraction, as described in Section 6.3.

### 6.1.3 Primary vertex

In the standard primary vertex reconstruction, the vertex with the highest  $\sum p_T^2$  is chosen, where the sum runs over the tracks associated to the vertex following the application of a deterministic annealing filter which assigns weights to sufficiently high-quality tracks that enter the vertex fit [114]. While in events with jets many tens of high-momentum tracks can usually be associated to a primary vertex, thus making primary vertex finding almost fully efficient and pure, in the case of a pair of neutral jets this is not the case any more. The underlying event and potentially initial state QCD radiation can still provide some tracks, but in extreme cases a wrong vertex is chosen, arising from a hard pileup collision.

The choice of a wrong vertex is not a problem in the case of signal events, which will pass in particular the CHF cuts in the event selection detailed in Section 6.3 just as easily. However, a wrongly chosen vertex in a Quantum Chromodynamics (QCD) background event leads to the jets having an artificially very low CHF, both in simulation and data, as the standard charged hadron subtraction (CHS) procedure will remove the tracks from the real hard vertex. This makes such event appear signal-like. At the tightest CHF cuts considered in this analysis, this fake background becomes dominant with respect to the real background of very rare jet fragmentation into predominantly neutral hadrons and photons. In Figure 6.1 an event display is shown that demonstrates such a wrong choice of vertex.

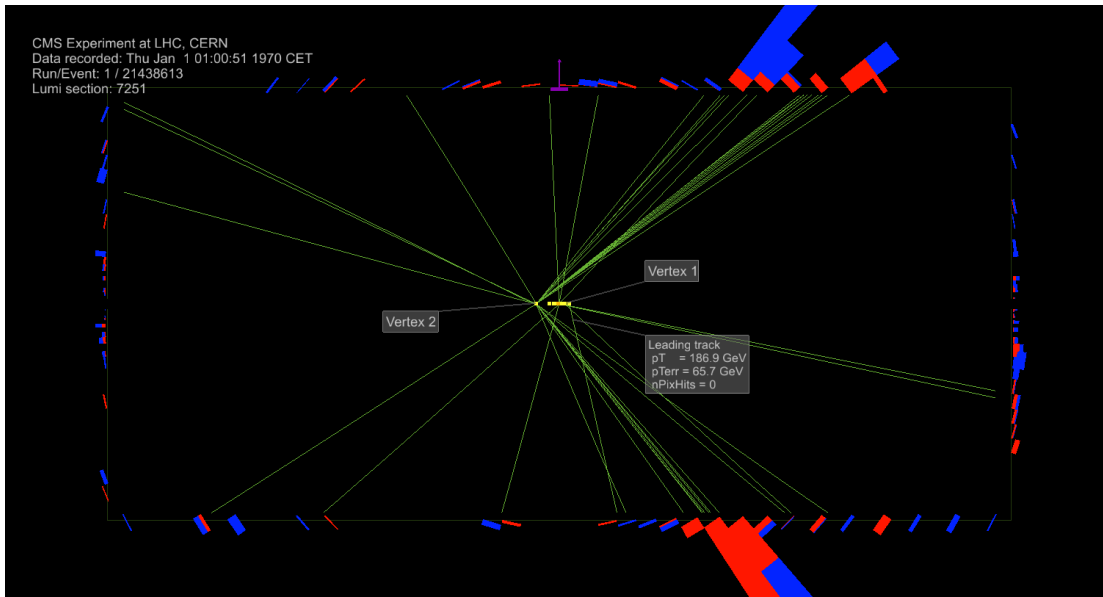


Figure 6.1: Event display showing a typical example of a wrong primary vertex selection in a MC simulated QCD event. Although "Vertex 2" is the real vertex of the hard collision, "Vertex 1" is selected because of the presence of a single high- $p_T$  track with poor momentum resolution and no pixel hits attached. As a result, the two visible high- $p_T$  jets (above 200 GeV), clearly with many tracks attached, are reconstructed with only 3% and 4% of charged energy fraction.

Investigating this problem, many events with a wrong vertex assignment were observed to have the highest- $p_T$  track being of poor quality, with a high momentum with large uncertainty, and no pixel hits. This alone, though, does not provide a sufficient handle to suppress this fake background, and a plain cut on number of pixel hits additionally comes at a cost of a large signal loss as well. The study of the simulated QCD multijet events with primary vertex misidentification also showed that the true vertex is

1 reconstructed as the second vertex in the list for the far majority of the cases. A second event reconstruction was therefore produced, rerunning the CHS and jet reconstruction based on selecting the second entry in the list of primary vertices to be the event's collision vertex. If this second vertex was the correct one, the jets will now have a large CHF in most of the cases, while the first event reconstruction yields low-CHF jets. In the event selection discussed in Section 6.3, it is then sufficient to ask both event reconstructions to pass the cut of low jet CHF, effectively suppressing this background induced from wrong primary vertex selection.

## 8 **6.2 Trigger selection**

9 Several triggers have been designed specifically for this analysis, as shown in Table 6.1. Four signal  
10 triggers were available, providing a trade-off between a high CHF and a low jet  $p_T$ . The CHF cut is  
11 always applied on both jets.

Trigger name	Type	Run range	Int. Lumi.
HLT_DiCentralPFJet170_CFMMax0p1_v*	Signal	> 274748	$33.1 \text{ fb}^{-1}$
HLT_DiCentralPFJet220_CFMMax0p3_v*	Signal	274748 – 281084	$5.91 \text{ fb}^{-1}$
HLT_DiCentralPFJet330_CFMMax0p5_v*	Signal	> 274748	$33.1 \text{ fb}^{-1}$
HLT_DiCentralPFJet430_v*	Signal	> 274748	$33.1 \text{ fb}^{-1}$
HLT_DiCentralPFJet170_v*	Control	> 274748	$0.101 \text{ fb}^{-1}$
HLT_SingleCentralPFJet170_CFMMax0p1_v*	Control	> 274748	$0.375 \text{ fb}^{-1}$

Table 6.1: Summary of the triggers designed for this analysis.

12 These triggers were designed by using QCD samples to test their performance before using them  
13 in data taking, since the signal samples do not simulate the trigger behaviour. The trigger efficiency of  
14 HLT\_DiCentralPFJet330\_CFMMax0p5 as a function of  $p_T$  and CHF is shown in Figure 6.2, using  
15 data and simulated QCD events. The signal efficiency measurement was first tried by taking a photon +  
16 jet sample, as photons would also give neutral jets. The photon was matched to the leading jet and the  
17 efficiency was measured at low CHF. However, the photon is in many cases reconstructed as an electron  
18 by the PF algorithm. Thus, the jet is reconstructed with a large electromagnetic energy fraction (EMF)  
19 and it does not mimic the SIMP signal.

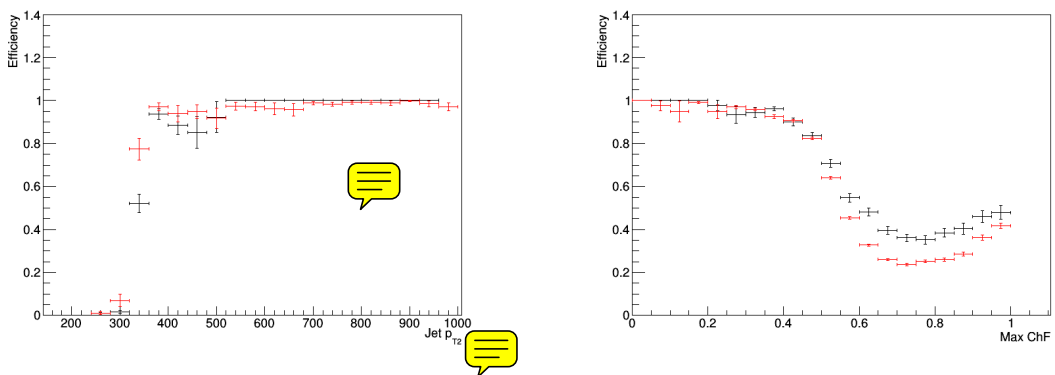


Figure 6.2: The HLT\_DiCentralPFJet330\_CFMMax0p5 trigger efficiency as a function of  $p_T$  (left) and CHF (right). Comparison between data (black) and QCD simulation (red).

20 Once the neutron signal samples described in Section 4.4 were generated, the one generated with a  
21 SIMP mass of 700 GeV was used instead. The obtained trigger efficiency as a function of  $p_T$  and CHF is  
22 shown in Figure 6.3 for HLT\_DiCentralPFJet330\_CFMMax0p5, comparing the data and the signal-like  
23 events. This shows that the trigger reaches a plateau at only 60% signal efficiency. The origin of the  
24 inefficiency was found to come from a requirement asking at least one charged particle in the jets. This  
25 explains why the trigger efficiencies turn on at the expected values when using data or simulated QCD  
26 events, while it is largely inefficient in signal-like simulation which generates neutral jets.

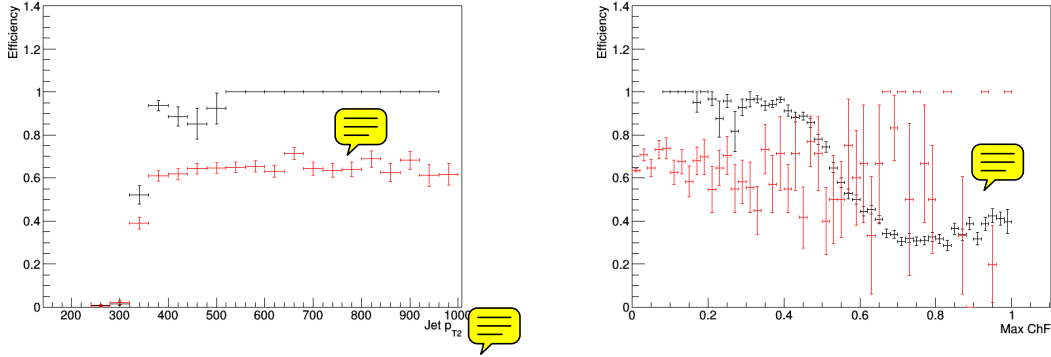


Figure 6.3: The `HLT_DiCentralPFJet330_CFMMax0p5` trigger efficiency as a function of  $p_T$  (left) and  $CHF$  (right). Comparison between data (black) and signal-like MC (red).

Consequently, the single jet trigger `HLT_PFJet450` has been used for the analysis. It was selected because it has the lowest threshold among the unprescaled<sup>1</sup> single jet triggers. The trigger efficiency for the data was measured using the single muon events, and is defined as

$$\epsilon = \frac{\text{Obs}(\text{HLT\_Jet450 and HLT\_IsoMu24})}{\text{Obs}(\text{HLT\_IsoMu24})}, \quad (6.1)$$

where Obs in this case is the  $p_T$  spectrum of the leading jet for events that fired the single muon (and single jet) trigger. The jets are required to have a muon energy fraction smaller than 0.3 in order to avoid jets with large difference in the online and offline  $p_T$ . This difference can arise when the offline PF jet contains a high- $p_T$  muon. Since the online jet is reconstructed using only information from the calorimeters, this can significantly change the total  $p_T$  of the jet between online and the offline PF jet. The trigger efficiency was also measured in the simulated QCD and neutron signal samples. In this case the denominator is the  $p_T$  spectrum of leading jet without any trigger selection, while the numerator is the  $p_T$  spectrum of the events firing the single jet trigger. Figure 6.4 shows the turn-on curves for data, QCD events, and the signal-like events. The trigger efficiency was found to be 98% for jets with  $p_T > 550$  GeV.

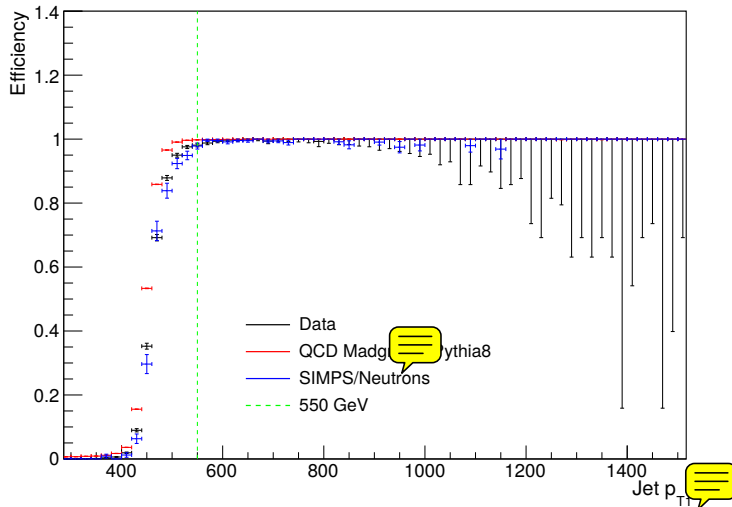


Figure 6.4: The `HLT_PFJet450` trigger efficiency turn-on as a function of the offline leading jet  $p_T$ , for data, QCD events, and the signal-like events. The  $p_T$  cut used in the event selection is shown with a green dashed line.

<sup>1</sup>Triggers with a lower  $p_T$  threshold exist, but only a fraction of the events is kept due to the otherwise very high rate. This is called prescaling.

### 6.3 Event selection

The event selection aims to select back-to-back dijet events with a low CHF. As a baseline selection, the two highest- $p_T$  jets are required to have  $p_T > 550$  GeV, in order to ensure the jets to be above the turn-on of the trigger. Furthermore, they are required to have  $|\eta| < 2.0$ , placing them fully within the tracking volume, thus suppressing backgrounds from jets that have a low CHF due to tracks falling out of tracker acceptance. Since the SIMPs do not undergo parton showering, while QCD partons undergo final state radiation, events with SIMPs have a lower number of jets than QCD multijet events, as can be seen from the top right plot in Figure 6.6. Events containing additional jets with  $p_T > 30$  GeV in the full  $\eta$  acceptance of the CMS calorimeters on top of the two leading jets are therefore vetoed.

A photon veto is also applied to suppress photon + jets events. This is done by rejecting events with a photon within  $\Delta R < 0.1$  of the leading or subleading jet, using the loose working point of the cut based photon identification to identify photons, as described in Section 4.3.3. In some cases, however, jets have a large photon energy fraction, above 0.8, but the photon in the jet does not pass the loose identification requirements, for instance when there is a photon conversion in the tracker. In order to reject photon + jets events more efficiently, an additional cut is applied when the jet photon energy fraction is greater than 0.8 and the photon in the jet does not pass the loose identification. The events are rejected if conversions with  $p_{T,\text{conv}}/p_{T,\gamma} > 0.3$  are matched to the photon within  $\Delta R < 0.2$ . In addition, the 2 jets are required to have a neutral electromagnetic energy fraction lower than 0.9, corresponding to one of the standard tight jet identification requirements mentioned in Section 4.3.6. The full jet ID is not applied, since the requirements on e.g. the neutral hadronic energy fraction and the charged multiplicity would reject the signal events.

In order to avoid any problems related to the striking discrepancy between data and simulation observed for events with only one reconstructed vertex in the top left plot of Figure 6.6, at least two reconstructed vertices are required. Additionally, the azimuthal separation of the two selected jets is required to be  $\Delta\phi > 2$ . Finally, noise filters are applied in order to reject instrumental background, mostly coming from beam halo.

Table 6.2 shows the number of events remaining in data, for simulated QCD events, and for 2 signal samples, after consecutively applying the described selection cuts. In Figure 6.5, data, QCD multijet simulation, and signal are compared after these selections, for the  $p_T$ ,  $\eta$  and CHF of the two leading jets. Figure 6.6 shows the number of vertices, number of jets,  $\Delta\phi(\text{jet1}, \text{jet2})$ , and  $H_T$  of the events. In some cases, the cut of the variable being shown is removed. The bump and long tail that can be seen in the data for the  $\Delta\phi(\text{jet1}, \text{jet2})$  distribution contain events coming from processes with a heavy vector boson, such as Z + jets or W + jets, or  $t\bar{t}$  events. The simulation instead shows a steeply falling spectrum since only QCD dijet events are shown.

selection cut	yield			
	data	QCD MC	SIMP ( $m_\chi = 1$ GeV)	SIMP ( $m_\chi = 1000$ GeV)
$p_T^{j1,j2} > 550$ GeV	2540420	3152550	773	5.7
$ \eta_{j1,j2}  < 2.0$	2441240	2980320	748	5.6
# jets = 2	534053	587670	636	4.9
photon veto	531366	586674	636	4.9
# vertices $\geq 2$	531244	586641	636	4.9
$\Delta\phi(j1, j2) > 2$	531207	586641	636	4.9
noise filters	528614	582184	634	4.9

Table 6.2: Number of events remaining after the listed selection cuts in data, QCD events, and for 2 signal samples as well.

As will be detailed in Section 6.4, the background is predicted from a data control region where at least one of the leading jets has a high CHF, above 0.25. No further selection on the second reconstruction with

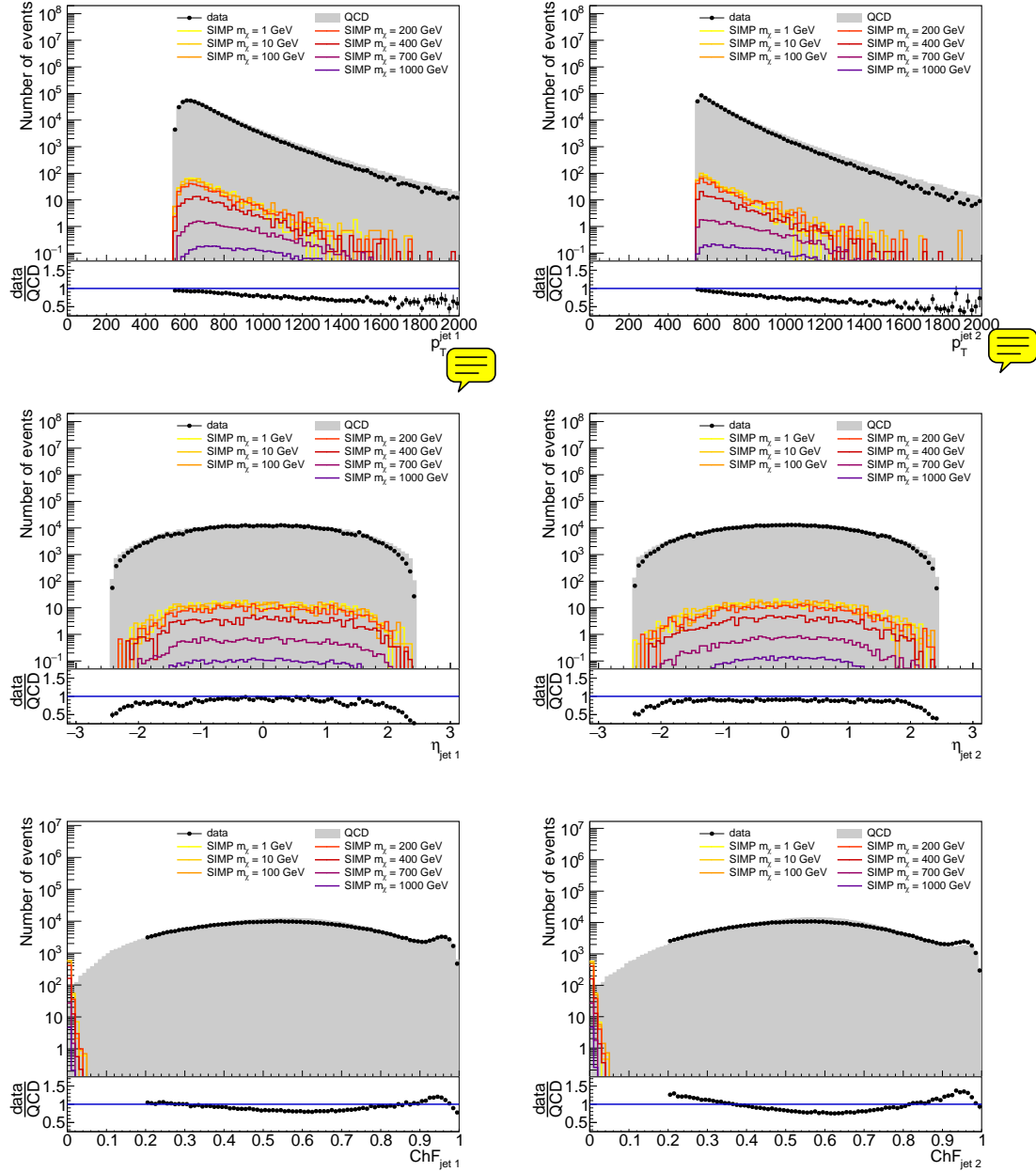


Figure 6.5:  $p_T$ ,  $\eta$  and CHF of the leading (left) and subleading (right) jet. The selection cuts are applied, except for the cut on  $\eta$  in the corresponding plot.

respect to the second primary vertex is applied for the control region, since the presence of at least one jet with a large CHF avoids the problem of the wrong selection of primary vertex detailed in Section 6.1.

In the case of the signal region selection, both jets are required to have  $\text{CHF} < x$ , where  $x$  is the signal cut being considered. In this case, the cut is applied for both reconstructions starting from the first and second primary vertex. The values of  $x$  considered in this analysis defining the signal regions are 0.03, 0.04, 0.05, 0.1, 0.15, and 0.2.

## 6.4 Background estimation

The main background for this analysis are QCD multijets. This background is estimated from data, as the simulation does not describe the data well, especially at low CHF. The signal events can then be

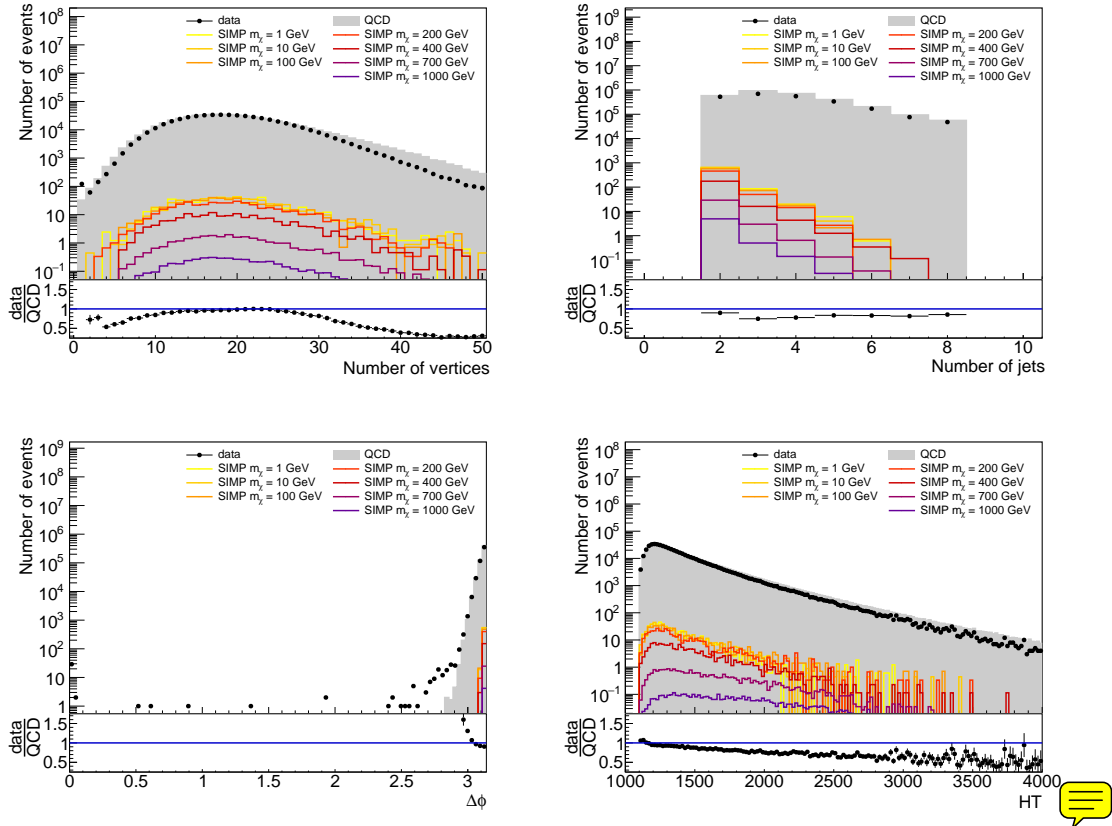


Figure 6.6: Number of vertices, number of jets,  $\Delta\phi(\text{jet1}, \text{jet2})$ , and  $H_T$  distributions, with selection cuts applied. The requirement on the number of vertices is not applied for the corresponding plot, the cut on the number of jets is not applied for the number of jets distribution, and the  $\Delta\phi$  cut is similarly not applied for the corresponding distribution.

1 distinguished from this background using the jet CHF. A second background comes from photon + jets  
 2 events. However, this background is efficiently removed by applying a photon veto.

### 3 6.4.1 Photon + jets

4 The photon + jets background is verified to be negligible and well within any other systematic uncertainty  
 5 on the background prediction. The photon veto works well, especially the cut on the jet neutral electro-  
 6 magnetic fraction, and no events from the used simulated photon + jets sample remain after applying  
 7 a cut of  $\text{CHF} < 0.1$ . Additionally, the events remaining just above that cut are partly contained in the  
 8 overlapping QCD multijets sample already.

### 9 6.4.2 QCD multijets

10 The QCD multijet background is estimated from data, since the simulation does not describe the data  
 11 well, especially at low CHF, as can be seen from Figure 6.7 which compares the CHF distribution in the  
 12 control region to the QCD MC. In this plot the subleading jet is required to have a large CHF, in order to  
 13 stay in the control region.

14 As a first step, the efficiency of the CHF cut is measured in the control region, by requiring one jet to  
 15 have  $\text{CHF} > 0.25$  and applying the CHF cut on the other jet. The measurement was done in bins of jet  
 16  $p_T$  and  $\eta$ . The number of QCD events in the signal region is then predicted by using any QCD dijet event  
 17 passing the selection cuts listed in Table 6.2 and applying the appropriate  $p_T$  and  $\eta$  dependent CHF cut  
 18 efficiencies on the two leading jets. Figure 6.8 shows the measured 1D efficiency as a function of the CHF  
 19 cut for various bins in  $p_T^{\text{jet}}$  and  $\eta_{\text{jet}}$ , as measured in the QCD MC. There is a strong dependence on the

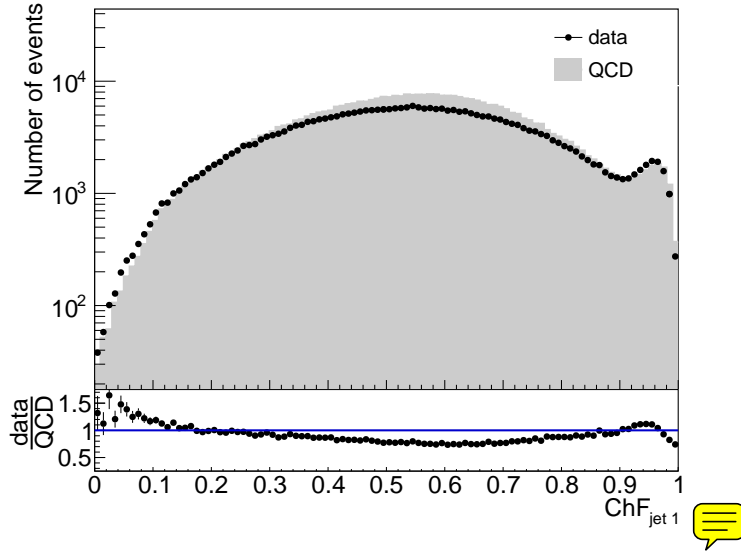


Figure 6.7: Data-MC comparison of the charged energy fraction of the leading jet, tagging events with subleading jet CHF > 0.5.

1 jet  $p_T$ , and a less pronounced dependence on the jet  $\eta$  at low CHF. The efficiencies are the highest for the  
 2  $1.0 < |\eta| < 1.25$  bin, which can be attributed to this being the barrel-endcap transition region where most  
 3 of the tracker material budget is located. The dependence on the jet  $p_T$  arises from the reconstruction. As  
 4 can be seen from the left plot in Figure 6.9, at generator level the CHF is independent of the jet  $p_T$ , as  
 5 one would expect. After reconstruction, as demonstrated in the right plot of Figure 6.9, a  $p_T$  dependence  
 6 arises due to the known degradation of tracking efficiency in dense jet environments, which becomes  
 7 more of an issue for very high  $p_T$  and thus collimated jets.

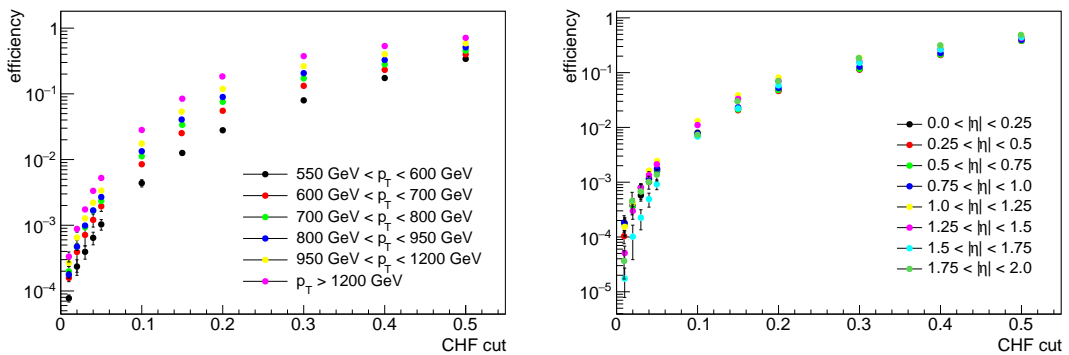


Figure 6.8: The efficiency of several CHF cuts in QCD MC, binned in  $p_T$  (left) and  $\eta$  (right).

8 A closure test is performed to validate this background prediction method, by comparing the MC truth  
 9 and the 1- and 2-leg predictions in MC. The MC truth shows the yield after applying the CHF cuts on  
 10 both jets. For the 1-leg prediction the CHF cut is applied on one jet and **the event is then scaled** by the  
 11 measured  $p_T$ - and  $\eta$ -dependent efficiency for the other jet. For the 2-leg prediction, the efficiencies are  
 12 applied for both jets, and no CHF cut is applied directly.

13 As a first check the closure test was **also** performed at the generator level, using the GenJets, which are  
 14 reconstructed from the generator level particles. This comparison is done in exclusive bins in ( $CHF_{jet1}$ ,  
 15  $CHF_{jet2}$ ), as illustrated in Figure 6.10. From Figure 6.11 one can see that there is a good agreement  
 16 between MC truth, 1-, and 2-leg predictions. This shows that there are no relevant physics correlations  
 17 between the 2 jets, an essential prerequisite for this background prediction to work well. The  $p_T$  and  $\eta$

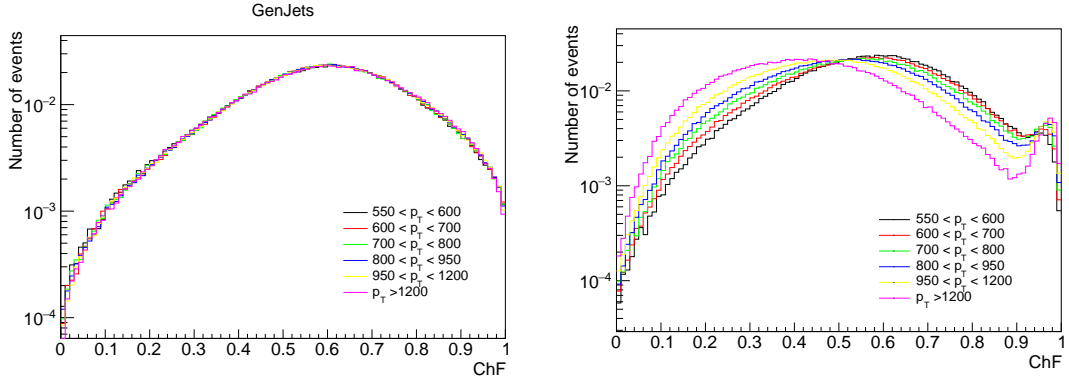


Figure 6.9: The CHF per bins of jet  $p_T$ , for generator level (left) and reconstructed (right) jets.

1 binning seems adequate as well.

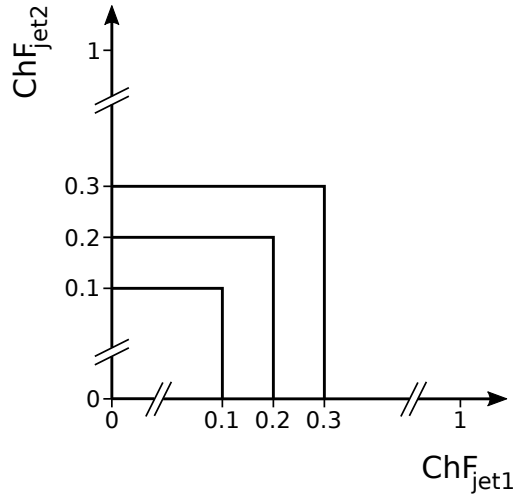


Figure 6.10: Illustration of the exclusive bins in the leading and subleading jet CHF, used for the closure test and the data vs. prediction comparisons.

2 Next, the closure test is performed with reconstructed jets, as shown in the left plot of Figure 6.12,  
3 using the exclusive binning. For the MC truth, the CHF cut is applied on the 2 leading jets of the standard  
4 jet collection, as well as the 2 leading jets of the jet collection created when using the second vertex as  
5 primary vertex. This extra cut is a part of the signal region event selection described earlier, designed to  
6 remove events where the wrong primary vertex was chosen and the charged fraction of the jets is removed  
7 by CHS. However, there is still a small discrepancy between the MC truth and the prediction at the tightest  
8 CHF cuts. This is mainly due to a very small number of events where the wrong vertex was chosen, but  
9 where the correct one is not the second one.

10 The closure test on MC is also performed in inclusive bins, as used in the signal region event selection,  
11 by applying a cut on the CHF of both jets. This is shown in the right plot of Figure 6.12, with the applied  
12 CHF cut on the x-axis. For the MC truth, the statistical uncertainty is determined per HT-binned QCD  
13 sample, using asymmetric vertical bars with correct coverage for event counts with Poisson variates when  
14 less than 10 events remain, and the square root of the remaining number of events otherwise. In this way,  
15 the statistical uncertainty correctly reflects the contribution of HT bins with few or no events left. The total  
16 statistical uncertainty is then calculated by multiplying the uncertainty per HT bin by the corresponding  
17 weight for this HT bin, and adding them quadratically. The systematic uncertainty on the background  
18 prediction is then defined as the difference between the MC truth and the prediction, unless it is smaller  
19 than the statistical uncertainty on the MC truth. In that case, the uncertainty on the MC truth is taken as  
1 systematic uncertainty.

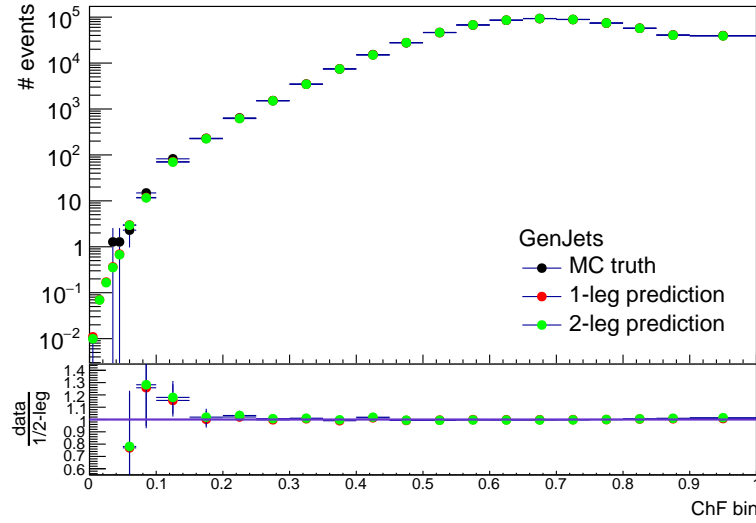


Figure 6.11: Closure test using GenJets.

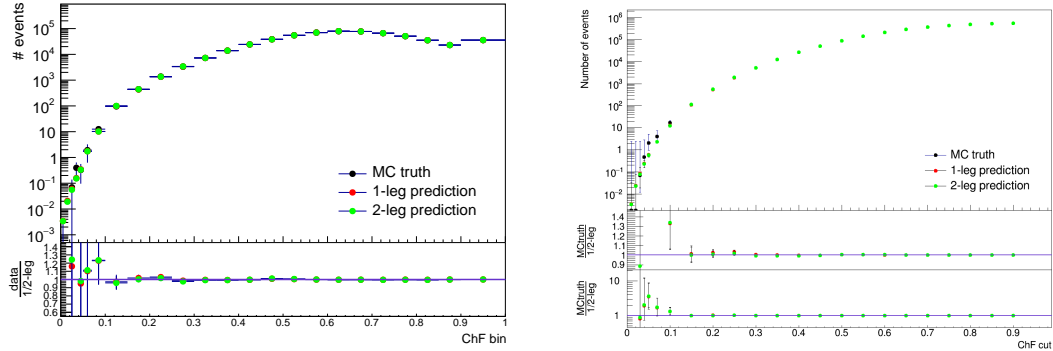


Figure 6.12: Closure test in MC using an exclusive (left) or inclusive (right) binning in CHF.

The QCD background prediction in data is shown in Figure 6.13 as a function of the exclusive CHF bins, using the `HLT_PFJet 450` single jet trigger. The data is blinded in the signal region below CHF = 0.05. A distinction is made between the run periods B to F (left) and G to H (right). There is a clear deviation below a CHF of 0.4 for run periods B to F, while the agreement is very good down to CHF = 0.05 for run periods G and H. The main difference between these 2 datasets is the issue with the Tracker APV pre-amplifier saturation, described in Section 3.2.6.1, which was solved from run period G onwards.

To first order, the measured CHF cut efficiencies should absorb the effects of tracking inefficiencies caused by the APV pre-amplifier saturation problem. However, this effect is also reflected in the distribution of the number of vertices. As is shown in Figure 6.14, a subtle effect causes the data and the prediction from data to disagree in the distribution of the number of vertices for run periods B to F, while a good agreement is obtained for run periods G to H. **As there are not enough statistics in order** to derive the CHF efficiencies reliably in bins of number of vertices as well as  $p_T$  and  $\eta$ , a recovery of the data in this way is not possible. A reweighting was also performed, using a fit to the ratio of data divided by the 2-leg prediction per CHF bin. Figure 6.15 shows the data versus data prediction comparison in run period E, applying the reweighting based on the number of vertices in the event, per CHF bin, and a clear improvement can be observed for the 2-leg prediction. In contrast, the 1-leg prediction has not been reweighted and still shows the original disagreement. This reweighting can however not be used in the signal region, where very few events remain. As a result, the analysis is performed with run periods G and H only, corresponding to an integrated luminosity of  $16.1 \text{ fb}^{-1}$ .

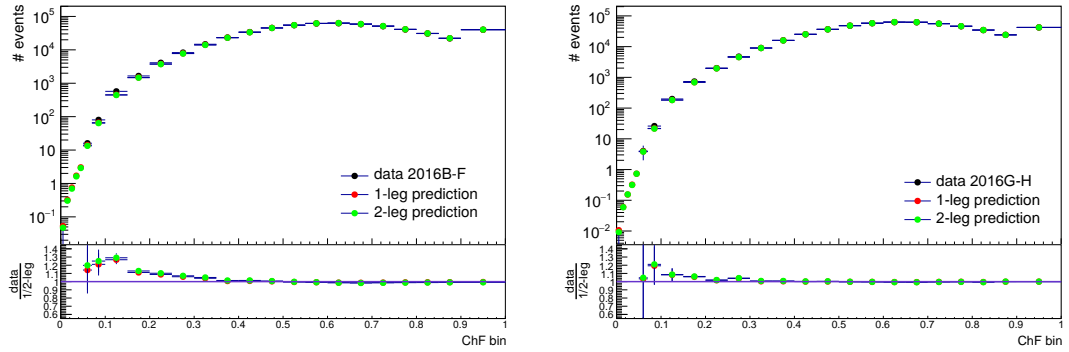


Figure 6.13: The 1- and 2-leg predictions from data, as well as the data (above  $CHF = 0.2$ ) as a function of the exclusive  $CHF$  bins, for run periods B-F (left) and G-H (right).

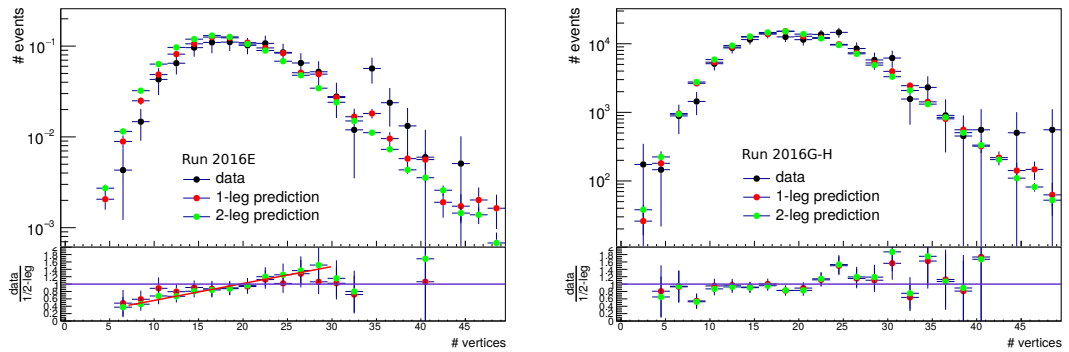


Figure 6.14: The distribution of the number of vertices for data, 1-leg, and 2-leg prediction using data from run period E (left) and run periods G-H (right).

## 6.5 Systematic uncertainties

For the signal prediction, systematics are included for the luminosity, the jet energy corrections, and the trigger inefficiency at 550 GeV due to the turn-on. The systematic for the luminosity amounts to 2.5%. The systematic uncertainty coming from the jet energy corrections is computed by varying the jet energy by the correction and recalculating the yield after applying the selection cuts and the  $CHF$  cut. Depending on the SIMP mass and the  $CHF$  cut, this uncertainty varies between 0.4% and 3.9%. A systematic uncertainty is also included to take into account the trigger inefficiency at 550 GeV due to the turn-on. This is done by taking a 100% uncertainty on the efficiency, which gives a 2% systematic uncertainty for the signal. This method does not take into account the fact that the turn-on was determined for one jet only and the inefficiency is strongly reduced when two jets with a similar  $p_T$  are present in the event. However, some signal events have one of the two jets with  $EMF = 0$ . In this case the jet which does not contain electromagnetic energy would not fire the single jet trigger and these events become single jet events from the trigger point of view. The 2% uncertainty is therefore conservative as it represents the worst case scenario. The photon and conversion veto was found to be 100% efficient on the signal, and as a result this systematic is negligible. The effect of pileup was considered to be negligible as well, as the distribution of the number of vertices is very similar for the data and SIMP samples. As an example the data is compared to the SIMP sample with  $m_\chi = 1000$  GeV in Figure 6.16, which shows there is a good agreement in the bulk of the distribution with some deviations in the tails only.

As mentioned in Section 6.4, the main systematic uncertainty on the background prediction is obtained from the closure test in MC, by taking the difference between the MC truth and the prediction, unless it is smaller than the statistical uncertainty on the MC truth, in which case the uncertainty on the MC truth is taken as systematic uncertainty. This uncertainty varies between 4% and 3416%, depending on the  $CHF$  cut. As for the signal, the trigger inefficiency due to the turn-on at 550 GeV is also taken into

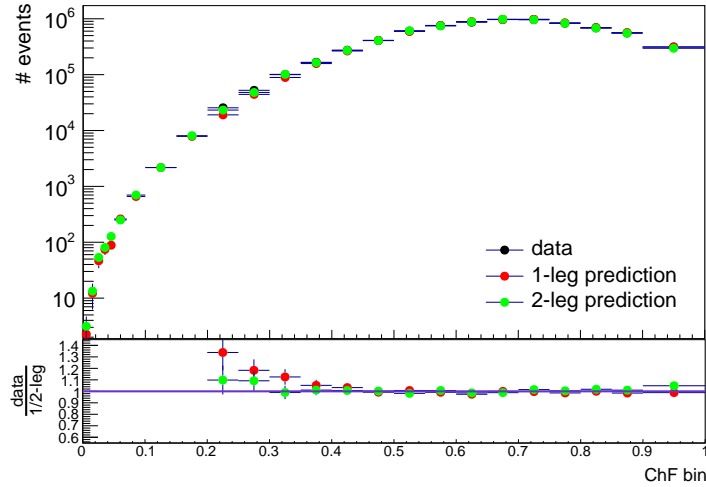


Figure 6.15: The 1- and 2-leg predictions from data, as well as the data (above CHF = 0.2) as a function of the exclusive CHF bins for run period E, reweighting the 2-leg prediction to data based on the number of vertices in the event, per CHF bin.

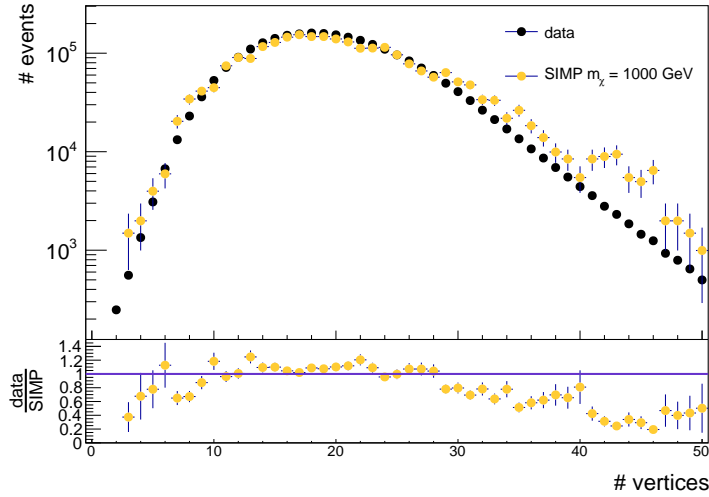


Figure 6.16: The distribution of the number of vertices in data compared to the SIMP signal with  $m_\chi = 1000$  GeV.

account, yielding an additional 2% systematic uncertainty.

## 6.6 Results

Table 6.3 shows the number of predicted and observed events, per considered CHF cut. The prediction is done using the 1-leg data prediction, as this provides slightly smaller uncertainties. The statistical uncertainty, as well as the systematic uncertainty from the closure test described in Section 6.5, are given.

A cut of  $\text{CHF} < 0.05$  is chosen, to reject most of the QCD background. The background is then reduced to the level of about one event, and a large uncertainty does not have big consequences. Moreover, the uncertainty from the closure test is reduced when taking into account the smaller statistical uncertainty on the number of background events during the limit calculation. In addition, the expected sensitivity does not improve significantly at tighter CHF cuts, and the closure tests start to run out of statistics. The dominating uncertainty then comes from the closure test, and amounts to 250% in this case.

Model-independent limits are derived for a  $\text{CHF} < 0.05$  cut, using the  $CL_S$  criterion [125, 126] with

CHF cut	data prediction	QCD MC prediction	observed	SIMP signal [ $m_\chi$ ]	
				1 GeV	1000 GeV
0.2	$902 \pm 5$ (stat.) $\pm 38$ (syst.)	$546.5 \pm 0.6$	969	634	4.9
0.15	$210 \pm 2$ (stat.) $\pm 18$ (syst.)	$111.1 \pm 0.4$	229	634	4.9
0.1	$26.9 \pm 0.3$ (stat.) $\pm 8.9$ (syst.)	$12.6 \pm 0.2$	30	634	4.9
0.07	$5.1 \pm 0.1$ (stat.) $\pm 4.4$ (syst.)	$2.3 \pm 0.2$	4	634	4.9
0.05	$1.28 \pm 0.03$ (stat.) $^{+ 3.24}_{- 1.28}$ (syst.)	$0.6 \pm 0.1$	0	634	4.9
0.04	$0.55 \pm 0.02$ (stat.) $^{+ 2.81}_{- 0.55}$ (syst.)	$0.24 \pm 0.09$	0	633	4.9
0.03	$0.22 \pm 0.01$ (stat.) $^{+ 7.68}_{- 0.22}$ (syst.)	$0.08 \pm 0.07$	0	632	4.9

Table 6.3: Number of predicted (using the 1-leg prediction from data) and observed events for the considered cuts. The expected number of signal events is also given for the  $m_\chi = 1$  GeV and  $m_\chi = 1000$  GeV scenarios.

- 5 the LHC style test statistic in which the systematic uncertainties are modelled as nuisance parameters.  
 6 This was done using the RooStat-based Combine tool, taking into account the systematic uncertainties  
 7 detailed in Section 6.5, as well as the statistical uncertainties on signal and background predictions. All  
 8 included systematic uncertainties are profiled with a lognormal prior, except for the uncertainty coming  
 9 from the closure test, which is profiled with a gamma function since it arises from limited statistics. The  
 10 resulting expected fiducial cross section is  $\sigma_{\text{fid}}^{95\%} = \sigma \times A \times \epsilon = 0.17$  fb. With zero observed events, the  
 11 observed model-independent lower limit is found to be  $\sigma_{\text{fid,obs}}^{95\%} = 0.18$  fb.

## 6.7 SIMP model interpretation

13 Limits are also derived on the production cross section for the SIMP simplified model, using the same  
 14 method as described for the model-independent limits. The expected limits on the production cross  
 15 section are shown for SIMP masses between 1 and 1000 GeV in Figure 6.17, using a cut of CHF < 0.05.  
 16 In this case, the search is sensitive to all the generated SIMP mass points, up to 1000 GeV.

17 Figure 6.18 shows the expected and observed limits when including the observation of zero events  
 18 in the signal region. The expected and observed limits, and the theoretical cross section are given with  
 19 respect to the generator level cuts applied in the signal sample generation,  $p_T^\chi > 200$  GeV and  $|\eta_\chi| < 2.5$ .  
 20 The shown theoretical cross section is also given per SIMP mass point in Table ???. In summary, no  
 21 significant excess above the expected background is observed, and the considered SIMP simplified model  
 22 is ruled out for SIMP masses up to 1000 GeV.

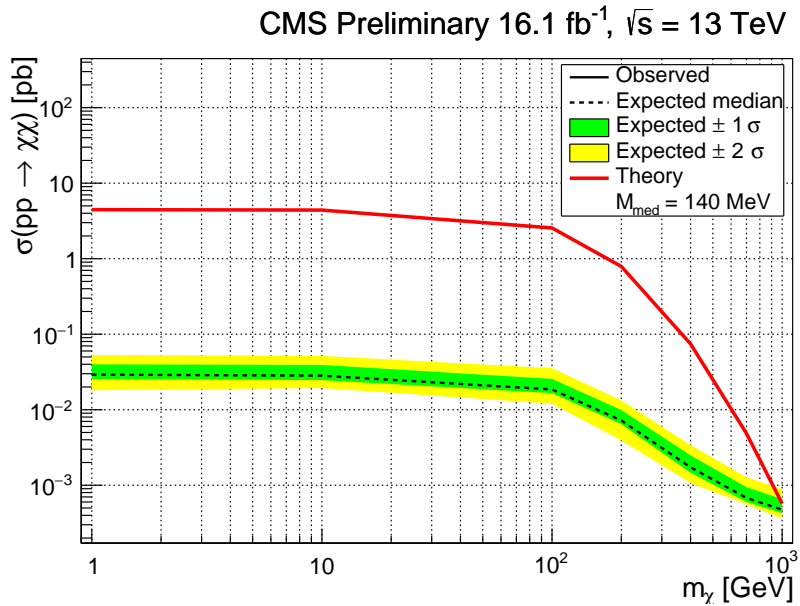


Figure 6.17: The expected limits on the production cross section, obtained without looking in the signal region, for SIMP masses between 1 and 1000 GeV, with  $1\sigma$  and  $2\sigma$  bands is shown, as well as the theoretical prediction (red), with respect to the generator level cuts ( $p_T^\chi > 200$  GeV and  $|\eta_\chi| < 2.5$ ).

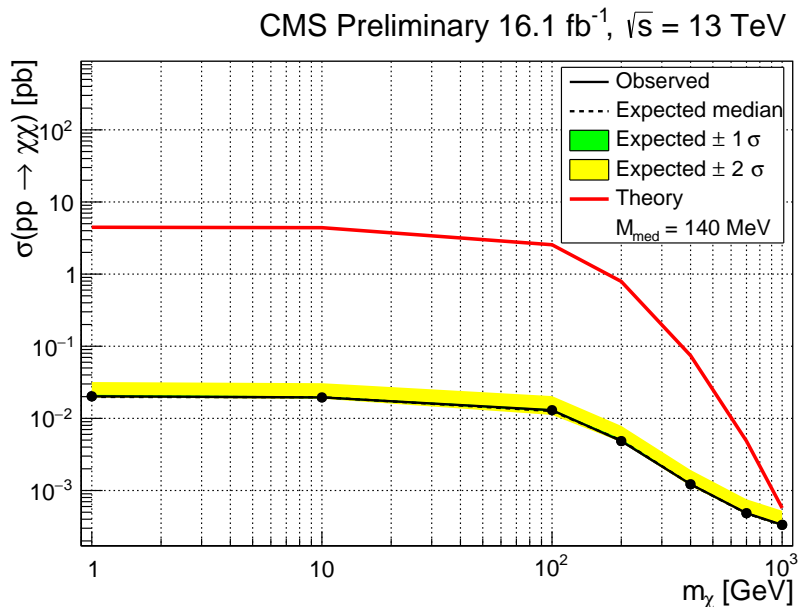


Figure 6.18: The expected and observed limits on the production cross section for SIMP masses between 1 and 1000 GeV, with  $1\sigma$  and  $2\sigma$  bands is shown, as well as the theoretical prediction (red), with respect to the generator level cuts ( $p_T^\chi > 200$  GeV and  $|\eta_\chi| < 2.5$ ).

# 7

1

2

## Conclusion & Outlook



## References

- [1] Michael E Peskin and Daniel V Schroeder. *An introduction to quantum field theory; 1995 ed.* Westview, Boulder, CO, 1995.
- [2] Yorikiyo Nagashima. *Beyond the standard model of elementary particle physics.* Wiley-VCH Verlag, Weinheim, Germany, 2014.
- [3] Georges Aad et al. *Observation of a new particle in the search for the Standard Model Higgs boson with the ATLAS detector at the LHC.* Phys. Lett., B716:1–29, 2012.
- [4] Serguei Chatrchyan et al. *Observation of a new boson at a mass of 125 GeV with the CMS experiment at the LHC.* Phys. Lett., B716:30–61, 2012.
- [5] Sheldon L. Glashow. *The renormalizability of vector meson interactions.* Nucl. Phys., 10:107–117, 1959.
- [6] Steven Weinberg. *A Model of Leptons.* Phys. Rev. Lett., 19:1264–1266, 1967.
- [7] Abdus Salam and John Clive Ward. *Weak and electromagnetic interactions.* Nuovo Cim., 11:568–577, 1959.
- [8] Peter W. Higgs. *Broken Symmetries and the Masses of Gauge Bosons.* Phys. Rev. Lett., 13:508–509, 1964.
- [9] F. Englert and R. Brout. *Broken Symmetry and the Mass of Gauge Vector Mesons.* Phys. Rev. Lett., 13:321–323, 1964.
- [10] G. S. Guralnik, C. R. Hagen, and T. W. B. Kibble. *Global Conservation Laws and Massless Particles.* Phys. Rev. Lett., 13:585–587, 1964.
- [11] David J. Gross and Frank Wilczek. *Ultraviolet Behavior of Nonabelian Gauge Theories.* Phys. Rev. Lett., 30:1343–1346, 1973.
- [12] H. David Politzer. *Reliable Perturbative Results for Strong Interactions?* Phys. Rev. Lett., 30:1346–1349, 1973.
- [13] <http://www.quantumdiaries.org/2014/03/14/the-standard-model-a-beautiful-but-flawed-theory/>
- [14] Q. R. Ahmad et al. *Direct evidence for neutrino flavor transformation from neutral current interactions in the Sudbury Neutrino Observatory.* Phys. Rev. Lett., 89:011301, 2002.
- [15] Y. Fukuda et al. *Evidence for oscillation of atmospheric neutrinos.* Phys. Rev. Lett., 81:1562–1567, 1998.
- [16] Gianfranco Bertone, Dan Hooper, and Joseph Silk. *Particle dark matter: Evidence, candidates and constraints.* Phys. Rept., 405:279–390, 2005.
- [17] F. Zwicky. *Die Rotverschiebung von extragalaktischen Nebeln.* Helv. Phys. Acta, 6:110–127, 1933. [Gen. Rel. Grav.41,207(2009)].
- [18] P. Salucci and A. Borriello. *The intriguing distribution of dark matter in galaxies.* Lect. Notes Phys., 616:66–77, 2003.

- [19] K. G. Begeman, A. H. Broeils, and R. H. Sanders. *Extended rotation curves of spiral galaxies: Dark haloes and modified dynamics*. Mon. Not. Roy. Astron. Soc., 249:523, 1991.
- [20] V. Belokurov, N. W. Evans, P. C. Hewett, A. Moiseev, R. G. McMahon, S. F. Sanchez, and L. J. King. *Two New Large Separation Gravitational Lenses from SDSS*. Mon. Not. Roy. Astron. Soc., 392:104, 2009.
- [21] Arno A. Penzias and Robert Woodrow Wilson. *A Measurement of excess antenna temperature at 4080-Mc/s*. Astrophys. J., 142:419–421, 1965.
- [22] George F. Smoot et al. *Structure in the COBE differential microwave radiometer first year maps*. Astrophys. J., 396:L1–L5, 1992.
- [23] E. Komatsu et al. *Seven-Year Wilkinson Microwave Anisotropy Probe (WMAP) Observations: Cosmological Interpretation*. Astrophys. J. Suppl., 192:18, 2011.
- [24] P. A. R. Ade et al. *Planck 2013 results. XVI. Cosmological parameters*. Astron. Astrophys., 571:A16, 2014.
- [25] <https://briankoberlein.com/2015/06/15/science-in-the-raw/>.
- [26] P. A. R. Ade et al. *Planck 2013 results. I. Overview of products and scientific results*. Astron. Astrophys., 571:A1, 2014.
- [27] M. Azzaro, F. Prada, and C. M. Gutierrez. *Motion properties of satellites around external spiral galaxies*. ASP Conf. Ser., 327:268, 2004.
- [28] Mario Mateo. *Dwarf galaxies of the Local Group*. Ann. Rev. Astron. Astrophys., 36:435–506, 1998.
- [29] John N. Bahcall, Chris Flynn, and Andrew Gould. *Local dark matter from a carefully selected sample*. Astrophys. J., 389:234–250, 1992.
- [30] Lars Bergström. *Nonbaryonic dark matter: Observational evidence and detection methods*. Rept. Prog. Phys., 63:793, 2000.
- [31] V. M. Lobashev. *The search for the neutrino mass by direct method in the tritium beta-decay and perspectives of study it in the project KATRIN*. Nucl. Phys., A719:153–160, 2003.
- [32] V. N. Aseev et al. *An upper limit on electron antineutrino mass from Troitsk experiment*. Phys. Rev., D84:112003, 2011.
- [33] Ch. Kraus et al. *Final results from phase II of the Mainz neutrino mass search in tritium beta decay*. Eur. Phys. J., C40:447–468, 2005.
- [34] M. C. Gonzalez-Garcia and Yosef Nir. *Neutrino masses and mixing: Evidence and implications*. Rev. Mod. Phys., 75:345–402, 2003.
- [35] Scott Dodelson and Lawrence M. Widrow. *Sterile-neutrinos as dark matter*. Phys. Rev. Lett., 72:17–20, 1994.
- [36] Naoki Yoshida, Aaron Sokasian, Lars Hernquist, and Volker Springel. *Early structure formation and reionization in a warm dark matter cosmology*. Astrophys. J., 591:L1–L4, 2003.
- [37] L. J. Rosenberg and K. A. van Bibber. *Searches for invisible axions*. Phys. Rept., 325:1–39, 2000.
- [38] Kimmo Kainulainen and Keith A. Olive. *Astrophysical and cosmological constraints on neutrino masses*. Springer Tracts Mod. Phys., 190:53–74, 2003.
- [39] Nima Arkani-Hamed, Savas Dimopoulos, and G. R. Dvali. *The Hierarchy problem and new dimensions at a millimeter*. Phys. Lett., B429:263–272, 1998.

- 1 [40] Lisa Randall and Raman Sundrum. *A Large mass hierarchy from a small extra dimension*. Phys.  
2 Rev. Lett., 83:3370–3373, 1999.
- 3 [41] Edward W. Kolb, Daniel J. H. Chung, and Antonio Riotto. *WIMPzillas!* In Trends in theoretical  
4 physics II. Proceedings, 2nd La Plata Meeting, Buenos Aires, Argentina, November 29–December  
5 4, 1998, pages 91–105, 1998. [,91(1998)].
- 6 [42] David N. Spergel and Paul J. Steinhardt. *Observational evidence for selfinteracting cold dark  
7 matter*. Phys. Rev. Lett., 84:3760–3763, 2000.
- 8 [43] A. De Rujula, S. L. Glashow, and U. Sarid. *CHARGED DARK MATTER*. Nucl. Phys., B333:173–  
9 194, 1990.
- 10 [44] Alexander Kusenko and Mikhail E. Shaposhnikov. *Supersymmetric Q balls as dark matter*. Phys.  
11 Lett., B418:46–54, 1998.
- 12 [45] John R. Ellis. *Particle candidates for dark matter*. Phys. Scripta, T85:221–230, 2000.
- 13 [46] Lars Bergstrom. *Dark Matter Candidates*. New J. Phys., 11:105006, 2009.
- 14 [47] R. Bernabei et al. *Final model independent result of DAMA/LIBRA-phase1*. Eur. Phys. J.,  
15 C73:2648, 2013.
- 16 [48] R. Agnese et al. *Search for Low-Mass Weakly Interacting Massive Particles with SuperCDMS*.  
17 Phys. Rev. Lett., 112(24):241302, 2014.
- 18 [49] E. Armengaud et al. *Constraints on low-mass WIMPs from the EDELWEISS-III dark matter search*.  
19 JCAP, 1605(05):019, 2016.
- 20 [50] G. Angloher et al. *Results on low mass WIMPs using an upgraded CRESST-II detector*. Eur. Phys.  
21 J., C74(12):3184, 2014.
- 22 [51] E. Aprile et al. *XENON100 Dark Matter Results from a Combination of 477 Live Days*. Phys.  
23 Rev., D94(12):122001, 2016.
- 24 [52] D. S. Akerib et al. *Results from a search for dark matter in the complete LUX exposure*. Phys. Rev.  
25 Lett., 118(2):021303, 2017.
- 26 [53] C. Amole et al. *Dark Matter Search Results from the PICO-60 C<sub>3</sub>F<sub>8</sub> Bubble Chamber*. Phys. Rev.  
27 Lett., 118(25):251301, 2017.
- 28 [54] Changbo Fu et al. *Spin-Dependent Weakly-Interacting-Massive-ParticleNucleon Cross Section  
29 Limits from First Data of PandaX-II Experiment*. Phys. Rev. Lett., 118(7):071301, 2017.
- 30 [55] Teresa Marrodán Undagoitia and Ludwig Rauch. *Dark matter direct-detection experiments*. J.  
31 Phys., G43(1):013001, 2016.
- 32 [56] W. B. Atwood et al. *The Large Area Telescope on the Fermi Gamma-ray Space Telescope Mission*.  
33 Astrophys. J., 697:1071–1102, 2009.
- 34 [57] F. Aharonian et al. *Observations of the Crab Nebula with H.E.S.S.* Astron. Astrophys., 457:899–  
35 915, 2006.
- 36 [58] J. Aleksic et al. *Performance of the MAGIC stereo system obtained with Crab Nebula data*. As-  
37 trropart. Phys., 35:435–448, 2012.
- 38 [59] J. Holder et al. *Status of the VERITAS Observatory*. AIP Conf. Proc., 1085:657–660, 2009.
- 39 [60] M. Ageron et al. *ANTARES: the first undersea neutrino telescope*. Nucl. Instrum. Meth., A656:11–  
40 38, 2011.

- [61] A. Achterberg et al. *First Year Performance of The IceCube Neutrino Telescope*. *Astropart. Phys.*, 26:155–173, 2006.
- [62] Andrei Kounine. *The Alpha Magnetic Spectrometer on the International Space Station*. *Int. J. Mod. Phys.*, E21(08):1230005, 2012.
- [63] P. Picozza et al. *PAMELA: A Payload for Antimatter Matter Exploration and Light-nuclei Astrophysics*. *Astropart. Phys.*, 27:296–315, 2007.
- [64] Albert M Sirunyan et al. *Search for dark matter produced with an energetic jet or a hadronically decaying W or Z boson at  $\sqrt{s} = 13$  TeV*. *JHEP*, 07:014, 2017.
- [65] Morad Aaboud et al. *Search for dark matter produced in association with a hadronically decaying vector boson in pp collisions at  $\sqrt{s} = 13$  TeV with the ATLAS detector*. *Phys. Lett.*, B763:251–268, 2016.
- [66] Felix Kahlhoefer. *Review of LHC Dark Matter Searches*. *Int. J. Mod. Phys.*, A32(13):1730006, 2017.
- [67] Oliver Buchmueller, Caterina Doglioni, and Lian Tao Wang. *Search for dark matter at colliders*. *Nature Phys.*, 13(3):217–223, 2017.
- [68] The ATLAS collaboration. *Search for long-lived, massive particles in events with displaced vertices and missing transverse momentum in 13 TeV pp collisions with the ATLAS detector*. 2017.
- [69] The ATLAS collaboration. *Search for long-lived charginos based on a disappearing-track signature in pp collisions at  $\sqrt{s} = 13$  TeV with the ATLAS detector*. 2017.
- [70] The ATLAS collaboration. *Search for Higgs boson decays to Beyond-the-Standard-Model light bosons in four-lepton events with the ATLAS detector at  $\sqrt{s} = 13$  TeV*. 2017.
- [71] Albert M Sirunyan et al. *Search for new physics with dijet angular distributions in proton-proton collisions at  $\sqrt{s} = 13$  TeV*. *JHEP*, 07:013, 2017.
- [72] Albert M Sirunyan et al. *Search for dijet resonances in protonproton collisions at  $\sqrt{s} = 13$  TeV and constraints on dark matter and other models*. *Phys. Lett.*, B769:520–542, 2017. [Erratum: *Phys. Lett.* B772,882(2017)].
- [73] Morad Aaboud et al. *Search for new phenomena in dijet events using  $37\text{ fb}^{-1}$  of pp collision data collected at  $\sqrt{s} = 13$  TeV with the ATLAS detector*. *Phys. Rev.*, D96:052004, 2017.
- [74] Yang Bai and Arvind Rajaraman. *Dark Matter Jets at the LHC*. 2011.
- [75] CMS Collaboration. *Search for heavy stable charged particles with  $12.9\text{ fb}^{-1}$  of 2016 data*. 2016.
- [76] Morad Aaboud et al. *Search for metastable heavy charged particles with large ionization energy loss in pp collisions at  $\sqrt{s} = 13$  TeV using the ATLAS experiment*. *Phys. Rev.*, D93(11):112015, 2016.
- [77] <http://cms-results.web.cern.ch/cms-results/public-results/publications/EXO/index.html>.
- [78] James S. Bullock. *Notes on the Missing Satellites Problem*. 2010.
- [79] Michael Boylan-Kolchin, James S. Bullock, and Manoj Kaplinghat. *Too big to fail? The puzzling darkness of massive Milky Way subhaloes*. *Mon. Not. Roy. Astron. Soc.*, 415:L40, 2011.
- [80] David H. Weinberg, James S. Bullock, Fabio Governato, Rachel Kuzio de Naray, and Annika H. G. Peter. *Cold dark matter: controversies on small scales*. *Proc. Nat. Acad. Sci.*, 112:12249–12255, 2014. [Proc. Nat. Acad. Sci. 112,2249(2015)].

- [81] Benoit Famaey and Stacy McGaugh. *Challenges for Lambda-CDM and MOND*. J. Phys. Conf. Ser., 437:012001, 2013.
- [82] J. F. Donoghue, E. Golowich, and Barry R. Holstein. *Dynamics of the standard model*. Camb. Monogr. Part. Phys. Nucl. Phys. Cosmol., 2:1–540, 1992. [Camb. Monogr. Part. Phys. Nucl. Phys. Cosmol.35(2014)].
- [83] C. Downum, T. Barnes, J. R. Stone, and E. S. Swanson. *Nucleon-meson coupling constants and form-factors in the quark model*. Phys. Lett., B638:455–460, 2006.
- [84] Scott W. Randall, Maxim Markevitch, Douglas Clowe, Anthony H. Gonzalez, and Marusa Bradac. *Constraints on the Self-Interaction Cross-Section of Dark Matter from Numerical Simulations of the Merging Galaxy Cluster 1E 0657-56*. Astrophys. J., 679:1173–1180, 2008.
- [85] Jonathan L. Feng. *Dark Matter Candidates from Particle Physics and Methods of Detection*. Ann. Rev. Astron. Astrophys., 48:495–545, 2010.
- [86] Gregory D. Mack, John F. Beacom, and Gianfranco Bertone. *Towards Closing the Window on Strongly Interacting Dark Matter: Far-Reaching Constraints from Earth’s Heat Flow*. Phys. Rev., D76:043523, 2007.
- [87] J. Rich, R. Rocchia, and M. Spiro. *A Search for Strongly Interacting Dark Matter*. Phys. Lett., B194:173, 1987. [,221(1987)].
- [88] Adrienne L. Erickcek, Paul J. Steinhardt, Dan McCammon, and Patrick C. McGuire. *Constraints on the Interactions between Dark Matter and Baryons from the X-ray Quantum Calorimetry Experiment*. Phys. Rev., D76:042007, 2007.
- [89] Gregory D. Mack and Adithya Manohar. *Closing the window on high-mass strongly interacting dark matter*. J. Phys., G40:115202, 2013.
- [90] Richard H. Cyburt, Brian D. Fields, Vasiliki Pavlidou, and Benjamin D. Wandelt. *Constraining strong baryon dark matter interactions with primordial nucleosynthesis and cosmic rays*. Phys. Rev., D65:123503, 2002.
- [91] Xue-lei Chen, Steen Hannestad, and Robert J. Scherrer. *Cosmic microwave background and large scale structure limits on the interaction between dark matter and baryons*. Phys. Rev., D65:123515, 2002.
- [92] Cora Dvorkin, Kfir Blum, and Marc Kamionkowski. *Constraining Dark Matter-Baryon Scattering with Linear Cosmology*. Phys. Rev., D89(2):023519, 2014.
- [93] H. Richard Gustafson, Cyril A. Ayre, Lawrence W. Jones, Michael J. Longo, and P. V. Rama Murthy. *Search for New Massive Long-lived Neutral Particles*. Phys. Rev. Lett., 37:474, 1976.
- [94] K. A. Olive et al. *Review of Particle Physics*. Chin. Phys., C38:090001, 2014.
- [95] N. Daci, Isabelle De Bruyn, S. Lowette, M. H. G. Tytgat, and B. Zaldivar. *Simplified SIMPs and the LHC*. JHEP, 11:108, 2015.
- [96] Esma Anais Mobs. *The CERN accelerator complex. Complexe des accrateurs du CERN*. Oct 2016. General Photo.
- [97] S. Chatrchyan et al. *The CMS Experiment at the CERN LHC*. JINST, 3:S08004, 2008.
- [98] David Aaron Matzner Dominguez, D. Abbaneo, K. Arndt, N. Bacchetta, A. Ball, E. Bartz, W. Bertl, G. M. Bilei, G. Bolla, H. W. K. Cheung, et al. *CMS Technical Design Report for the Pixel Detector Upgrade*. 2012.

- 1 [99] G. L. Bayatian et al. *CMS Physics*. 2006.
- 2 [100] Serguei Chatrchyan et al. *Energy Calibration and Resolution of the CMS Electromagnetic*  
3 *Calorimeter in pp Collisions at  $\sqrt{s} = 7 \text{ TeV}$* . JINST, 8:P09009, 2013. [JINST8,9009(2013)].
- 4 [101] Giovanni Abbiendi. *The CMS muon system in Run2: preparation, status and first results*. PoS,  
5 EPS-HEP2015:237, 2015.
- 6 [102] A. Tapper and Darin Acosta. *CMS Technical Design Report for the Level-1 Trigger Upgrade*.  
7 2013.
- 8 [103] Jean-marc Olivier Andre, Ulf Behrens, James Branson, Philipp Maximilian Brummer, Olivier  
9 Chaze, Sergio Cittolin, Cristian Contescu, Benjamin Gordon Craigs, Georgiana Lavinia Dar-  
10 lea, Christian Deldicque, Zeynep Demiragli, Marc Dobson, Nicolas Doualot, Samim Erhan,  
11 Jonathan Richard Fulcher, Dominique Gigi, Maciej Szymon Gladki, Frank Glege, Guillermo  
12 Gomez Ceballos, Jeroen Guido Hegeman, Andre Georg Holzner, Mindaugas Janulis, Raul  
13 Jimenez Estupinan, Lorenzo Masetti, Franciscus Meijers, Emilio Meschi, Remigius Mommsen,  
14 Srecko Morovic, Vivian O'Dell, Luciano Orsini, Christoph Maria Ernst Paus, Petia Petrova, Marco  
15 Pieri, Attila Racz, Thomas Reis, Hannes Sakulin, Christoph Schwick, Dainius Simelevicius, Petr  
16 Zejdl, Hamburg, California, San Diego, California, Chicago, Illinois, Massachusetts Institute  
17 of Technology, Cambridge, Massachusetts, also at Vilnius University, Vilnius, Lithuania, and also  
18 at. *Performance of the CMS Event Builder*. Technical Report CMS-CR-2017-034, CERN, Geneva,  
19 Feb 2017.
- 20 [104] J. Pumplin, D. R. Stump, J. Huston, H. L. Lai, Pavel M. Nadolsky, and W. K. Tung. *New generation*  
21 *of parton distributions with uncertainties from global QCD analysis*. JHEP, 07:012, 2002.
- 22 [105] A. D. Martin, W. J. Stirling, R. S. Thorne, and G. Watt. *Parton distributions for the LHC*. Eur.  
23 Phys. J., C63:189–285, 2009.
- 24 [106] Richard D. Ball et al. *Parton distributions for the LHC Run II*. JHEP, 04:040, 2015.
- 25 [107] J. Alwall, R. Frederix, S. Frixione, V. Hirschi, F. Maltoni, O. Mattelaer, H. S. Shao, T. Stelzer,  
26 P. Torrielli, and M. Zaro. *The automated computation of tree-level and next-to-leading order*  
27 *differential cross sections, and their matching to parton shower simulations*. JHEP, 07:079, 2014.
- 28 [108] Stefano Frixione, Paolo Nason, and Carlo Oleari. *Matching NLO QCD computations with Parton*  
29 *Shower simulations: the POWHEG method*. JHEP, 11:070, 2007.
- 30 [109] V. N. Gribov and L. N. Lipatov. *Deep inelastic e p scattering in perturbation theory*. Sov. J. Nucl.  
31 Phys., 15:438–450, 1972. [Yad. Fiz.15,781(1972)].
- 32 [110] Yuri L. Dokshitzer. *Calculation of the Structure Functions for Deep Inelastic Scattering and e+ e-*  
33 *Annihilation by Perturbation Theory in Quantum Chromodynamics*. Sov. Phys. JETP, 46:641–653,  
34 1977. [Zh. Eksp. Teor. Fiz.73,1216(1977)].
- 35 [111] Guido Altarelli and G. Parisi. *Asymptotic Freedom in Parton Language*. Nucl. Phys., B126:298–  
36 318, 1977.
- 37 [112] Torbjörn Sjöstrand, Stephen Mrenna, and Peter Skands. *PYTHIA 6.4 physics and manual*. JHEP,  
38 05:026, 2006.
- 39 [113] John Allison et al. *Geant4 developments and applications*. IEEE Trans. Nucl. Sci., 53:270, 2006.
- 40 [114] Serguei Chatrchyan et al. *Description and performance of track and primary-vertex reconstruction*  
41 *with the CMS tracker*. JINST, 9(10):P10009, 2014.
- 42 [115] A. Strandlie and R. Frühwirth. *Discrimination between different types of material in track recon-*  
43 *struction with a Gaussian-sum filter*. IEEE Trans. Nucl. Sci., 53:3842–3849, 2006.

- 1 [116] A. M. Sirunyan et al. *Particle-flow reconstruction and global event description with the CMS*  
2 *detector*. JINST, 12:P10003, 2017.
- 3 [117] Matteo Cacciari, Gavin P. Salam, and Gregory Soyez. *The anti-  $k_t$  jet clustering algorithm*. Journal  
4 of High Energy Physics, 2008(04):063, 2008.
- 5 [118] Serguei Chatrchyan et al. *Identification of  $b$ -quark jets with the CMS experiment*. JINST, 8:P04013,  
6 2013.
- 7 [119] Vardan Khachatryan et al. *Reconstruction and identification of lepton decays to hadrons and at*  
8 *CMS*. JINST, 11(01):P01019, 2016.
- 9 [120] Adam Alloul, Neil D. Christensen, Céline Degrande, Claude Duhr, and Benjamin Fuks. *FeynRules*  
10 *2.0 - A complete toolbox for tree-level phenomenology*. Comput.Phys.Commun., 185:2250–2300,  
11 2014.
- 12 [121] Johann H. Kuhn, A. Kulesza, S. Pozzorini, and M. Schulze. *Electroweak corrections to hadronic*  
13 *photon production at large transverse momenta*. JHEP, 03:059, 2006.
- 14 [122] Stefan Kallweit, Jonas M. Lindert, Stefano Pozzorini, Marek Schnherr, and Philipp Maierhfer.  
15 *NLO QCD+EW automation and precise predictions for  $V$ +multijet production*. In Proceedings,  
16 50th Rencontres de Moriond, QCD and high energy interactions: La Thuile, Italy, March 21–28,  
17 2015, pages 121–124, 2015.
- 18 [123] Stefan Kallweit, Jonas M. Lindert, Philipp Maierhfer, Stefano Pozzorini, and Marek Schnherr.  
19 *NLO electroweak automation and precise predictions for  $W$ +multijet production at the LHC*. JHEP,  
20 04:012, 2015.
- 21 [124] Stefan Kallweit, Jonas M. Lindert, Philipp Maierhofer, Stefano Pozzorini, and Marek Schnherr.  
22 *NLO QCD+EW predictions for  $V$  + jets including off-shell vector-boson decays and multijet merg-*  
23 *ing*. JHEP, 04:021, 2016.
- 24 [125] A. L. Read. *Presentation of search results: the CLs technique*. J. Phys., G28:2693, 2002.
- 25 [126] T. Junk. *Confidence level computation for combining searches with small statistics*. Nucl. Instrum.  
26 Meth., A434:435, 1999.



# List of Acronyms

1

2

3

## A

4

5  
6 ATLAS Almost Toroidal LHC ApparatuS

7

8

## B

9

10  
11 BU Builder Unit

12

13

## C

14

15  
16 CERN European Organization for Nuclear Research  
17 CHS charged hadron subtraction  
18 CMB Cosmic Microwave Background  
19 CMS Compact Muon Solenoid  
20 CSC Cathode Strip Chambers

21

22

## D

23

24  
25 DAQ data acquisition  
26 DQM Data Quality Monitoring  
27 DT Drift Tubes

28

29

## E

30

31  
32 ECAL electromagnetic calorimeter

33

34

## F

35

36  
37 FED Front End Driver  
38 FSR final state radiation  
39 FU Filter Unit

1

2

**G**

3

4

5 GSF Gaussian-sum filter

6

7

**H**

8

10 HCAL hadronic calorimeter  
11 HLT High-Level Trigger  
12 HSCP heavy stable neutral particle

13

14

15 **I**

16

17 IP interaction point  
18 ISR initial state radiation

19

20

**J**

21

23 JER jet energy resolution

24

25

**L**

26

28 L1 Level-1  
29 LEIR Low Energy Ion Ring  
30 LEP Large Electron Positron  
31 LHC Large Hadron Collider  
32 LO leading order

33

34

**N**

35

37 NLO next-to-leading order

38

39

**P**

40

42 PDF parton distribution function  
43 PF particle flow  
44 PS Proton Synchrotron  
45 PSB Proton Synchrotron Booster

1

2

**Q**

3

4

5 QCD

Quantum Chromodynamics

6

7

**R**

8

9 10 RF

radio-frequency

11 ROC

read-out chip

12 RPC

Resistive Plate Chambers

13 RU

Readout Unit

14

15

**S**

16

17 18 SIDM

self-interacting dark matter

19 SIMP

strongly interacting massive particle

20 SPS

Super Proton Synchrotron

21 SUSY

supersymmetry

22

23

**T**

24

25 26 TEC

Tracker EndCaps

27 TIB

Tracker Inner Barrel

28 TID

Tracker Inner Disks

29 TOB

Tracker Outer Barrel

30

31

**W**

32

33 34 WIMP

weakly interacting massive particle

